SCANNING NEAR-FIELD OPTICAL MICROSCOPY STUDY OF $PtSe_2$ FLAKES

WONG KIN PING

MPhil

The Hong Kong Polytechnic University

2020

The Hong Kong Polytechnic University

Department of Applied Physics

SCANNING NEAR-FIELD OPTICAL MICROSCOPY STUDY OF PtSe2 FLAKES

Wong Kin Ping

A thesis submitted in partial fulfilment of the requirements for the degree of Master of Philosophy

08/2019

CERTIFICATE OF ORIGINALITY

I hereby declare that this thesis is my own work and that, to the best of my knowledge and belief, it reproduces no material previously published or written, nor material that has been accepted for the award of any other degree or diploma, except where due acknowledgement has been made in the text.

(Signed)_____

(Name of student)_____Wong Kin Ping_____

Abstract

Scientists are exploring the mid-infrared (MIR) optoelectronic properties of two-dimensional (2D) materials. Noble metal (Group 10) dichalcogenides MX_2 (M = Pt, Pd, X = S, Se, etc.) are the potential candidates for MIR applications due to their matching bandgaps and high stability. $PtSe_2$ is an emerging 2D material for MIR optoelectronics and photonics due to its air stability, high electron mobility and layer-dependent band gap.

Inspired by the conventional-FTIR spectra of $PtSe_2$ flakes, which reveals the waveguide supporting properties of $PtSe_2$, scanning near-field optical microscopy (s-SNOM) and nano-Fourier Transform Infrared Spectroscopy (nano-FTIR) were employed to study the mechanically exfoliated $PtSe_2$ flakes. Like pervious study on waveguide supporting TMDCs such as WSe_2, $MoSe_2$ and MoS_2, interference fringe patterns were observed in real space by the use of s-SNOM. The fringes were induced by the MIR waveguide photon modes of $PtSe_2$, in contrast to previous studies, in where visible light was used. The full-range edge orientation dependence of the fringe patterns was studied for the first time. By tuning the MIR frequency from 1380 to 2519 cm^{-1}, the dispersion relation of the waveguide modes with different thicknesses can be extracted. Theoretical calculations, based on the dielectric constant of $PtSe_2$ obtained by conventional-FTIR, are in good agreement with the experimental results. Interestingly, in addition to the commonly observed (transverse magnetic) TM modes, the (transverse electric) TE modes were also visualised. This work reveals the applicability of s-SNOM in high-loss MIR waveguide mode imaging, in contrast to the previous studies, in which low-loss visible waveguide modes were observed. In addition, the dielectric constant of the $PtSe_2$ flakes in MIR range is validated.

Acknowledgements

First of all, I would like to express my sincere thanks to my supervisor, Prof. Lau Shu Ping Daniel, who gave me the valuable chance to study MPhil at PolyU, in spite of my late application and graduation problem. Also, Prof. Lau supervised me patiently and considerately, notwithstanding my slow progression on the research work. During his two-year supervision, I did not bear much pressure but enjoyed my research work.

Special thank is also given to Dr. Hu Xin, who selflessly taught me lots of experimental skills and necessary theories. Without his encouragement, inspiration and teaching, I cannot accomplish my work.

I would also like to express appreciation to Mr. Lo Tsz Wing Billy as he taught me skills in implementing the s-SNOM and nano-FTIR and skills in mechanical exfoliation.

Last but not least, I express my great gratitude to my parents, who let me pursue my goal and idea.

Contents

1 Introduction

The optoelectronic properties of two-dimensional (2D) materials including graphene, black phosphorous (BP) and transition metal dichalcogenides (TMDCs) in mid-infrared (MIR) are being explored. However, graphene suffers from narrow bandgap and BP possesses poor stability under ambient conditions. Thus, the exploration of alternative materials for MIR optoelectronics is of scientific importance. Noble metal (Group 10) dichalcogenides MX_2 (M = Pt, Pd, X = S, Se or Te) [1-3] are the potential candidates, but comparatively little explored, for MIR applications due to their bandgap and high stability. Among the group, $PtSe_2$ is an emerging 2D material for optoelectronics and photonics due to its air stability and high electron mobility [4, 5]. The most intriguing property of $PtSe_2$ is its layer-induced semiconductor-to-metal (SM) transition, predicted by theory [6, 7] and confirmed by experiments [8-10]. Although $PtSe_2$ is type-II Dirac semi-metal [11, 12] in its bulk form, monolayer $PtSe_2$ is a semiconductor with bandgap near 1.2 eV [2, 8] while the bandgap of bilayer $PtSe_2$ is about 0.2eV [7, 8]. The $PtSe_2$ becomes semi-metallic when it is of trilayer form [8, 10]. SM transition can also be induced by strain [6, 13-15]. These properties suggest the possibility of wide range of application including field effect transistors (FETs) [5, 16], gas sensing [17], photocatalysis [8], photodetection [18], spintronics [19], valleytronics [8] and also MIR applications [10].

Scattering type scanning near-field optical microscopy (s-SNOM) [20-22] is a state-of-art technique for performing nano-optical imaging, which allows study in nano-science such as mapping of free carrier [23-25], the material characterization [26-28], crystal quality characterization [29], the strain-field mapping in semiconductor crystals [30, 31], imaging of nano-phase-transition in VO_2 [32, 33].

Nano-Fourier Transform Infrared Spectroscopy (Nano-FTIR), a technique combining the nano-scale resolving power of s-SNOM and the analytical power of conventional-FTIR, is capable of performing infrared spectroscopy in nanoscale. This so called near-field infrared spectroscopy has been applied for nanoscale chemical sensing at the so-called "fingerprint" frequency region [34], extraction of local (nanoscale-resolved) optical constant [35-37], studying micro-strain in semiconductor crystals [31].

In recently years, polaritons, which are hybrid light-matter quasiparticles, have been widely studied in 2D materials and van der Waals materials [38-40]. The properties of these electromagnetic modes have been studied by employing s-SNOM and nano-FTIR. By nano-optical imaging study performed by s-SNOM, different kinds of polaritons was imaged directly in real-space and the properties of these polaritons were found by analysing the observed fringe patterns. Surface plasmon polaritons (SPP) in graphene was found to have gate-tunability, strong field confinement and low loss property [41, 42]. Surface phonon polaritons (SPhP) in h-BN [43, 44] and α-MoO_3 [45, 46] were found to has hyperbolicity property. Black phosphorus was found to support coupled plasmon-phonon polaritons upon ultrafast pump-probe technique [47]. In addition, waveguide exciton polaritons (EP) in WSe_2 [48, 49] and $MoSe_2$ [50] and waveguide modes in MoS_2 [51, 52] were found to have long-distance propagation length in specific frequency range. Detail study in these modes could be useful for future nanophotonic circuits applied for manipulating light in nanoscale. On the other hand, near-field enhancement by plasmon-phonon coupling in graphene/SiO_2 [53] interface and MoS_2/SiO_2 [54] interface was observed from the near-field spectra generated by near-field IR spectroscopy. Also, near-field IR

spectroscopy has also been employed for fundamental study of the spectral response in monolayer $MnPS_3$ [55].

Although the electronic and photonic properties of $PtSe_2$ have been studied, the near-field optical properties of it remain unexplored. In this work, s-SNOM and nano-FTIR were employed to perform nano-optical study on $PtSe_2$ flakes. Interference fringe patterns induced by the MIR waveguide photon modes of $PtSe_2$ were observed in real space by the use of s-SNOM. The edge orientation dependence of the fringe patterns was studied. By tuning the MIR frequency from 1380 to 2519 cm^{-1}, the dispersion relation of the waveguide modes with different thicknesses can be extracted. In order to theoretically calculate the dispersion relations of these modes, the dielectric constant of $PtSe_2$ was obtained by fitting the conventional-FTIR reflectivity spectrum. The reflectivity spectrum showed that $PtSe_2$ exhibited low absorption and Fabry–Pérot cavity effect in the MIR frequency from 1000 to 3000 cm^{-1}, thereby revealing its waveguide supporting properties. The theoretical calculations of the dispersion relations are in good agreement with the experimental results. The calculations were performed by solving the eigenequations numerically or calculating the imaginary part of the Fresnel reflection coefficients analytically. Interestingly, in addition to the commonly observed TM modes, the TE modes were also visualised. This work reveals the applicability of s-SNOM in high-loss MIR waveguide mode imaging, in contrast to previous studies, in which low-loss visible waveguide modes were observed [48, 52]. In addition, the dielectric constant of the $PtSe_2$ flakes in MIR range was validated by the far-field FTIR spectroscopy. From the far-field analysis, it is also found that the free charge carrier concentration of $PtSe_2$ is $N = 1.75 \times 10^{20}$ cm^{-3}, which is within the a typical range for a semimetal: $1 \times 10^{17} - 1 \times 10^{22}$ cm^{-3}.

In this thesis, the working principle of s-SNOM will be introduced. Basic theories necessary for nano-optics and s-SNOM will also be presented. Following is the introduction of nano-FTIR. Finally, the experimental results and corresponding analysis of the near-field optical microscopy study of $PtSe_2$ flakes will be demonstrated.

2 Scattering - Scanning Near-Field Optical Microscopy

2.1 Nano-Optics

Nanotechnology and nanoscience are mainstream research field nowadays. Beginning from 20th century, with the development of quantum physics, it is known that in ultra-small scales, the physical phenomena are different from that in macroscopic world. Scientists hope to explore these exotic effects which might be applicable in the future technology [56].

Nano-optics, one of the branches of nanotechnology, studies the behaviour of light and light-matter interaction on the nanoscale. Optical microscopy is important for characterizing the nanostructure. However, the diffraction effect limits the resolution of conventional optical microscope to about half of the wavelength of the light [57, 58]. To avoid this diffraction limit, near-field optical microscope [20, 59], for example, the s-SNOM, instead of classical far-field microscope, is used to study materials' optical properties.

2.2 Theoretical Background

2.2.1 Maxwell's Equations

In order to interpret the optical image taken by the near-field optical microscope, the light-matter interactions during the imaging process should be studied

comprehensively. In classical electrodynamics, light can be described by electromagnetic wave and therefore the coupling between light and matter can be analysed with the use of Maxwell's Equations [60, 61], by which J. C. Maxwell unified the electric field and magnetic field into a single physical field, electromagnetic (EM) field, and deduced that light is an electromagnetic wave [62, 63]. The expressions of these equations in SI units are

$$\nabla \times \mathbf{E}(\mathbf{r}, t) = -\frac{\partial \mathbf{B}(\mathbf{r}, t)}{\partial t}, \tag{1}$$

$$\nabla \times \mathbf{H}(\mathbf{r}, t) = \frac{\partial \mathbf{D}(\mathbf{r}, t)}{\partial t} + \mathbf{J}(\mathbf{r}, t), \tag{2}$$

$$\nabla \cdot \mathbf{D}(\mathbf{r}, t) = \rho(\mathbf{r}, t), \tag{3}$$

$$\nabla \cdot \mathbf{B}(\mathbf{r}, t) = 0, \tag{4}$$

where **E**, **D**, **B** and **H** are electric field, electric displacement, magnetic flux density and magnetic field respectively. ρ and **J** are charge density and current density. **D** and **H** are important for studying the electromagnetic field in matter because they account for the bound charge and bound current inside the matter. Maxwell's equations (Equations (1) - (4)) only describe how the EM field is generated by existing charges and currents but not reveal how these charges and currents inside the material are generated. It is the constitutive relations to account for the response of materials under the influence of EM field. In general, for linear and isotropic materials, the constitutive relations in **k** and ω domain, relating **E**, **D**, **B** and **H** are

$$\mathbf{D}(\mathbf{k}, \omega) = \varepsilon_0 \varepsilon_r(\mathbf{k}, \omega)\mathbf{E}(\mathbf{k}, \omega), \tag{5}$$

$$\mathbf{B}(\mathbf{k}, \omega) = \mu_0 \mu_r(\mathbf{k}, \omega)\mathbf{H}(\mathbf{k}, \omega), \tag{6}$$

where ε_0 and μ_0 are the permittivity and permeability in free space respectively, and ε_r and μ_r are the relative permittivity (also called dielectric constant) and the relative permeability of the material. The response functions ε_r and μ_r are complex values if there is phase lag between the response (**D** and **B**) and the influencing field (**E** and **H**). The complex-valued dielectric constant ε_r will be derived with the use of a classical model in Section 2.2.2. Within this model, the phase lag is explained by the damping in the oscillating system. The ohm's law

$$\mathbf{J}(\mathbf{k},\omega) = \sigma(\mathbf{k},\omega)\mathbf{E}(\mathbf{k},\omega) \tag{7}$$

is another constitutive relation that is responsible to conducting materials. $\sigma(\mathbf{k},\omega)$ denotes the complex conductivity of the conducting materials. Same as ε_r and μ_r it is a complex value because there may be a phase difference between **J** and **E**.

If monochromatic field is used, the electric field $\mathbf{E}(\mathbf{r},t)$, for example, can be expressed as the real part of the corresponding complex time-harmonic field:

$$\mathbf{E}(\mathbf{r},t) = \mathrm{Re}\left(\mathbf{E}(\mathbf{r})\mathrm{e}^{-i\omega t}\right), \tag{8}$$

where the spatial distribution of amplitude $\mathbf{E}(\mathbf{r})$ is complex while $\mathbf{E}(\mathbf{r},t)$ is real as in Equation (1). **D**, **B**, **H**, ρ and **J** can be expressed as similar form as Equation (8). By using these new forms, the Maxwell's Equations (1)-(4) can be now expressed by the complex spatial amplitudes $\mathbf{E}(\mathbf{r})$, $\mathbf{D}(\mathbf{r})$, $\mathbf{B}(\mathbf{r})$, $\mathbf{H}(\mathbf{r})$, $\rho(\mathbf{r})$ and $\mathbf{J}(\mathbf{r})$:

$$\nabla \times \mathbf{E}(\mathbf{r}) = i\omega\mathbf{B}(\mathbf{r}), \tag{9}$$

$$\nabla \times \mathbf{H}(\mathbf{r}) = -i\omega\mathbf{D}(\mathbf{r}) + \mathbf{J}(\mathbf{r}), \tag{10}$$

$$\nabla \cdot \mathbf{D}(\mathbf{r}) = \rho(\mathbf{r}), \tag{11}$$

$$\nabla \cdot \mathbf{B}(\mathbf{r}) = 0. \tag{12}$$

If the field is not only monochromatic, but also a plane wave, the E-field can be expressed as

$$\mathbf{E}(\mathbf{r}, t) = \mathrm{Re}\left(\mathbf{E}(\mathbf{k}, \omega)\mathrm{e}^{i(\mathbf{k}\cdot\mathbf{r}-\omega t)}\right). \tag{13}$$

Comparing Equation (13) with (8), the complex amplitude $\mathbf{E}(\mathbf{r})$ of time harmonic expression can be expressed as

$$\mathbf{E}(\mathbf{r}) = \mathbf{E}(\mathbf{k}, \omega)\mathrm{e}^{i\mathbf{k}\cdot\mathbf{r}}. \tag{14}$$

Expression (14) implies that, for monochromatic plane wave, the constitutive relations (Equations (5) – (7)) can be expressed by terms of the complex amplitudes in position space:

$$\mathbf{D}(\mathbf{r}) = \varepsilon_0\varepsilon_r(\mathbf{k}, \omega)\mathbf{E}(\mathbf{r}), \tag{15}$$

$$\mathbf{B}(\mathbf{r}) = \mu_0\mu_r(\mathbf{k}, \omega)\mathbf{H}(\mathbf{r}), \tag{16}$$

$$\mathbf{J}(\mathbf{r}) = \sigma(\mathbf{k}, \omega)\mathbf{E}(\mathbf{r}). \tag{17}$$

The Maxwell's Equations (9) – (12), together with the constitutive relations (Equations (15) – (17)), can be applied for studying the light-matter interaction for the specific case of monochromatic incident light.

2.2.2 Complex Dielectric constant

The constitutive relations (5) and (6) (or Equations (15) and (16) for the case of monochromatic light) show that the dielectric constant (or relative permittivity) $\varepsilon_r(\mathbf{k}, \omega)$ and the relative permeability $\mu_r(\mathbf{k}, \omega)$ play an important role in determining the displacement field **D** and magnetic field **H**, which in turn are important parameters for studying the electrodynamics in matter. If non-magnetic material is considered, that is $\mu_r(\mathbf{k}, \omega) = 1$, the dielectric constant $\varepsilon_r(\mathbf{k}, \omega)$ is the key to study the light-matter interaction in material. For example, it is a necessary parameter for calculating the Fresnel coefficient and the dispersion relation of electromagnetic surface modes and waveguide modes in material, as will be discussed in Sections 2.2.3 and 2.2.5 respectively. For vacuum and transparent (weakly absorbing) materials, $\varepsilon_r(\mathbf{k}, \omega)$ is real and positive, but for absorbing medium, $\varepsilon_r(\mathbf{k}, \omega)$ can be complex-valued. Here the classical modelling of the complex-valued dielectric constant $\varepsilon_r(\mathbf{k}, \omega)$ will be introduced.

2.2.2.1 Lorentz Dipole Oscillator Model for Bound Electrons

In 1865, Maxwell deduced from his electromagnetic theory that light is a EM wave [63]. From this deduction, theorists predicted that a dipole oscillator can be a source of light. Based on this prediction and the fact that atoms can emit and absorb light at discrete wavelengths, which is now known as the result of the interband transition, H. A. Lorentz became the first to model the atoms as oscillating electric

dipoles to account for the absorption of light by the contribution of bound charges inside the atoms. It should be noted that Lorentz proposed that theory before the discovery of electrons and nuclei, and before the experimental confirmation that an electric dipole can generate and absorb EM waves.

In the Lorentz's model [64, 65], the bound electrons inside an atom are connected with the heavy nuclei by springs with different force constants, forming different oscillating electric dipoles with different resonant frequencies ω_0. Quantum mechanically, the ω_0 is related to the energy of a photon ($E = \hbar\omega_0$) absorbed by the electron when interband transition occurs. When light, an EM wave, is incident on the atoms inside the material, the electric field (E-field) of the light will drive the bound electrons to oscillate. Because the nuclei are much heavier than the bound electrons, the induced motion of the nuclei by the E-field is ignored. The equation of motion of the bound electron with mass m_0 and charge $-e$ is

$$m_0 \frac{\mathrm{d}^2 \boldsymbol{x}}{\mathrm{d}t^2} + m_0 \gamma \frac{\mathrm{d}\boldsymbol{x}}{\mathrm{d}t} + m_0 \omega_0^2 \boldsymbol{x} = -e\boldsymbol{E}, \tag{18}$$

where x is the induced displacement of the bound electron, E is the driving E-field of the incident light (magnetic force can be neglected compared with the electric force) and γ is the phenomenological damping rate of the damped harmonic oscillator, introduced to account for the absorption strength of the electric dipole to light. Considering monochromatic light with complex time-harmonic E-field $\boldsymbol{E}(\boldsymbol{r}, t) = \boldsymbol{E_0}(\boldsymbol{r})\mathrm{e}^{-i\omega t}$ (Equation (8)), and looking for solution of (complex) displacement x with the form $\boldsymbol{x}(\boldsymbol{r}, t) = \boldsymbol{X_0}(\boldsymbol{r})\mathrm{e}^{-i\omega t}$, by solving Equation (18) we found that $\boldsymbol{X_0}(\boldsymbol{r}) = \frac{-e}{m_0}\frac{1}{\omega_0^2 - \omega^2 - i\gamma\omega}\boldsymbol{E_0}(\boldsymbol{r})$, and therefore the induced dipole moment $\boldsymbol{p} = -e\boldsymbol{x}$ can be found.

The induced macroscopic polarization, that is, dipole moment per unit volume, of the material is $\boldsymbol{P} = N\boldsymbol{p} = -Ne\boldsymbol{x}$, where N is the number of atoms per unit volume and therefore the complex amplitude is given by

$$\boldsymbol{P_0}(\boldsymbol{r}) = \frac{Ne^2}{m_0}\frac{1}{\omega_0^2 - \omega^2 - i\gamma\omega}\boldsymbol{E_0}(\boldsymbol{r}). \tag{19}$$

One can find that $\boldsymbol{P}$ is small unless the frequency of the light is close to the natural frequency ω_0 of the electric dipole. The electric displacement can be calculated from $\boldsymbol{P}$ through its definition (for monochromatic light) $\boldsymbol{D_0}(\boldsymbol{r}) = \varepsilon_0\boldsymbol{E_0}(\boldsymbol{r}) + \boldsymbol{P_0}(\boldsymbol{r})$. On the other hand, the definition of the complex dielectric constant ε_r is given by the constitutive relation (for monochromatic light) $\boldsymbol{D_0}(\boldsymbol{r}) = \varepsilon_0\varepsilon_r(\mathbf{k}, \omega)\boldsymbol{E_0}(\mathbf{r})$ (Equation (15)). Combining these results and splitting the macroscopic polarization into a background term ($\boldsymbol{P_{bg}}(\boldsymbol{r}) = \varepsilon_0\chi_{bg}\boldsymbol{E_0}(\mathbf{r})$) and the resonant term, that is, $\boldsymbol{D_0}(\boldsymbol{r}) = \varepsilon_0\boldsymbol{E_0}(\boldsymbol{r}) + \varepsilon_0\chi_{bg}\boldsymbol{E_0}(\mathbf{r}) + \boldsymbol{P_0}(\boldsymbol{r})$, where χ_{bg} is the electric susceptibility of all other contributions to the polarizability, the ε_r is given by: $\varepsilon_r(\omega) = \varepsilon_\infty + \frac{Ne^2}{\varepsilon_0 m_0}\frac{1}{\omega_0^2 - \omega^2 - i\gamma\omega}$, in which the $1 + \chi_{bg}$ term is replaced by the high-frequency dielectric constant ε_∞. Because there can be electric dipoles with different natural frequencies ω_0 to account for different electronic transitions between discrete energy-levels, the $\varepsilon_r(\omega)$ should be account for the total effect for all the transitions within the frequency range in interest. Also, from quantum mechanics we know different transitions have different transition probability and therefore a phenomenological oscillator strength f_j should be introduced to each transition (j). As a result, the complex dielectric constant ε_r for bound electrons in this classical Lorentz's model is given by:

$$\varepsilon_{r,\text{bound}}(\omega) = \varepsilon_\infty + \frac{Ne^2}{\varepsilon_0 m_0} \sum_j \frac{f_j}{\omega_{0,j}^2 - \omega^2 - i\gamma\omega}, \tag{20}$$

where $\sum_j f_j = 1$ for each bound electron. If all oscillators are included in the summation, the high-frequency dielectric constant ε_∞ is equal to 1. It should be noted that the Lorentz's model does not account for the $\mathbf{k}$-dependency of ε_r. This $\mathbf{k}$-dependency comes from the non-local effect which becomes important when the wavelength of light is comparable to electrons' mean free paths or the unit cell. Nonetheless, this effect is neglectable in most cases so the Lorentz's model is often applied to predict optical phenomena of materials, provided that the wavelength is long enough.

2.2.2.2 Drude Model for Free Charge Electrons

In last Section, only the contribution from bound electrons is considered for deriving the complex-valued dielectric constant ε_r. However, for conducting materials such as metals and doped semiconductors, there is also high density of free charge carriers, which give additional contribution to the optical response of materials. The ε_r of a free-electron-system can be derived from the classical Drude Model [66, 67].

In his model of free electron, P. Drude in 1900 assumed that the valence electrons are delocalized and the much heavier metal ions remain immobile in a metallic system. Therefore, the delocalized electrons, that is, the conduction electrons, forms a free electron gas and Drude applied the kinetic theory to study its electronic properties. When the conduction electrons move freely inside the metal, they will

suffer collisions with the metal ions. The average duration of an electron between two successive collision is the mean free time (or relaxation time) τ and therefore the characteristic collision frequency is $\gamma = 1/\tau$. Between collisions, Drude boldly assumed that the electron-electron interactions and the electron-ion interactions can be neglected (independent electron approximation and free electron approximation respectively). Therefore, the conduction electrons wander freely with constant velocity in a straight line between collisions. Under these assumptions, the equation of motions of the free electrons under the influence of the E-field of the incident light (like Equation (18) for bound electrons) can be derived as followed. Given than at time t, the momentum of a free electron is $\boldsymbol{p}(t)$. Between the time t and time $t + \Delta t$, the electron will collide with an ion with a probability $\Delta t/\tau$, and have a probability $1 - \Delta t/\tau$ to wander without suffering a collision. For the process without a collision, the electron will gain momentum $-e\boldsymbol{E}\Delta t$ by the E-field E of the light. Because, in Drude model, after collisions the electrons are assumed to move with random directions with speed corresponding to the temperature of the collision place (so as to achieve thermal equilibrium), the average momentum of the electron after a collision is therefore zero. After suffering a collision, the electron will gain momentum (from zero) by the E-field for time duration less than Δt. The final momentum is thus equal to $-e\boldsymbol{E}\alpha\Delta t$, where α is a factor between 0 and 1. Combining the results of the two cases, the momentum at time $t + \Delta t$ is: $\boldsymbol{p}(t + \Delta t) = \left(1 - \frac{\Delta t}{\tau}\right)[\boldsymbol{p}(t) + -e\boldsymbol{E}\Delta t] + \frac{\Delta t}{\tau}(-e\boldsymbol{E}\alpha\Delta t)$. After dividing the equation by Δt and take the limit $\Delta t \to 0$, we obtain the equation of motion of a free electron with mass m_0 under the influence of the E-field of the light:

$$\frac{\mathrm{d}\boldsymbol{p}}{\mathrm{d}t} + \frac{\boldsymbol{p}}{\tau} = -e\boldsymbol{E}. \tag{21}$$

By using $\boldsymbol{p} = m_0\boldsymbol{v} = m_0\frac{\mathrm{d}\boldsymbol{x}}{\mathrm{d}t}$ and $\gamma = 1/\tau$, it can be expressed as

$$m_0\frac{\mathrm{d}^2\boldsymbol{x}}{\mathrm{d}t^2} + m_0\gamma\frac{\mathrm{d}\boldsymbol{x}}{\mathrm{d}t} = -e\boldsymbol{E}. \tag{22}$$

The analysis above reveals that the collision process between the free electrons and the ions is represented by a frictional damping term in the equation of motion. One can see that the form of the equation of motion (Equation (22)) for the free electron is the same as the one for the bound electron (Equation (18)), except that there is no restoring force term. As a result, for solving solution of Equation (22), we can following the same steps as solving Equation (18), and the complex dielectric constant ε_r for free electrons is

$$\varepsilon_{r,\mathrm{free}}(\omega) = \varepsilon_\infty - \frac{\omega_p^2}{\omega^2 + i\gamma\omega}, \tag{23}$$

where

$$\omega_p = \sqrt{\frac{Ne^2}{\varepsilon_0 m_0}} \tag{24}$$

is known as the plasma frequency of the free electron gas. For doped semiconductor, the dielectric constant still has the form of Equation (23) but the mass m_0 in the plasma frequency (Equation (24)) should be replaced by the effective mass m^*, which accounts for the effect of the periodic potential the electrons experiences and the band structure of the electrons, according to the effective mass theory [68].

By solving Equation (21) with specific solution form $\boldsymbol{p}(\boldsymbol{r},t) = \boldsymbol{p_0}(\boldsymbol{r})\mathrm{e}^{-i\omega t}$, we obtain: $\boldsymbol{p_0}(\boldsymbol{r}) = \frac{-e\tau}{1-i\omega\tau}\boldsymbol{E_0}(\boldsymbol{r})$. Because (the complex amplitude of) the current

density can be expressed as $\boldsymbol{J_0}(\boldsymbol{r}) = -Ne\boldsymbol{v_0}(\boldsymbol{r}) = -Ne\boldsymbol{p_0}(\boldsymbol{r})/m_0$, or from the ohm's law (Equation (17)) $\boldsymbol{J_0}(\boldsymbol{r}) = \sigma(\boldsymbol{k}, \omega)\boldsymbol{E_0}(\boldsymbol{r})$. Combining these results, we obtain the AC conductivity of the free electron gas:

$$\sigma(\omega) = \frac{Ne^2\tau}{m_0}\frac{1}{1 - i\omega\tau}. \tag{25}$$

Comparing this with Equation (23), one can find the dielectric constant of the free electron can be expressed in term of the AC conductivity by

$$\varepsilon_{r,\text{free}}(\omega) = \varepsilon_\infty + \frac{i\sigma(\omega)}{\varepsilon_0\omega}. \tag{26}$$

This result reveals that the optical response of the free electrons, which contribute the conductivity to the system, is to add the term $\frac{i\sigma(\omega)}{\varepsilon_0\omega}$ to the background dielectric constant ε_∞. This argument is consistent with the general approach by the use of the (monochromatic plane wave related) Maxwell's equations (9) - (12) and constitutive relations (15) - (17). Assume that the material studied is non-magnetic so that $\mu_r(\mathbf{k}, \omega) = 1$ and that the dielectric constant $\varepsilon_r(\mathbf{k}, \omega)$ in the constitutive relation $\mathbf{D}(\mathbf{r}) = \varepsilon_0\varepsilon_r(\mathbf{k}, \omega)\mathbf{E}(\mathbf{r})$ (Equation (15)) is limited to the insulating part of the material (bound electrons) only so that $\varepsilon_r(\mathbf{k}, \omega) = \varepsilon_{r,\text{insul}}(\mathbf{k}, \omega)$. If the material contains free electrons, it will have a conductivity $\sigma(\mathbf{k}, \omega)$ which is related to the current density through the ohm's law $\mathbf{J}(\mathbf{r}) = \sigma(\mathbf{k}, \omega)\mathbf{E}(\mathbf{r})$ (Equation (17)). Substituting Equations (15) and (16) into the Faraday's law (9) and Maxwell corrected Ampere's law (10) respectively, and applying ∇ operator to the both sides of the first equation, and then substituting $\nabla \times \mathbf{B}(\mathbf{r})$, obtained by rearranging the second equation, into the first equation, and finally using the Ohm's law (17), we have

$$\nabla \times \nabla \times \mathbf{E}(\mathbf{r}) = \frac{\omega^2}{c^2}\left(\varepsilon_{r,\text{insul}} + \frac{i\sigma(\mathbf{k},\omega)}{\varepsilon_0 \omega}\right)\mathbf{E}(\mathbf{r}). \tag{27}$$

Using the vector identity $\nabla \times \nabla \times \mathbf{E}(\mathbf{r}) = \nabla\big(\nabla \cdot \mathbf{E}(\mathbf{r})\big) - \nabla^2\mathbf{E}(\mathbf{r})$ and the Gauss's law (11), assuming the transient behaviour of the free charge can be ignored so the accumulated free charge disappear (i.e. $\rho = 0$) [60], Equation (27) become

$$\nabla^2\mathbf{E}(\mathbf{r}) = -\frac{\omega^2}{c^2}\left(\varepsilon_{r,\text{insul}}(\mathbf{k},\omega) + \frac{i\sigma(\mathbf{k},\omega)}{\varepsilon_0 \omega}\right)\mathbf{E}(\mathbf{r}). \tag{28}$$

Equation (28) has the same form of the electromagnetic wave equation in insulating material, if we express the terms in the bracket by a single term [67, 69]

$$\varepsilon_{tot}(\mathbf{k},\omega) = \varepsilon_{r,\text{insul}}(\mathbf{k},\omega) + \frac{i\sigma(\mathbf{k},\omega)}{\varepsilon_0 \omega}. \tag{29}$$

This complex total dielectric constant $\varepsilon_{tot}(\mathbf{k},\omega)$ shows that the free electron contribution to the dielectric constant is the term $\frac{i\sigma(\mathbf{k},\omega)}{\varepsilon_0 \omega}$, which is consistent with the result of the Drude model, Equation (26).

2.2.2.3 Lorentz-Drude (LD) Model

By summarizing above results about the complex dielectric constant of bound electrons (Equation (20)) and free electrons (Equations (23) or (26)), the dielectric constant of a material exhibiting not only free-electron but also bound-electron type of behaviour is

$$\varepsilon_r(\omega) = \varepsilon_\infty + \sum_j \frac{f_j^2}{\omega_{0,j}^2 - \omega^2 - i\gamma\omega} - \frac{\omega_p^2}{\omega^2 + i\gamma\omega}, \tag{30}$$

which is known as the Lorentz-Drude (LD) model [65, 70-72], where the second term refers to the effect associated with interband transition of bound electrons and the third term is due to intraband transition of conduction electrons.

2.2.2.4 Lorentz Model for Transverse Optical Phonons

Beside electrons, the phonons, the quantized lattice vibrational modes, can also interact with light strongly and the optical effect should be introduced into the complex dielectric constant ε_r. Experiments show that polar crystals absorb light strongly when the frequency of light is close to the frequency of the transverse optical (TO) phonons, just like the case for bound electrons which can absorb light at certain frequencies, as mentioned in the Section 2.2.2.1. By analogy to the bound electrons, the Lorentz's oscillator model can be used for the modelling of the interaction between light and the TO phonons. It can be shown that [64] the dielectric constant due to the TO phonons is

$$\varepsilon_{r,\mathrm{TO}} = \varepsilon_\infty + \frac{Nq^2}{\varepsilon_0 \mu} \frac{1}{\omega_{\mathrm{TO}}^2 - \omega^2 - i\gamma\omega}, \tag{31}$$

which is the same form as the for bound electrons (Equation (20)), with ω_0 replaced by the TO phonon frequency ω_{TO}, $-e$ replaced by the effective charge per ion q, and m_0 replaced by μ, which is the reduced mass of the ion-pair.

2.2.2.5 Kramers-Kronig (KK) Relations

The real part and imaginary part of the complex-valued dielectric constant $\varepsilon_r(=\varepsilon_r' + i\varepsilon_r'')$ are associated with different optical effects. For example, for low absorbing materials, the real part ε_r' corresponds to the refractive index of the materials and the imaginary part ε_r' determines the absorption of light by the materials. It is found that these two parameters are not independent on each other. For example, a semiconductor having a higher refractive index tends to have a smaller bandgap [64]. The dependence between these two seemingly unrelated parameters can be explained by the Kramers-Kronig (KK) relations [65, 73-75]. The KK relations are derived not by physical grounds but based on complex number analysis with the assumptions of causality and linear response system ($\boldsymbol{P} = \varepsilon_0[\varepsilon_r(\omega) - 1]\boldsymbol{E}$). The dependence between the real and imaginary parts of $\varepsilon_r(\omega)$ are therefore related with each other by:

$$\varepsilon_r'(\omega) = 1 + \frac{2}{\pi} P \int_0^{\infty} \frac{\omega' \varepsilon_r''(\omega')}{\omega'^2 - \omega^2} d\omega', \tag{32}$$

and

$$\varepsilon_r''(\omega) = -\frac{2\omega}{\pi} P \int_0^{\infty} \frac{\varepsilon_r'(\omega') - 1}{\omega'^2 - \omega^2} d\omega', \tag{33}$$

where *P* represents the Cauchy principal value of the integral. The KK relations (32) and (33) allow us to find the real part $\varepsilon_r'(\omega)$ if the value of $\varepsilon_r''(\omega)$ for all frequency range is known, and vice versa.

2.2.3 Fresnel Coefficients

The Fresnel reflection and transmission coefficients, i.e., r and t respectively, relate the amplitude of reflected and transmitted E-field to the incident E-field in a plane separating two different media. These coefficients can be calculated from the complex dielectric constant described in the Section 2.2.2. The Fresnel reflection coefficient is important in theoretical modelling [76, 77] (Section 2.6) of imaging process in s-SNOM and also important in predicting the dispersion relation of electromagnetic modes in materials such as surface plasmon polaritons in semimetal [78], surface phonon polaritons in polar crystal [43, 78] and waveguide modes in transition metal dichalcogenides [48, 50, 79, 80] (TMDCs). One of the important applications of s-SNOM is real-space imaging of these modes [41-43, 45, 46, 48, 50, 51, 81] and thus a brief introduction to the Fresnel coefficients will be presented here. The method of calculating dispersion relations of electromagnetic modes from Fresnel coefficient will be presented in Section 2.2.5.

2.2.3.1 Single interface

We consider the simplest case for reflection and transmission problem, which is monochromatic plane wave with wavevector $\mathbf{k}_\mathrm{i}$ incident on single interface between two isotropic media (denoted as i) with different (complex) refractive index $n_\mathrm{i} = \sqrt{\varepsilon_\mathrm{i}\mu_\mathrm{i}}$. The magnitude of $\mathbf{k}_\mathrm{i}$ is $k_\mathrm{i} = n_\mathrm{i}k_0 = \sqrt{\varepsilon_\mathrm{i}\mu_\mathrm{i}}k_0$, where k_0 is the wavenumber in free space. For more complex wave, the problem can be analysed by expressed the incident wave by a superposition of monochromatic plane wave.

The cases of s-polarised and p-polarised light should be analysed separately. s-polarisation means the polarization of the plane wave is perpendicular to the plane of incidence, while p-polarisation means that it is parallel to that plane. Figure 1 shows the geometry of these independent situation, where $\mathrm{E}_1^{(\mathrm{s,p})}$ is the s/p-polarized incident E-field from media 1, $\mathrm{E}_{1\mathrm{r}}^{(\mathrm{s,p})}$ is the reflected field and $\mathrm{E}_2^{(\mathrm{s,p})}$ is the transmitted field. $\mathbf{k}_1$, $\mathbf{k}_{1\mathrm{r}}$ and $\mathbf{k}_2$ are the wavevector of the corresponding field. After fulfilling the boundary conditions of the B-field and E-field, implied from Maxwell's equations, the Fresnel reflection and transmission coefficients can be obtained [82, 83]:

$$r_{\mathrm{s}} = \frac{\mathrm{E}_{1\mathrm{r}}^{(\mathrm{s})}}{\mathrm{E}_1^{(\mathrm{s})}} = \frac{\mu_2 k_{\mathrm{z}_1} - \mu_1 k_{\mathrm{z}_2}}{\mu_2 k_{\mathrm{z}_1} + \mu_1 k_{\mathrm{z}_2}}, \qquad r_{\mathrm{p}} = \frac{\mathrm{E}_{1\mathrm{r}}^{(\mathrm{p})}}{\mathrm{E}_1^{(\mathrm{p})}} = \frac{\varepsilon_2 k_{\mathrm{z}_1} - \varepsilon_1 k_{\mathrm{z}_2}}{\varepsilon_2 k_{\mathrm{z}_1} + \varepsilon_1 k_{\mathrm{z}_2}}, \tag{34}$$

$$t_{\mathrm{s}} = \frac{\mathrm{E}_2^{(\mathrm{s})}}{\mathrm{E}_1^{(\mathrm{s})}} = \frac{2\mu_2 k_{\mathrm{z}_1}}{\mu_2 k_{\mathrm{z}_1} + \mu_1 k_{\mathrm{z}_2}}, \qquad t_{\mathrm{p}} = \frac{\mathrm{E}_2^{(\mathrm{p})}}{\mathrm{E}_1^{(\mathrm{p})}} = \frac{2\varepsilon_2 k_{\mathrm{z}_1}}{\varepsilon_2 k_{\mathrm{z}_1} + \varepsilon_1 k_{\mathrm{z}_2}} \sqrt{\frac{\mu_2 \varepsilon_1}{\mu_1 \varepsilon_2}}, \tag{35}$$

where $k_{\mathrm{z_i}}$ is the magnitude of the out-of-plane wavenumber of the plane wave in medium i, having a relation with the magnitude of in-plane wavenumber $k_{\parallel}$

$$k_{\mathrm{z_i}} = \sqrt{k_{\mathrm{i}}^2 - k_{\parallel}^2} = \sqrt{\varepsilon_{\mathrm{i}} \mu_{\mathrm{i}} k_0^2 - k_{\parallel}^2}, \tag{36}$$

where $k_{\parallel}$ is conserved along the surface, which is a consequence of fulfilling the boundary conditions. Equations (34) and (35) can be extended to the case there is a 2D material such as graphene along the interface. The forms and deviation can be found in reference [78]. In addition, for anisotropic materials, the forms of Fresnel's coefficients can be found in references [82] and [84].

In Section 2.2.2, the concept of complex dielectric constant is introduced. It reveals that the Fresnel's coefficients (34) and (35) can also be complex, indicating that there can be a phase shift of the incident light relative to the reflected and transmitted light.

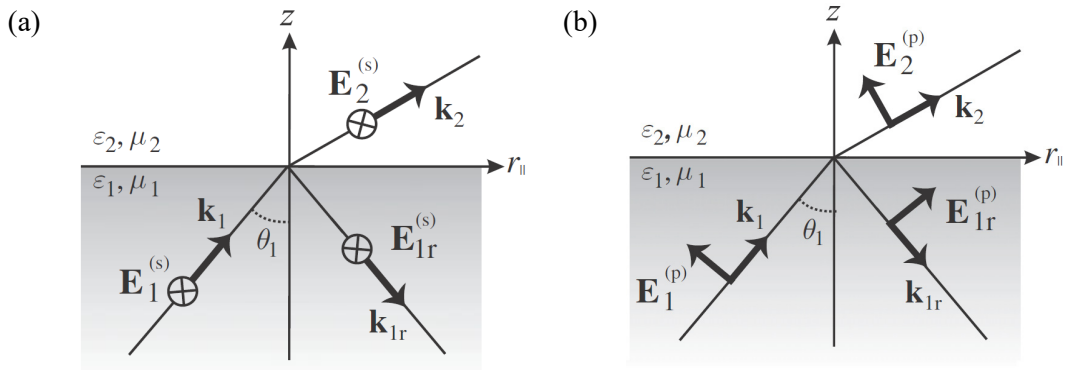

Figure 1. A plane wave with (a) s-polarisation and (b) p-polarisation is incident on an interface between two media. (Images taken from reference [69].)

2.2.3.2 Multi-layer System (Transfer-Matrix Method)

As mentioned above, Fresnel equations are important for the theoretical modelling of the light-matter interaction during the imaging process of s-SNOM (Section 2.6). While pervious Section focuses only on single-layer system, s-SNOM is usually applied to characterise multi-layer system. This Section will discuss using the transfer-matrix (T-matrix) method to find the Fresnel coefficients in multi-layer structure [47, 82, 85].

The Fresnel coefficients for N-layer structure can be found from the total T-matrix $\mathbf{T}_{\mathrm{tot}}$ which is expressed as

$$\mathbf{T}_{\mathrm{tot}} = \begin{pmatrix} T_{11}^{tot} & T_{12}^{tot} \\ T_{21}^{tot} & T_{22}^{tot} \end{pmatrix} = \prod_{\mathrm{i}=1}^{N-2} (\mathbf{T}_{\mathrm{i}\to\mathrm{i}+1} \cdot \mathbf{P}_{\mathrm{i}+1}) \cdot \mathbf{T}_{\mathrm{N}-1\to\mathrm{N}}. \tag{37}$$

$\mathbf{T}_{\mathrm{i}\to\mathrm{i}+1}$ is the transfer-matrix for i/i+1 interface, which relates the amplitudes of the EM-field in layer i and layer i+1 at the interface. $\mathbf{P}_{\mathrm{i}}$ is called propagation matrix, which accounts for the amplitude change due to the phase shift during the light propagating within the layer i. The expression of transfer-matrix and propagation matrix are

$$\mathbf{T}_{\mathrm{i}\to\mathrm{i}+1} = \frac{1}{t_{\mathrm{i}\to\mathrm{i}+1}^{(p,s)}} \begin{pmatrix} 1 & r_{\mathrm{i}\to\mathrm{i}+1}^{(p,s)} \\ r_{\mathrm{i}\to\mathrm{i}+1}^{(p,s)} & 1 \end{pmatrix}, \qquad \mathbf{P}_{\mathrm{i}} = \begin{pmatrix} e^{-jk_{\mathrm{z_i}}d_{\mathrm{i}}} & 0 \\ 0 & e^{jk_{\mathrm{z_i}}d_{\mathrm{i}}} \end{pmatrix}, \tag{38}$$

where $r_{\mathrm{i}\to\mathrm{i}+1}^{(p,s)}$ and $t_{\mathrm{i}\to\mathrm{i}+1}^{(p,s)}$ are the Fresnel coefficients in single i/i+1 interface, given by Equations (34) and (35). $k_{\mathrm{z_i}}$ is the out-of-plane wavenumber, given by Equation (36), and d_{i} is the thickness of layer i. The symbol j is used to denote the imaginary unit to avoid confusion with the layer index i. Finally, the Fresnel coefficients for N-layer structure are

$$r_{(p,s)} = \frac{T_{21}^{tot}}{T_{11}^{tot}}, \qquad t_{(p,s)} = \frac{1}{T_{11}^{tot}}. \tag{39}$$

For example, for 3-layer system, according to equation (37), $\mathbf{T}_{\mathrm{tot}} = \mathbf{T}_{1\to2} \cdot \mathbf{P}_2 \cdot \mathbf{T}_{2\to3} = \frac{1}{t_{1\to2}^{(p,s)}} \frac{1}{t_{2\to3}^{(p,s)}} \begin{pmatrix} e^{-jk_{\mathrm{z_2}}d_2} + r_{1\to2}^{(p,s)} r_{2\to3}^{(p,s)} e^{jk_{\mathrm{z_2}}d_2} & r_{2\to3}^{(p,s)} e^{-jk_{\mathrm{z_2}}d_2} + r_{1\to2}^{(p,s)} e^{jk_{\mathrm{z_2}}d_2} \\ r_{1\to2}^{(p,s)} e^{-jk_{\mathrm{z_2}}d_2} + r_{2\to3}^{(p,s)} e^{jk_{\mathrm{z_2}}d_2} & r_{1\to2}^{(p,s)} r_{2\to3}^{(p,s)} e^{-jk_{\mathrm{z_2}}d_2} + e^{jk_{\mathrm{z_2}}d_2} \end{pmatrix}$.

The Fresnel coefficients can be calculated by Equation (39):

$$r_{(p,s)}^{3-\text{layer}} = \frac{r_{1\to2}^{(p,s)} + r_{2\to3}^{(p,s)} e^{2jk_{z_2}d_2}}{1 + r_{1\to2}^{(p,s)} r_{2\to3}^{(p,s)} e^{2jk_{z_2}d_2}}, \qquad t_{(p,s)}^{3-\text{layer}} = \frac{t_{1\to2}^{(p,s)} t_{2\to3}^{(p,s)} e^{jk_{z_2}d_2}}{1 + r_{1\to2}^{(p,s)} r_{2\to3}^{(p,s)} e^{2jk_{z_2}d_2}}. \quad (40)$$

Equation (40) can be used to generalise to N-layer result, or one can directly calculate it by Equations (37)-(39).

2.2.4 Evanescent wave

A electromagnetic plane wave has the form $\mathbf{E}(\mathbf{r}) = \mathbf{E}(\mathbf{k}, \omega)\mathrm{e}^{i\mathbf{k}\cdot\mathbf{r}}$ (Equation (14)), where the wavevector $\mathbf{k} = k_x\hat{x} + k_y\hat{y} + k_z\hat{z}$. For propagating wave, all of the three components are real. In contrast, if at least one of the components of $\mathbf{k}$, for example, the z-component, is imaginary so that $\mathbf{k} = k_x\hat{x} + k_y\hat{y} + ik_z\hat{z}$, the plane wave now has the form

$$\mathbf{E}(\mathbf{r}) = \mathbf{E}(\mathbf{k}, \omega)\mathrm{e}^{i\mathbf{k}_\parallel\cdot\mathbf{r}_\parallel}\mathrm{e}^{-k_z z}, \quad (41)$$

where k_z is real. Equation (41) reveals that the plane wave now does not propagate in z-direction, but decays exponentially instead. As a result, the electromagnetic energy is restricted to a space with subwavelength scale in this direction. This type of wave is called evanescent wave.

The term near-field is used to describe this exponentially decaying field, in contrast to the term far-field which refers to the field far enough away from any material inhomogeneities. Actually material inhomogeneity is necessary for the existence of evanescent wave [61, 69]. Examples of evanescent wave includes the field in the interface in which total internal reflection occurs and the electromagnetic surface

modes in graphene, h-BN and TMDCs. Evanescent wave is important in nano-optics and has been employed in near-field imaging technique, which will be discussed in the Section 2.4.

2.2.5 Dispersion relation of electromagnetic modes

The dispersion relation $\omega(k_{\parallel})$ of electromagnetic surface and waveguide modes are the spectrum showing the angular frequency ω dependency with the in-plane wavenumber $k_{\parallel}$ of the modes. This curve can show the possibility of exciting these modes within a range of angular frequency, and thus is an important concept for employing s-SNOM to perform real-space imaging of these modes.

2.2.5.1 The Eigenequation

The condition for the existence of the electromagnetic surface mode can be found by finding the particular solutions (modes), of the form Equation (41), satisfying the Maxwell's Equations (9)-(12) or simply the wave Equations (28) and (29). By imposing suitable boundary conditions, an eigenequation can be obtained, from which the dispersion relation $\omega(k_{\parallel})$ of the modes can be determined [78, 80, 86, 87]. Alternatively, the same eigenequation can be obtained by finding the condition of the pole of Fresnel reflection coefficient $r_{(p,s)}$ (Equation (39)), that is, by setting denominator of $r_{(p,s)}$ to be zero [69, 78]. The pole of r_p (r_s) refers to TM (TE) modes.

However, the extraction of dispersion relation from the eigenequation cannot be done analytically and numerical methods must be used, which is more difficult and time-consuming. Also, for material having complex dielectric constant (Equation (29)), the eigenequation has no solution for real ω [88, 89], which is impractical. As a result, a wiser method for determining the dispersion spectrum is required, as will be discussed in the following section.

2.2.5.2 Loss function

Inspired by the fact that the pole of $r_{(\mathrm{p,s})}$ indicates the condition of existence of EM modes, a function is defined for the purpose of calculating the dispersion curve:

$$L(k_{\parallel}, \omega) = \mathrm{Im}\left(r_{(\mathrm{p,s})}\right), \tag{42}$$

which is called the loss function, because it is related to the energy loss during the optical excitation of the EM modes. The excitation of long-live modes corresponds to high loss in energy. Therefore, the peaks of $L(k_{\parallel}, \omega)$ refer to the excitation of surface modes and the plot of $L(k_{\parallel}, \omega) = \mathrm{Im}\left(r_{(\mathrm{p,s})}\right)$ recovers the dispersion relation $\omega(k_{\parallel})$ [78]. The method produces the same dispersion curve as by solving the eigenequations by time-consuming numerical method. Ones only need to find the dielectric constant ε (Equation (29)), and it in turn can determine the Fresnel reflection coefficients $r_{(\mathrm{s,p})}$. By plotting the imaginary part of $r_{(\mathrm{s,p})}$, the dispersion relation $\omega(k_{\parallel})$ can be obtained.

2.3 Resolution Limit of Far-Field Optical Microscope

In far-field (classical) optical microscopy, propagating electromagnetic wave is used for imaging tiny objects. The dispersion relation of a propagating photon in medium i is $\omega = ck_i$, where

$$k_i = \sqrt{{k_x}^2 + {k_y}^2 + {k_z}^2} = n_{\mathrm{i}} k_0 = \frac{2\pi}{\lambda_i} \tag{43}$$

is the wavenumber of the light in medium i. n_{i} is the refractive index, λ_i are wavelength in medium i, ω is the angular frequency and k_0 is the wavenumber in free space. Applying Heisenberg's uncertainty principle to a photon, its momentum and position in x-space have the relation

$$\Delta p_x \cdot \Delta x \geq \frac{\hbar}{2}. \tag{44}$$

After rearranging terms and using the relation $p_x = \hbar k_x$, Equation (44) becomes

$$\Delta x \geq \frac{1}{2\Delta k_x}, \tag{45}$$

where Δx and Δk_x measure the uncertainty of position and momentum of the photon in x-direction. Equation (45) shows that a photon has a certain uncertainty in position, which is inversely proportional to the uncertainty of momentum in respective direction. For a propagating photon, k_x, k_y and k_z are real number. Equation (43) shows the possible range of k_x (also k_y and k_z) is $0 < k_x < k_i$. For limiting case that the uncertainty of k_x covers the full possible range, that is $\Delta k_x = k_i$, Equation (45) becomes

$$\Delta x \geq \frac{\lambda_i}{4\pi}. \tag{46}$$

Equation (46) reveals the minimum spatial uncertainty $\Delta x_{\min} = \frac{\lambda_i}{4\pi}$, which is of the order of wavelength of the photon. In order words, the image of a propagating photon will be blurred. If considering real imaging system containing real lens, the minimum resolvable separation $\Delta x_{\min}$ should be [21, 22, 69]

$$\Delta x_{\min} = \frac{0.61\lambda_i}{\mathrm{NA}} \tag{47}$$

for uniform illumination and within the Rayleigh criterion [61], where $\mathrm{NA} = n_i \sin 2\theta_{\max}$ is numerical aperture. $2\theta_{\max}$ is the maximum angle for collecting light. By substituting suitable NA value of common classical imaging system into Equation (47), we can see that the minimum separation of two point sources $\Delta x_{\min} \sim \frac{\lambda_i}{2}$, as mentioned above.

2.4 Near-Field Imaging

While conventional optical microscope measures light-matter interaction by using propagating electromagnetic wave, E. H. Synge [90], after discussing with A. Einstein [91], in 1928 suggested using near field (Section 2.2.4) to break the diffraction limit so that nano-imaging can be performed. The limitation of technology level prevented scientists to achieve Synge's idea at that time. Nowadays near-field optical microscope (SNOM) is widely employed to take image at subwavelength scale.

2.4.1 Imaging Beyond the Diffraction Limit

Subwavelength imaging can be achieved by employing near field (evanescent wave). Section 2.2.4 has mentioned the wavevector $\mathbf{k}_\mathrm{i}$ of evanescent wave in medium i has at least one imaginary component so that $\mathbf{k}_\mathrm{i} = k_x\hat{x} + k_y\hat{y} + ik_z\hat{z}$. As a result, Equation (43) becomes $k_i = \sqrt{{k_x}^2 + {k_y}^2 - {k_z}^2}$, which implies the maximum value of k_x can be larger than k_i. According to Equations (45) and (46), the minimum spatial uncertainty $\Delta x_{\min}$ for a point source can be much smaller than $\frac{\lambda_i}{4\pi}$ now, thereby improving the spatial resolution to subwavelength dimension [57, 58].

2.4.2 Scanning Near-Field Optical Microscope (SNOM)

Scanning Near-Field Optical Microscope (SNOM) is a state-of-art technique to perform near-field imaging. Image process relies on scanning probe microscopy (SPM). During imaging, a probe, placed in close proximity with the sample, scans the sample and related optical information in each pixel can be obtained. SNOM is a technique combining SPM with optical measurement system so that nano-imaging can be performed.

2.4.2.1 Aperture - SNOM

The earliest successful application of SNOM [92, 93] relied on aperture-type probe, using optical fibre tip in which there is a small aperture in the apex. When

passing light through the aperture, a strong near field with size in subwavelength scale will be confined near the probe tip. Near-field interaction occurs when the tip is put in close proximity with the sample during scanning and then optical image is obtained after analysing the near-field signal. Figure 2(a) demonstrates the schematic diagram of aperture-SNOM (a-SNOM).

Smaller aperture favours higher image resolution but suffering from high power loss. Moreover, this power loss effect is severer for larger wavelength [22]. Therefore, application of a-SNOM is restricted to visible and near-field range, but not MIR. Practically, the resolution of a-SNOM for visible light is about 100 nm.

2.4.2.2 Scattering (Apertureless) – SNOM

An improved version of SNOM is the scattering-SNOM (s-SNOM) [59, 94-97] in which an atomic force microscope (AFM) tip is used as the scanning probe. Focused laser is incident on the tip apex and generate a strong near field near the tip apex with subwavelength dimension. When the tip is scanning and placed in close proximity with the sample, near-field scattering occurs and generate far-field scattering signal which in turn creates a near-field image. Figure 2(b) demonstrates the schematic diagram of s-SNOM. The resolution of s-SNOM is of the same order with the size of tip apex and therefore is wavelength-independent. Therefore, unlike aperture-SNOM, scattering-SNOM is available for MIR application and also offers higher imaging resolution.

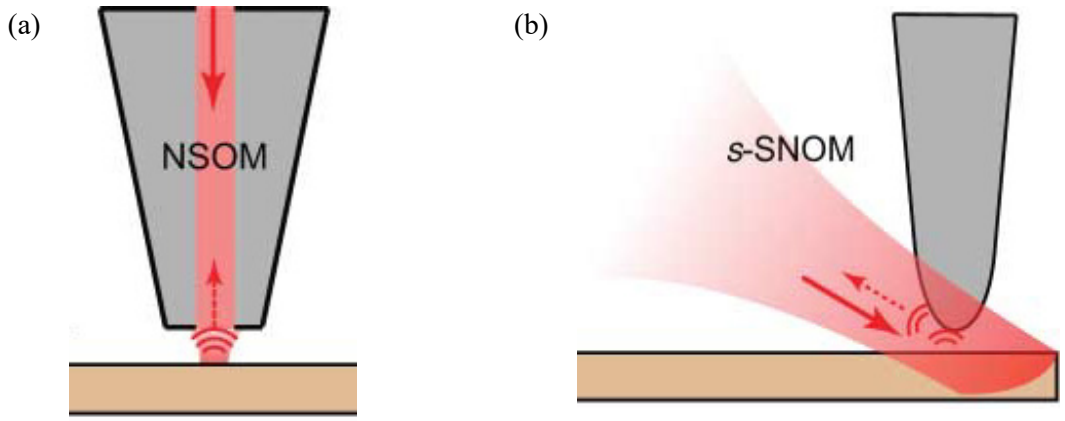

Figure 2. Schematic diagram of SNOM with (a) aperture-type probe and (b) scattering probe. (images taken from reference [22].)

2.5 Working Principle of Elastic s-SNOM

Scattering (Apertureless) – SNOM can be classified into elastic and inelastic s-SNOM, depending on the scattering type in the AFM tip when it is placed in close proximity with a material surface and then a laser beam is focused on its apex. In this project, elastic s-SNOM was employed, in which the scattering, induced by near-field interaction, is elastic.

When the AFM tip is illuminated by focused light during scanning, the sharp tip can concentrate the incident light and create a strong near-field adjacent to the apex. This can be shown by simulation from different groups [25, 98, 99]. This field-localization, with size typically on the order of the tip radius, is caused by the geometric effect (i.e. the probe) [99-102]. Figure 3 shows a simulated field intensity distribution near the tip apex, which is performed by Novotny's group [98]. It has been shown that only p-polarized light, rather than s-polarized light, can induce this near-field spot [95, 98]. During scanning, the tip is placed in close proximity with the

sample surface, and there is a near-field interaction between the tip and sample. This tip-sample interaction is strongly dependent on the local optical property (complex dielectric constant) of the sample and this interaction can generate scattering light to far field, resulting in optical contrast in the image. This type of scattering is called near-field scattering. If metal-coated or dielectric tip is used and is in off-resonant case, the near-field enhancement is weaker than when metal tip is used [103]. The scattering is elastic in this case and this is the case in elastic s-SNOM [22]. In contrast, if metal or resonant tip is used, the scattering in inelastic and this is inelastic s-SNOM. Elastic s-SNOM is widely applied for real-space imaging with nanoscopic spatial resolution, while inelastic s-SNOM is employed for tip-enhanced spectroscopy such as tip-enhanced Raman spectroscopy (TERS) [104-108].

Monochromatic p-polarized light should be focused on the tip apex to induce near-field. This is achieved by using a focusing mirror such as parabolic mirror. Apart from usage of focusing light to the tip apex, the same parabolic mirror in s-SNOM is also used to collect the near-field backscattering light. This set-up can reduce the difficulty in optical alignment. Figure 2 shows that in s-SNOM the focused incident light and the collected near-field scattering light signal are parallel to each other so that only one parabolic mirror is capable of focusing and the collection of light.

Even one can find a best position and orientation of the parabolic mirror, the finite spot size due to diffraction effect (~4 μm for MIR light and ~3 μm for NIR light) inevitably illuminates not only the tip apex, but also the sample and the tip shaft. These illuminated positions generate Rayleigh scattering to far-field, which contributes an unwanted background scattering signal. This is the main source of noise in the detected signal. For elastic s-SNOM, the near-field scattering is weak, compared to this

background scattering, and thus an effective background suppression scheme is required. Section 2.7 will discuss about it.

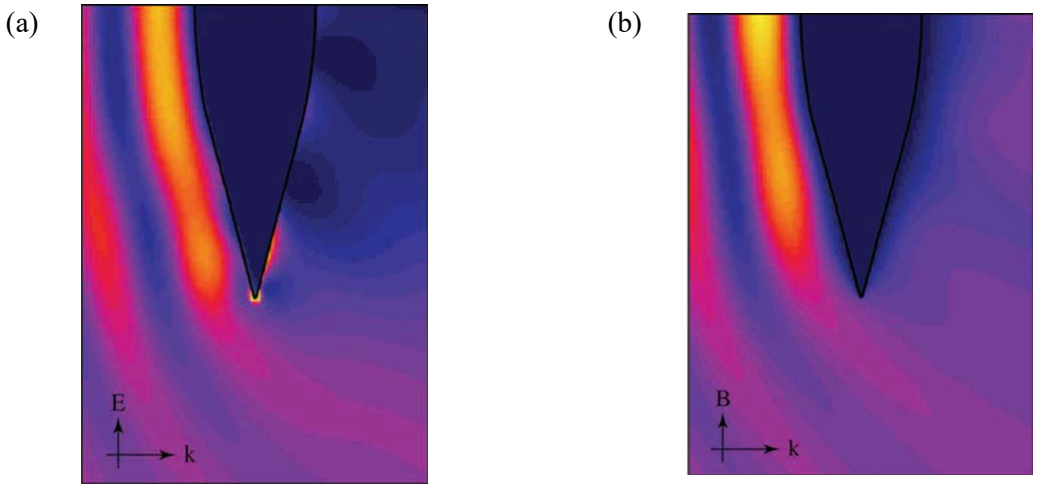

Figure 3. Simulated field intensity distribution [98] in the gold tip apex with (a) p-polarized and (b) s-polarized visible light illumination. Only the p-polarized light can induce near field enhancement near the apex. Light is incident from left side so generating far-field standing wave pattern in the left side after superposing with reflected light from the tip. (Images taken from reference [98].)

2.6 Theoretical Model of Light-Matter Near-Field Scattering in s-SNOM

For s-SNOM, the meaningful signal is the backscattering light from the tip apex, generated by the near-field interaction between the illuminated tip and sample when their separation is in the same order of the apex diameter, as shown in Figure 4(a). The near-field interaction strongly depends on the local optical property of the

sample, and so does the backscattered light. This process can be expressed mathematically:

$$E_{\mathrm{s,nf}} = \sigma_{\mathrm{nf}} E_{\mathrm{i}}, \tag{48}$$

where

$$\sigma_{\mathrm{nf}} = s_{\mathrm{nf}} e^{i\phi_{\mathrm{nf}}}. \tag{49}$$

$E_{\mathrm{s,nf}}$ is the E-field of backscattered light generated by the near-field interaction between the tip and the sample while E_{i} is the E-field of the light incident on the tip apex. Both of them are complex value. The ratio between them is the complex-valued near-field scattering coefficient σ_{nf}, having modulus s_{nf}, which is called near field amplitude. The fact that σ is a complex number implies there may be a phase difference between the scattering field $E_{\mathrm{s,nf}}$ and the incident field E_{i}. This phase difference is equal to the phase of σ_{nf}, that is, ϕ_{nf}, which is called the near-field phase. The use of s-SNOM is to measure both s_{nf} and ϕ_{nf} simultaneously.

An understanding of near-field interaction in the tip-sample system is required for correctly interpreting the output signal. Equation (49) shows that if the mathematical form of coefficient σ_{nf} can be found, the optical signal can be predicted. Analytical calculation of σ_{nf} from real geometry by full electrodynamic approach [109] is very complicated and numerical calculation [76, 88, 99, 102, 110] may also be time-consuming and unpractical. Therefore, two common analytical models with suitable approximation, point dipole and finite dipole models, will be introduced here.

2.6.1 Point Dipole (DP) Model

Point-dipole (DP) model [26, 96, 111-113] is the simplest analytical model to calculate the complex-valued near-field scattering coefficient σ_{nf}. It was applied in earlier [24, 25, 114, 115] s-SNOM experiments and even in recently years [53, 54] for 2D materials, due to its simplicity and qualitative agreement with the results. In this section, DP model for isotropic materials will be introduced.

Figure 4(b) shows the schematic diagram of DP model in which the AFM tip is modelled as a polarizable sphere with the same dielectric constant ε_t as the tip material and with radius a matched with the radius of curvature of the tip apex. The incident EM-field induces charge redistribution in the sphere, thereby polarizing the sphere. For typical AFM tip, radius a is between 20 to 100 nm, much smaller than the wavelength λ of MIR or even visible illuminating light. For such a small sphere, i.e., $a \ll \lambda$, one can apply the quasi-electrostatic approximation, and thus under uniform field irradiation the sphere responses as a point dipole (ideal dipole) in its centre [65]. The dipole moment of this point dipole is $\boldsymbol{p} = \alpha\left[\left(1 + r_p\right)\boldsymbol{E_i}\right]$, where the term in the square bracket is the exciting field. The factor $\left(1 + r_p\right)$ corresponds to the direct illumination on the sphere (tip) and additional illumination on the sphere due to the reflection at the sample surface [77, 116, 117]. Figure 3 reveals that only p-polarized light is able to induce near-field enhancement near the apex, and thus only the z-direction of dipole moment $\boldsymbol{p}$ will be considered:

$$p_z = \alpha\left(1 + r_p\right)E_{i,z} \tag{50}$$

where α is the quasi-static bare polarizability of the sphere [65]:

$$\alpha = 4\pi a^3 \frac{\varepsilon_t - 1}{\varepsilon_t + 2}, \tag{51}$$

provided that $\boldsymbol{E_i}$ is not very strong, otherwise higher-order components may occur [60]. Within the quasi-electrostatic approximation, the tip-dipole (the polarized sphere) can generate field (in spherical coordinate) with the form [60]

$$\boldsymbol{E_{tip-dipole}} = \frac{p_z}{4\pi\varepsilon_0 r^3}\left(2\cos\theta\,\hat{r} + \sin\theta\,\hat{\theta}\right). \tag{52}$$

As shown in Figure 4(b), this dipole field will polarize the sample with dielectric constant ε_s and induce a image point dipole in the sample, which has the same direction as the tip dipole but has a different value of polarizability, $\alpha\beta$, where

$$\beta = \frac{\varepsilon_s - 1}{\varepsilon_s + 1} \tag{53}$$

is the electrostatic reflection coefficient. Equation (53) can be derived from the electrodynamic Fresnel reflection coefficient r_p in Equation (34) by substituting $k_{z_i} \approx ik_{\parallel}$ in the case $k_{\parallel} \gg k_i$ (non-radiative mode). Therefore, the image dipole has dipole moment $p_{z,image} = \beta p_z$. This image dipole produces additional field to the tip dipole. By analogy with Equation (52), the additional field to the tip dipole has value $\frac{p_{z,image}}{2\pi\varepsilon_0[2(H+a)]^3}$. As a result, Equation (50) should be modified to the form

$$p_z = \alpha\left\{(1 + r_p)E_{i,z} + \frac{\beta p_z}{2\pi\varepsilon_0[2(H+a)]^3}\right\}, \tag{54}$$

where H is the distance between the tip apex and the sample plane. After rearranging the terms, the tip dipole moment is:

$$p_z = \alpha_{\text{eff}}\left(1 + r_p\right)E_{i,z}, \tag{55}$$

with

$$\alpha_{\text{eff,PD}} = \frac{\alpha}{1 - f(H)\beta(\varepsilon)} \tag{56}$$

where

$$f(H) = \left(\frac{\varepsilon_t - 1}{\varepsilon_t + 2}\right)\frac{a^3}{4(H + a)^3}. \tag{57}$$

α_{eff} is the effective polarizability of the tip and $f(H)$ is a function depending only the distance between the tip apex and the sample plane. Comparing Equation (50) with (55), one can find that, to calculate the tip dipole moment induced by incident light, the bare polarizability of the sphere α should be replaced by the effective polarizability α_{eff} in order to account for the tip-sample near-field interaction. By using Equations (52) and (55), the expression of backscattered field is $\boldsymbol{E}_{\text{s,nf}} = \left(1 + r_p\right)\boldsymbol{E}_{\boldsymbol{tip-dipole}} = \frac{\left(1+r_p\right)^2\alpha_{\text{eff,PD}}E_{i,z}}{4\pi\varepsilon_0(H+a)^3}\left(2\cos\theta\,\hat{r} + \sin\theta\,\hat{\theta}\right)$, where the additional factor $\left(1 + r_p\right)$ corresponds to the additional signal due to the reflection of backscattered light at the sample surface [77, 116, 117]. Comparing this with Equation (48), one can finally obtain an expression of the near-field scattering coefficient

$$\sigma_{\text{nf}} \propto \left(1 + r_p\right)^2\alpha_{\text{eff}}. \tag{58}$$

The coupled dipole model can correctly predict experiment results qualitatively in some case [24, 37, 53, 114, 115, 118, 119]. This model can be extended to the case for anisotropic materials [115, 118, 120] and for thin films [53, 121]. However, this model fails to give accurate prediction in near-field resonant materials [76, 88, 110,

114, 117, 119]. Moreover, this model favours MIR over visible illumination because the quasi-electrostatic approximation requires $a \ll \lambda$. Also, it has been shown that the position of the tip dipole should be below the sphere centre, but not exactly in the centre [76]. This model also ignores the multipole contribution [76, 110, 122], the effect due to the real shape of the tip [99, 101, 102] and nonlocal (electrodynamic) effect such as retardation [121].

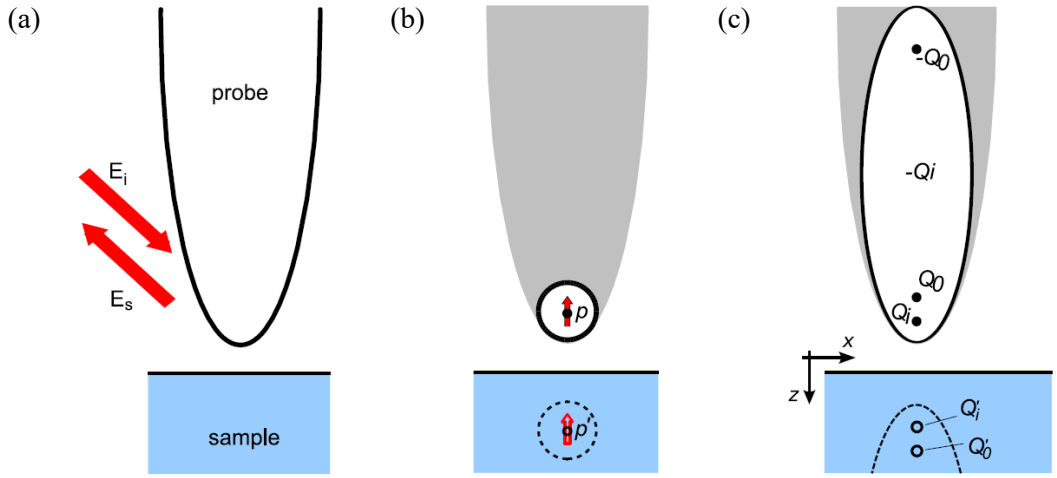

Figure 4. Schematic diagrams of modeling the near-field scattering coefficient σ_{nf}. (a) The tip-sample coupled system scatters light to far-field when it is illuminated by focused laser beam. (b) Point-dipole (PD) model. (c) Finite-dipole model. (Images taken from reference [77].)

2.6.2 Finite Dipole (FD) Model

Finite dipole (FD) model [77, 117] is a more advanced model for calculating the near-field scattering coefficient σ_{nf}. Instead of approximating the tip as a sphere in PD model, FD model replaces the tip by a spheroid to account for the geometric effect of the extended sharp of the probe [76, 101, 102]. The radius of curvature of one side

matches with the probe apex, as shown in Figure 4(c). Following calculation steps are based on the work by Cvitkovic et al [77]. The response in z-direction will only be considered because only p-polarized light is able to induce near-field enhancement near the apex, as mentioned in Section 2.5.

Assuming the effective length $2L \approx 600$ nm [117] of the spheroid is much smaller than the wavelength λ of the illuminating beam, calculation can be based on quasi-electrostatic approximation. It has been shown that electrostatically an illuminated isolated spheroid has similar near-field pattern as a finite dipole. Therefore, the spheroid is further modelled as extended dipole (finite dipole) with dipole moment $p_0 \approx 2LQ_0$, in which there are two opposite monopoles (point charges) Q_0 and $-Q_0$ situating at the distance $W_0 \approx \frac{1.31aL}{L+2a}$ [123] away from their nearest apexes, where a is the radius of curvature of the tip apex, as shown in Figure 4(c). When this dipole is near a flat sample surface, only the field from monopole Q_0 participates in the tip-sample near-field interaction, because Q_0 is much closer to the sample than $-Q_0$. The field from this point charge Q_0 will polarize the sample and this effect can be represented by a mirror point charge $Q_0' = -\beta Q_0$, which in turn induces a charge redistribution in the spheroid. This charge redistribution can be represented by an additional line charge distribution, which can be approximated by an additional finite dipole with dipole moment $p_i \approx LQ_\mathrm{i}$, which is represented by opposite charges Q_i and $-Q_\mathrm{i}$ situated $W_i = \frac{a}{2}$ from the lower apex and at the centre of the spheroid respectively, as shown in Figure 4(c). As shown in Figure 4(c), like the dipole p_0, this additional dipole p_i will also polarize the sample and induce mirror point charge $Q_\mathrm{i}' = -\beta Q_\mathrm{i}$ in the sample, which in turn influence the value of p_i. Recursively, a final value of p_i can be found. By calculating the value of point charges Q_0 and Q_i, one can find the

expression of the effective dipole moment $p_{\text{eff}} = p_0 + p_i \approx 2LQ_0 + LQ_{\text{i}}$. By using Equation (55), the effective polarizability $\alpha_{\text{eff,FD}}$ of the tip is found to be [117]

$$\alpha_{\text{eff,FD}} = C\left(2 + \frac{f_0(H)\beta(\varepsilon)}{1 - f_i(H)\beta(\varepsilon)}\right), \tag{59}$$

with

$$f_{0,i}(H) = \left(g - \frac{a + 2H + W_{0,i}}{2L}\right)\frac{\ln\left(\frac{4L}{a + 4H + 2W_{0,i}}\right)}{\ln\left(\frac{4L}{a}\right)} \tag{60}$$

and [117]

$$C = a^2 L \frac{L(\varepsilon_t - 1)\left(2L\sqrt{1 - \frac{a}{L}} + a\ln\frac{\left(\sqrt{L} - \sqrt{L - a}\right)^2}{a}\right)}{2L\sqrt{1 - \frac{a}{L}}\left((L - a\varepsilon_t) - aL(\varepsilon_t - 1)\ln\frac{\left(\sqrt{L} - \sqrt{L - a}\right)^2}{a}\right)}. \tag{61}$$

C is height-independent constant, ε_t is the dielectric constant of the tip material, H is the distance between the tip apex and the sample, and $g = 0.7e^{0.08i}$ is a complex factor that determines the value of Q_{i}. Using Equations (58) and (59), one can calculate the near-field scattering coefficient σ_{nf}.

FD model has been widely applied in s-SNOM experiments [31, 43, 124] and found to be more accurate than PD model [77, 117]. However, the applicability of FD model is limited to the case that $2L \ll \lambda$, where λ is the wavelength of the exciting laser beam. Therefore, it may be an accurate model for MIR and THz light but not for visible light. Also, FD model is a quasi-electrostatic model and thus it ignores non-local (electrodynamic) effect such as retardation effect. Moreover, it cannot be applied

for layered system [88] and an extended version [36, 123] should be used. In order to fully account for the geometric effect due to the shape of the probe and the electrodynamic effect, Porto et al [109]. has proposed a theory to give a general expression for the s-SNOM signal, by using reciprocity theorem but it is much more complicated. Recently, McLeod et al. [37] also proposed a model, called lightning rod model, to include the geometric and electrodynamic effect.

2.6.3 Finite dipole (FD) model for Thin Film

Although finite dipole (FD) model is proposed based on several approximations, it offers certain degree of accuracy and remains not very complicated. Therefore, it is widely applied for signal prediction for s-SNOM. The result of FD model in pervious section, Equation (59), is only limited to the application for bulk sample. Govyadinov et al. [36] provides an extend version of FD model which can be applied to thin film case. The concept of Govyadinov et al. is represented in Figure 5. ε_{f} and ε_{s} are dielectric constant of the thin film and substrate respectively. H is the distance between tip apex and the thin film while d_0 is the thin film thickness. The thin film system is regarded as a combination of several tip-(bulk sample) systems, as shown in Figure 5. Therefore, the effective polarizability $\alpha_{\mathrm{eff,thin}}$ for thin film system can be calculated by a summation of several $\alpha_{\mathrm{eff,bulk}}$ terms. According to Equation (59), $\alpha_{\mathrm{eff,bulk}} = C\big(2 + \xi_0(\varepsilon, H)\big)$, where $\xi_0(\varepsilon, H) = \frac{f_0(H)\beta(\varepsilon)}{1-f_i(H)\beta(\varepsilon)}$. Figure 5 only shows the first order terms, if second and higher order corrections are also considered, the effective polarizability $\alpha_{\mathrm{eff,thin}}$ for thin film system is:

$$\alpha_{\text{eff,thin}}(\varepsilon_f, \varepsilon_s, H, d_0) = C\big(2 + \xi_0(\varepsilon_s, H) + \xi_0(\varepsilon_f, H + d_0) - \xi_0(\varepsilon_f, H + d_0)\big)$$
$$+2\xi_1(\varepsilon_f, H + d_0)\xi_0(\varepsilon_f, H + d_0)$$
$$-\big(\xi_1(\varepsilon_f, H)\xi_0(\varepsilon_f, H + d_0) + \xi_1(\varepsilon_f, H)\xi_0(\varepsilon_f, H)\big)$$
$$+\Big(\xi_1(\varepsilon_f, H)\xi_0(\varepsilon_s, H + d_0) + \xi_1(\varepsilon_s, H)\xi_0(\varepsilon_f, H)\Big)$$
$$-\big(\xi_1(\varepsilon_f, H + d_0)\xi_0(\varepsilon_s, H + d_0) + \xi_1(\varepsilon_s, H + d_0)\xi_0(\varepsilon_f, H + d_0)\big) \quad (62)$$

where $\xi_1(\varepsilon, H) = \frac{f_i(H)\beta(\varepsilon)}{1-f_i(H)\beta(\varepsilon)}$.

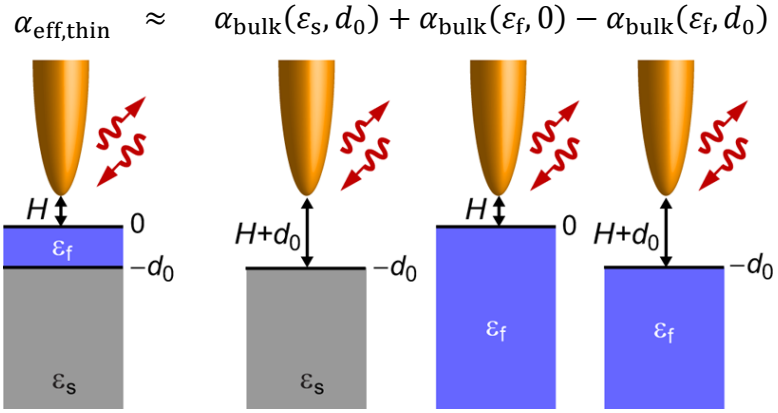

Figure 5. Schematic diagram of the representation of the effective polarizability of thin film system $\alpha_{\text{eff,thin}}$ by first order combination of α_{bulk} terms. (Image taken from reference [36].)

2.7 Background Signal Suppression

2.7.1 Background Scattering Contribution

As mentioned in Section 2.5, not only the gap between the tip and sample, but also the tip shaft and the sample is illuminated by the incoming laser beam. For s-SNOM, the background signal comes from the scattering by the tip shaft and the sample surface. Mathematically, this background scattering field $E_{s,bg} = \sigma_{bg}E_i$ should be added to Equation (48) so that the total backscattered field

$$E_s = \sigma E_i = (\sigma_{nf} + \sigma_{bg})E_i, \tag{63}$$

where $\sigma_{bg} = s_{bg}e^{i\phi_{bg}}$ is the background scattering coefficient and

$$\sigma = \sigma_{nf} + \sigma_{bg} = se^{i\phi} \tag{64}$$

is the total scattering coefficient.

2.7.2 Basic Principle

The basic principle of background suppression scheme [125, 126] is based on modulating the near-field scattering by operating the AFM in tapping mode, with tapping frequency Ω, and then demodulating the signal at higher order harmonics Ω, that is, at frequency $n\Omega$, where n is the demodulation order number. The point dipole (PD) model (Section 2.6.1) can give some insight about this idea. Equation (56) shows that the effective polarizability of the tip, α_{eff}, and thus the scattering coefficient σ_{nf} (Equation (58)), has strong non-linear effect when tip-sample distance H is small. In contrast, the variation of background scattering coefficient $\sigma_{bg} = s_{bg}e^{i\phi_{bg}}$ is comparatively small. As a result, for higher n, the demodulated signal is expected to be dominated by near-field contribution [96, 97, 127].

2.7.3 Modulation of Near-Field Scattering

Assuming the oscillation of the tip is sinusoidal with a dither frequency Ω so the height of the tip apex

$$H(t) = H_{\min} + \Delta H(1 + \cos(\Omega t)), \tag{65}$$

where $H_{\min}$ refers to the lowest position and ΔH is the oscillation amplitude, the total scattering coefficient σ is modulated and can be expressed by Fourier series:

$$\sigma\big(H(t)\big) = \sum_{n=0}^{\infty} \sigma_n \cos(n\Omega t) = \sum_{n=0}^{\infty} \big(\sigma_{\mathrm{nf},n} + \sigma_{\mathrm{bg},n}\big) \cos(n\Omega t)\,. \tag{66}$$

$\sigma_n = \sigma_{\mathrm{nf},n} + \sigma_{\mathrm{bg},n}$ is the n^{th} order Fourier coefficient of $\sigma\big(H(t)\big)$. It is expected that $\sigma_{\mathrm{nf},n} \gg \sigma_{\mathrm{bg},n}$ for higher demodulation order n, as explained in Section 2.7.2. It is found that higher tip dithering amplitude ΔH generates larger $\sigma_{\mathrm{nf},n}$ [96] but in return higher ΔH induces higher background contribution to the signal [96, 99]. As a result, there should be a compromise of choosing value of ΔH, and practically, ΔH is chosen to be lower than the tip diameter.

2.7.4 Signal Demodulation

Since total scattering field $E_{\mathrm{s}} \propto \sigma$ (Equation (63)), E_{s} can also be expanded by Fourier series: $E_{\mathrm{s}}\big(H(t)\big) = \sum_{n=0}^{\infty} E_{\mathrm{s},n} \cos(n\Omega t)$. Demodulating E_{s} at higher harmonics $n\Omega$ yields $E_{\mathrm{s},n}$, which is background-free, because $E_{\mathrm{s},n} \propto \sigma_n \approx \sigma_{\mathrm{nf},n}$. However, detected signal U is not E_{s}, but rather the intensity I:

$$U \propto I \propto E_{\mathrm{s}} E_{\mathrm{s}}^{*} \propto \sigma\sigma^{*} = \big(\sigma_{\mathrm{nf}} + \sigma_{\mathrm{bg}}\big)\big(\sigma_{\mathrm{nf}} + \sigma_{\mathrm{bg}}\big)^{*}. \tag{67}$$

The demodulated signal U_n can be expressed by the complex Fourier transform of $\sigma\big(H(t)\big)$ with respect to time t:

$$U_n(\beta) \propto \frac{1}{T}\int_0^T \sigma\big(\beta, H(t)\big)\, e^{in\Omega t} dt, \tag{68}$$

where $T = 2\pi/\Omega$ is the dithering period of the tip. Substituting Equation (66) into expression (67) and the expression of the nth order demodulated signal U_n for high n is (Appendix A)

$$U_n \propto s_{\mathrm{nf},n} {s_{\mathrm{bg},0}}^* \cos\big(\phi_{\mathrm{nf},n} - \phi_{\mathrm{bg},0}\big). \tag{69}$$

Although the demodulated signal U_n successfully has an amplitude proportional to $s_{\mathrm{nf},n}$, which is the amplitude of $\sigma_{\mathrm{nf},n}$ (Equation (49)), U_n is influenced by the background phase $\phi_{\mathrm{bg},0}$ which is uncontrollable and difficult to be predicted. Therefore, this direct detection scheme should be replaced by interferometric detection which is able to produce background-free signal and simultaneously detect the target signals: $s_{\mathrm{nf},n}$ and $\phi_{\mathrm{nf},n}$.

2.7.5 Pseudo-Heterodyne Interferometric Detection

Interferometric detection has been employed in s-SNOM for a long time. Homodyne [128, 129] and heterodyne [97, 127, 129, 130] schemes have been demonstrated as effective methods to suppress the background signal. A commercial s-SNOM (Neaspec GmbH) employs pseudo-heterodyne [131] (PsHet) interferometric detection, which exhibits much better background suppression power.

Figure 6 shows the schematic diagram of pseudo-heterodyne detection. The laser source emits laser beam towards a beam-splitter (BS), which splits the light into

two parts. One part is focused onto the tip by a parabolic mirror for near-field scattering process. The backscattered light is collected by the same parabolic mirror and propagates back to the BS and finally is focused to the detector. The other part propagates to the reference mirror and is reflected. This reflected light, called reference beam, will finally reaches the detector and interferes with the first part.

In pseudo-heterodyne scheme, the reference mirror is set to oscillate with frequency M [131], which can modulate the phase of the reference beam so that the field E_{ref} can be expressed by Fourier series. Equation (67) should be modified to $U \propto (\sigma_{\mathrm{nf}} + \sigma_{\mathrm{bg}} + \sigma_{\mathrm{ref}})(\sigma_{\mathrm{nf}} + \sigma_{\mathrm{bg}} + \sigma_{\mathrm{ref}})^*$, where $\sigma_{\mathrm{ref}} = E_{\mathrm{ref}}/E_{\mathrm{i}}$. The n^{th} order demodulated near-field coefficient for higher n can be obtained by [131] (Appendix B)

$$\sigma_{\mathrm{nf},n} \propto U_{n,2} + iU_{n,1}, \tag{70}$$

where $U_{n,1}$ and $U_{n,2}$ are the signal demodulated at frequency $n\Omega + \mathrm{M}$ and $n\Omega + 2\mathrm{M}$ respectively. Therefore, s-SNOM can obtain the near-field amplitude and phase simultaneously via

$$s_{\mathrm{nf},n} \propto \sqrt{{U_{n,1}}^2 + {U_{n,2}}^2} \quad \text{and} \quad \phi_{\mathrm{nf},n} \propto \tan^{-1}\left(\frac{U_{n,1}}{U_{n,2}}\right). \tag{71}$$

Compared with non- interferometric detection as mention in Section 2.7.4, the signal obtained by PsHet interferometric detection contains no uncontrollable parameter. Nonetheless, the detected signal is no longer the near-field scattering coefficient σ_{nf} (Equation (49)) but the Fourier coefficient $\sigma_{\mathrm{nf},n}$ (Equation (66)).

(a)

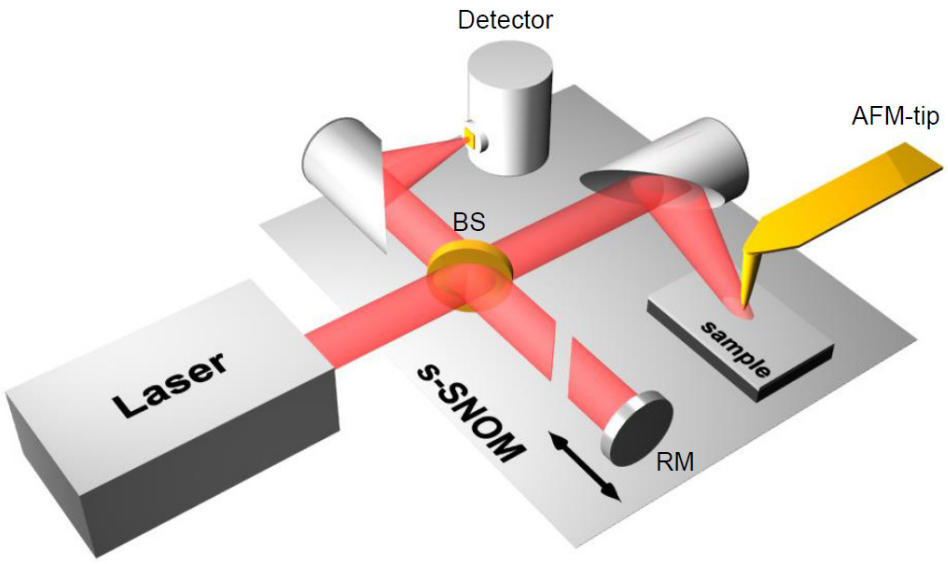

Figure 6. Schematic diagram of the pseudo-heterodyne interferometric detection. (Image taken from reference [132].)

2.7.6 Near-Field Contrast

By employing pseudo-heterodyne interferometric detection, the detected s-SNOM signal is proportional to $\sigma_{\mathrm{nf},n}$. The value of $\sigma_{\mathrm{nf},n}$ can be predicted by applying suitable model, such as the FD model (Section 2.6.2). However, the proportionality between signal and $\sigma_{\mathrm{nf},n}$ is typically unpredictable because it relates to the response function of the setup. To obtain a predictable signal, the detector signal is normalized to a reference signal from a sample having well-known optical properties, such as silicon and gold. This yields a signal called near-field contrast:

$$\eta_{\mathrm{n}} = \frac{\sigma_{\mathrm{n}}}{\sigma_{\mathrm{n,ref}}} = \frac{s_{\mathrm{n}}}{s_{\mathrm{n,ref}}} e^{i\phi_{\mathrm{n}} - \phi_{\mathrm{n,ref}}}. \tag{72}$$

3 Nanoscale Fourier Transform Infrared Spectroscopy (Nano-FTIR)

Scattering-type SNOM has been introduced in Section 2.5. It offers the nano-scale resolving power to measure the near-field amplitude $|\eta_{\mathrm{n}}|$ and phase $\arg(\eta_n)$ simultaneously. Nanoscale Fourier Transform Infrared Spectroscopy (Nano-FTIR) [34, 117] is a technique combining the nano-scale resolving power of s-SNOM and the spectrum measuring function of FTIR. Therefore, Nano-FTIR provides the power to obtain the near-field amplitude spectrum $|\eta_{\mathrm{n}}(\omega)| = \frac{s_{\mathrm{n}}(\omega)}{s_{\mathrm{n,ref}}(\omega)}$ and the near-field phase spectrum $\arg(\eta_n(\omega)) = \phi_{\mathrm{n}}(\omega) - \phi_{\mathrm{n,ref}}(\omega)$ simultaneously in a single measuring process and in nano-scale resolution.

3.1 Working Principle

The schematic diagram of a nano-FTIR spectrometer is shown in Figure 7. Different from s-SNOM in which monochromatic source is used, nano-FTIR employs broadband laser source generated by different-frequency generator (DFG) [133], like the conventional FTIR. A beamsplitter (BS) splits the broadband light into two parts. One part propagates to the linearly moving reference mirror and is reflected as a reference beam and finally reaches the detector. Another part propagates to a parabolic mirror and is focused onto the gap between the AFM tip and the sample surface, in where backscattered light is generated. The parabolic mirror also collects that backscattered light and focuses it onto the beamsplitter and finally reaches the detector

and interferes with the reference beam. The interference signal is then demodulated at high order number n (Section 3.2) to suppress the background noise, yielding a complex interferogram $U_n(d)$, which can finally be used to calculate the complex near-field spectrum $U_n(\omega)$, from which the near-field amplitude spectrum $|U_{\mathrm{n}}(\omega)|$ and phase spectrum $\arg(U_n(\omega))$ can be obtained.

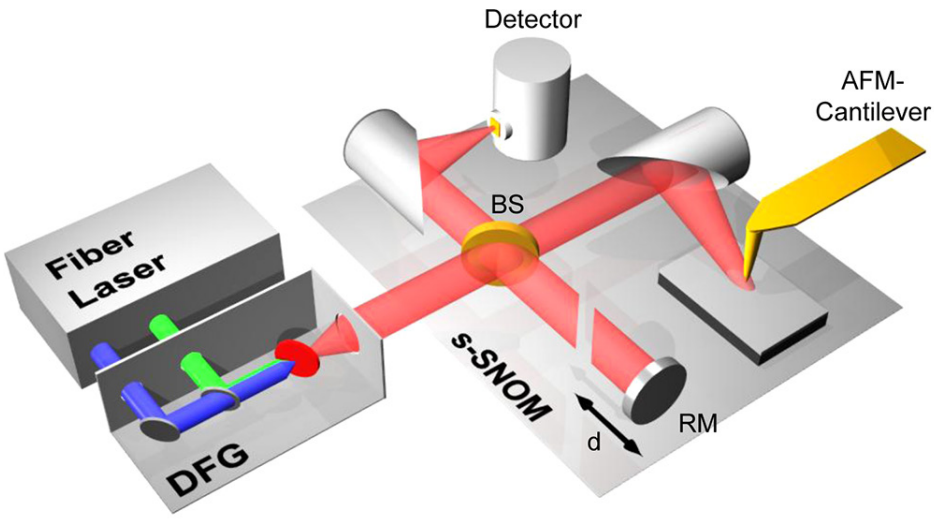

Figure 7. Schematic diagram of experimental setup of nano-FTIR spectrometer. (Image is taken from ref [34].)

3.2 Background Scattering Suppression

Like s-SNOM, the background scattering from AFM tip shaft and neighbour sample region should be removed and therefore signal demodulation technique is employed to achieve this, like the one in s-SNOM (Section 2.7). The nth order demodulated signal, that is, the interferogram, is given by:

$$U_n(d) \propto s_{\mathrm{nf},n}\left[s_{\mathrm{bg},0}\cos\left(\varphi_{\mathrm{nf},n}-\varphi_{\mathrm{b},0}\right)+s_{\mathrm{ref}}\cos\left(\varphi_{\mathrm{nf},n}-\varphi_{\mathrm{ref}}\right)\right], \qquad (73)$$

which is similar to Equation (69) but has an additional term relating to reference beam. Equation (73) is derived in Appendix C. It can be seen than the detected signal still contains uncontrollable background related parameter $\varphi_{\mathrm{b},0}$. Nonetheless, if we perform Fourier transform on Equation (73), the first term vanishes because it is independent of d. Therefore, the complex near-field spectrum $U_n(\omega)$ is given by [132]:

$$U_n(\omega) = \int_0^\infty s_{\mathrm{nf},n} s_{\mathrm{ref}} \cos\left(\varphi_{\mathrm{nf},n} - 2\pi\omega d\right) e^{i2\pi\omega d} \mathrm{d}d \,. \tag{74}$$

This yields the near-field spectrum $U_n(\omega) \propto s_{\mathrm{nf},n} e^{i\varphi_{\mathrm{nf},n}} = \sigma_{\mathrm{nf},n}$.

4 Near-Field Optical Microscopy Study of $PtSe_2$ Flakes

s-SNOM and Nano-FTIR spectroscopy were employed to perform near-field optical study of $PtSe_2$ flakes. Waveguide modes in $PtSe_2$ were imaged directly in real-space in nano-scale resolution by s-SNOM and fringe patterns parallel to the edge were observed. By analysing the properties of these fringes, the dispersion relations of these modes were successfully extracted, confirmed by the theory. Nano-FTIR was used to measure the near-field spectra of $PtSe_2$ and the results agreed, at least qualitatively, with the FD model.

4.1 Experimental Set-up

The elastic s-SNOM used for nano-optical imaging is the commercial NeaSNOM (www.neaspec.com/), which is based on an AFM operating at tapping mode. The AFM tip oscillates with frequency equal to its resonance frequency $\Omega \approx 270$ kHz and with dithering amplitude $\Delta H \approx 70$ nm. The AFM tip is illuminated by a monochromatic NIR or MIR laser beam and generates modulated scattering light. The operating wavelength of NIR laser (www.toptica.com/) is 1550 nm while the wavelength of the MIR quantum cascade laser (QCL) (www.daylightsolutions.com) is turned from 3.97 to 7.24 μm (1380 to 2520 cm^{-1}). Background scattering signal was eliminated by the use of pseudo-heterodyne interferometric detection method and then demodulating the detected signal by lock-in amplifier at the 3rd order harmonic of the dithering frequency Ω, thereby generating near-field amplitude signal $s_{\mathrm{nf},n}$ and phase signal $\phi_{\mathrm{nf},n}$ simultaneously. The signal is detected by a mercury cadmium telluride (MCT, HgCdTe) detector which is cooled by liquid nitrogen. The focusing of laser

beam to the AFM tip and the collection of the backscattered light is done by one parabolic mirror with small collection angle. The s-SNOM performs all the nano-imaging at ambient conditions.

Nano-FTIR spectroscopy was provided by the same commercial NeaSNOM. The tapping AFM tip was illuminated by a broadband MIR laser source with frequency range 700 – 2500 cm^{-1}, generated by different-frequency generator (DFG). An asymmetric Michelson interferometer with 1.5-mm travel range reference mirror enables collection of demodulated near-field amplitude $s_{\mathrm{nf},n}(\omega)$ and phase $\phi_{\mathrm{nf},n}(\omega)$ spectra.

4.2 $PtSe_2$ Sample

4.2.1 Background

Layered transition metal dichalcogenides (TMDCs) with the formula MX_2 (X=S, Se or Te) have attracted scientists' attention for future nano-photonics and nano-optoelectronics [134]. Scientific research has been focused much more on the TMDCs with group 6 transition metals (M=Mo or W) than the group 10 TMDCs (M=Pt, Pd or Ni) [1, 2, 135]. The group 10 TMDCs were found to have electronic properties distinct from group 6 TMDCs due to the greater degree of hybridization between the valance d-orbitals of the group 10 metals and the valance p-orbitals of the chalcogen atoms, which is resulting from the close binding energy values between these d- and p-

orbitals [2]. Due to its distinct electronic properties and air stability [5], $PtSe_2$, one of the candidates of group 10 TMDCs, has been studied for optoelectronic applications such as field effect transistors (FETs) [5, 16], gas sensing [17], photocatalysis [8], photodetection [18], spintronics [19], valleytronics [8] and also MIR applications [10].

$PtSe_2$ has the CdI_2-type crystal structure. The Bravais lattice of this structure is 1T-type hexagonal. The 3D structure is obtained by stacking $PtSe_2$ layers, which are made up of edge-sharing $PtSe_6$ octahedra, as shown in Figures 8 (a) and (b). In each $PtSe_2$ layer, the Pt 2D-layer is sandwiched between two Se layers. The $PtSe_2$ crystal structure belongs to $P\bar{3}ml$ space group of the centrosymmetric trigonal system and belongs to D_{3d}^3 point group. The primitive lattice vectors can be chosen to be $\boldsymbol{a_1} = a\hat{\boldsymbol{x}}$, $\boldsymbol{a_2} = 0.5a\left(-\hat{\boldsymbol{x}} + \sqrt{3}\hat{\boldsymbol{y}}\right)$ and $\boldsymbol{a_3} = c\hat{\boldsymbol{z}}$ and the atoms are positioned at Pt(0, 0, 0), X(1/3, 2/3, u), and X(2/3, 1/3, -u) in the primitive cell. The in-plane lattice constants a and b have be found to be about 3.8 Å for bulk $PtSe_2$ [136] and 3.785 Å by calculation [137]. For monolayer, the lattice constants a and b decrease to be about 3.7 Å [7, 8]. The out-of-plane lattice constant is predicted to be $c = 5.107$ Å [12], which is also consistent with the experimental result, $c = 5.081$ Å [136, 138]. The u value, that is, the z-coordinate of the Se atom position in the primitive cell, is 0.255 [136], which is near to the ideal value, 1/4. The c/a ratio is about 1.363, which is smaller than the value (1.67) predicted in an ideal hexagonal close packing of Se atoms. This effect may be due to the distinct electronic properties of group 10 TMDCs as mentioned above.

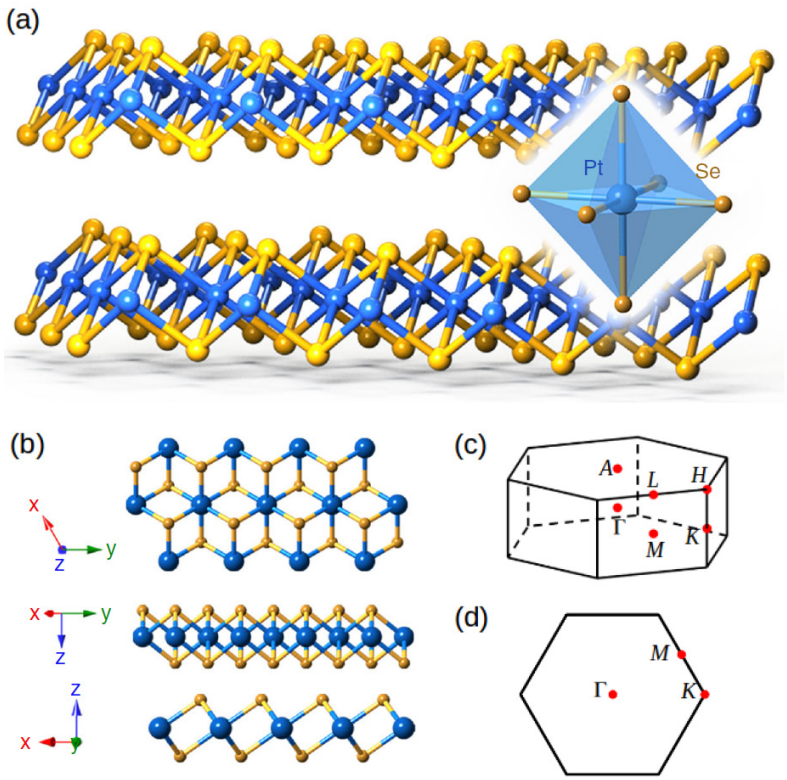

Figure 8. (a), (b) Crystal structure of $PtSe_2$. (c), (d) Brillouin zone of (c) bulk and (d) thin $PtSe_2$ in which high symmetry points are indicated by red dots. (Images taken from ref. [10])

Because of the great degree of hybridization between the valance d-orbitals of the Pt and the valance p-orbitals of the chalcogen atoms, $PtSe_2$ has distinct electronic properties. The calculated band structures [8] for monolayer, bilayer, trilayer and bulk $PtSe_2$ are shown in Figure 9. The bandgap of the semiconducting monolayer $PtSe_2$ is predicted to be 1.2eV [2], which is confirmed by experiment [8]. The interesting spin properties of the monolayer $PtSe_2$ [19] favour the application on spintronics. The bilayer $PtSe_2$ remains to be semiconducting but the bandgap decreases to 0.21eV, calculated by first-principles calculations [8]. This bandgap value and high environmental stability favour the photonic and optoelectronic applications in MIR frequency range [10]. The semiconductor-to-semimetal transition occurs when the

layer number is increased to 3. This transition is predicted by calculations [8] and confirmed by experimental results [10]. The transition can also be induced by strain [6, 13-15]. Although the monolayer and bilayer $PtSe_2$ have electron mobilities about 1.7 [10] and 8.6 [5] $cm^2\ V^{-1}\ s^{-1}$ respectively, the few-layer $PtSe_2$ possesses high electron mobility (≈210 $cm^2\ V^{-1}\ s^{-1}$) and theoretically the mobility of $PtSe_2$ can be as high as 16250 $cm^2\ V^{-1}\ s^{-1}$ [5]. The bulk $PtSe_2$ is predicted to be semimetallic long ago [1, 2] and recently it was shown that it is a type-II Dirac semimetal [11, 12]. This kind of topological semimetals provide platform for studying novel physical properties [139, 140], topological phase transitions and potential device applications [141, 142].

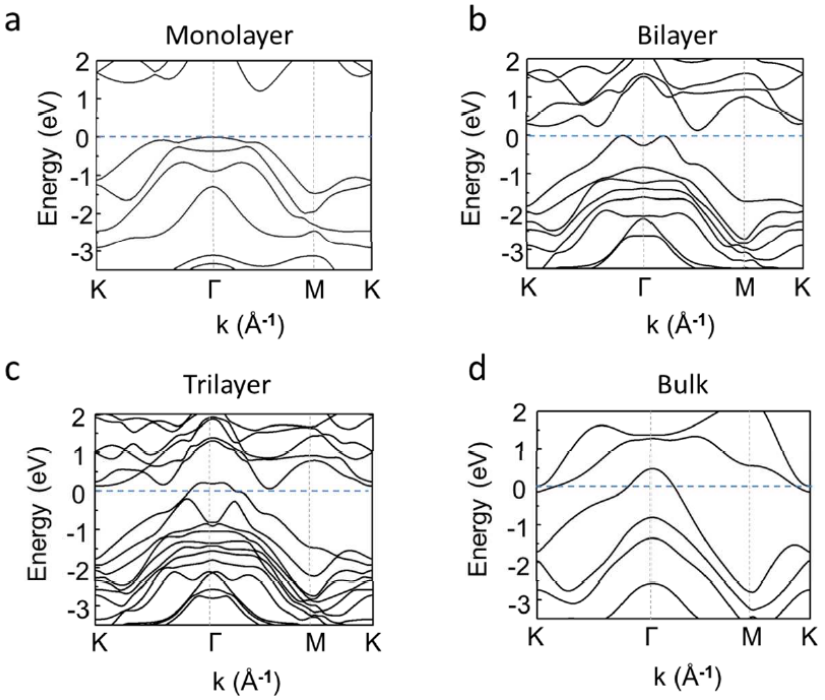

Figure 9. Band structures of (a) monolayer, (b) bilayer, (c) trilayer and (d) bulk $PtSe_2$, calculated by Y. Wang et al. [8].

4.2.2 Sample Fabrication

The substrates used is Si wafers with 300-nm-thick SiO_2 on the top. $PtSe_2$ flakes were fabricated by mechanically exfoliating a high quality bulk $PtSe_2$ crystal (www.2dsemiconductors.com/) onto the SiO_2/Si substrates. For the s-SNOM study, the $PtSe_2$ flakes with thickness 579 nm and 696 nm were used. The AFM topographies of these samples are shown in Figure 10.

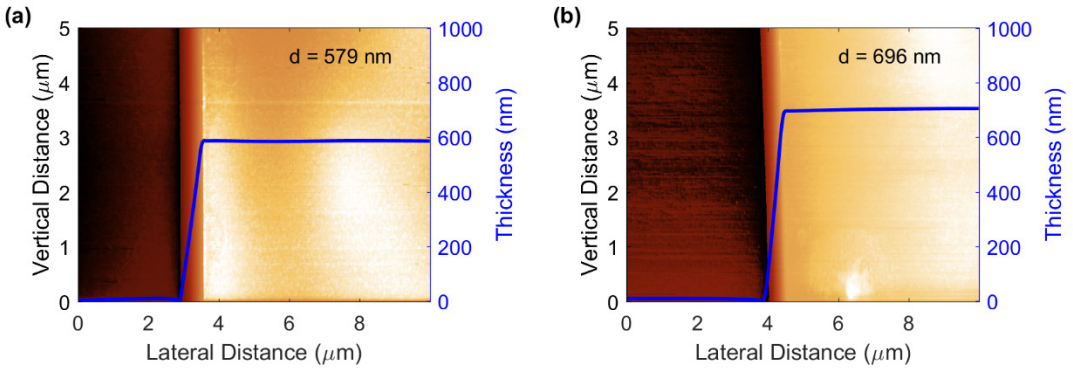

Figure 10. The AFM topographies and line profiles of the $PtSe_2$ samples with thicknesses (a) 696 nm, (b) 579 nm.

4.3 Optical Constant of $PtSe_2$

4.3.1 Far-field FTIR Study

As mentioned in Section 2.2.2, the complex dielectric constant $\varepsilon(\mathbf{k}, \omega)$ (Equation (29)) determines the optical property of a material. In order to calculate the dispersion relation of the waveguide modes in $PtSe_2$ and the near-field amplitude spectrum of $PtSe_2$, it is needed to determine the dielectric constant. Therefore, far-field

FTIR spectroscopy technique was employed to determine this optical constant of $PtSe_2$. This technique is limited to explore only the frequency dependent constant $\varepsilon(\omega)$. The **k**-dependent comes from the non-local effect, which can be neglected in most cases, as mentioned in the Section 2.2.2.1. Therefore, the correctly determined $\varepsilon(\omega)$ is sufficient to predict optical phenomena of corresponding materials. IR ellipsometry, a widely used spectroscopy for determining material's dielectric constant, has not been used because it does not possess high enough resolving power.

BRUKER FTIR spectrometer with reflection mode was used to extract the reflectivity $R(\omega)$ of $PtSe_2$ flakes on Au substrates in frequency range $500 - 6000\ \mathrm{cm}^{-1}$. The incident beam is randomly polarized and has incident $\theta_{\mathrm{inc}} \sim 15^{\mathrm{o}}$. Gold substrates was chosen because of its high reflectivity, which is near to 1 within the MIR frequency range. In addition, frequency-independent reflectivity makes it a suitable reference material.

The measured spectra $R(\omega)$ for sample with $PtSe_2$ thicknesses 199 nm, 1013 nm, 1708 nm and 2810 nm are shown by the black lines in Figure 11. Although bulk $PtSe_2$ has been predicted to be semi-metallic [1, 2, 7], the reflectivity of 1013, 1708 and 2810 nm thick $PtSe_2$ samples show clear Fabry–Pérot (FP) cavity interference effect, which is a phenomenon due to the dielectric properties of the materials. This dielectric nature in the $PtSe_2$ flakes could facilitate the fabrication of optical waveguides.

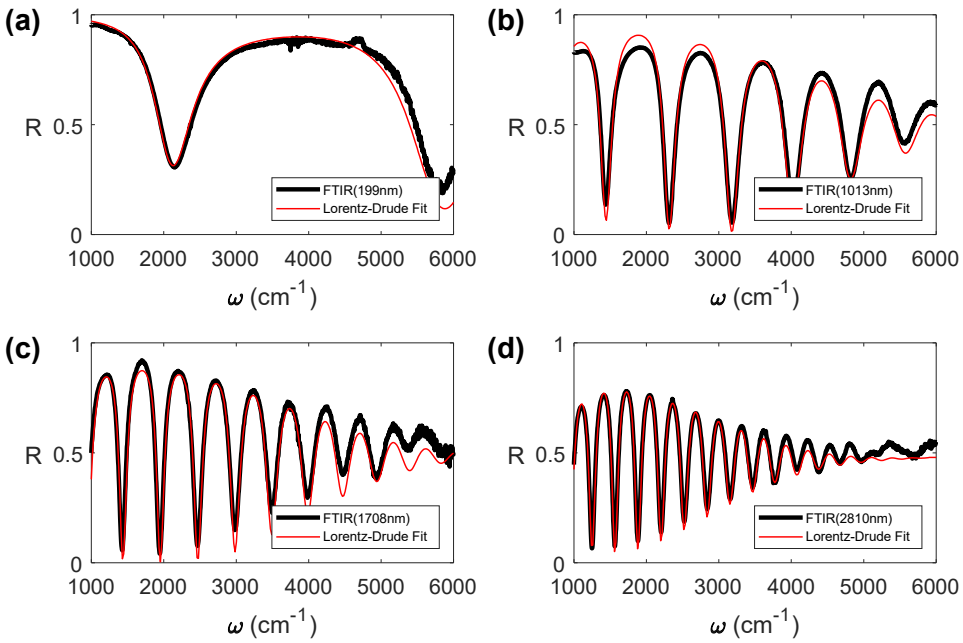

Figure 11. Far-field FTIR and fitted reflectivity spectra of $PtSe_2$ flakes on Au substrates. Samples with (a) 199 nm, (b) 1013 nm, (c) 1708 nm and (d) 2810 nm thick $PtSe_2$ layer were tested. Red lines refer to fitted reflectivity by single-Lorentz-Drude model while black lines refer to the measured ones.

4.3.2 Lorentz-Drude Modelling

In this work, the dielectric constant $\varepsilon(\omega)$ of the $PtSe_2$ was determined from measuring the reflectivity spectra $R(\omega)$. The principle is that one can calculate $R(\omega)$ if the dielectric constants of all three layers in the Air/$PtSe_2$/Au system are known. Here. the dielectric constant of the first layer (air) is $\varepsilon_1 = 1$. Gold, the third layer, is a metal and there is no interband transition in MIR range. As a result, its dielectric constant can be represented by a simple Drude form (Equation (23)) $\varepsilon_3(\omega) = 1 - {\omega_p}^2/(\omega^2 + i\gamma\omega)$, where the plasma frequency $\omega_p = 72800\ \mathrm{cm}^{-1}$ and collision frequency $\gamma = 215\ \mathrm{cm}^{-1}$ [143]. Therefore, only the second layer ($PtSe_2$) has unknown

$\varepsilon(\omega)$. If one can find a value of $\varepsilon_2(\omega)$ ($PtSe_2$) from which the calculated reflectivity $R(\omega)$ fitting well with the measured one, this fitted $\varepsilon(\omega)$ can be regard as reliable.

The steps for calculating $R(\omega)$ are presented as follows. The effective reflectivity $R(\omega)$ for unpolarized light and for small incident angle can be calculated from the expression [144]:

$$R = \frac{r_s^2 + r_p^2}{2}, \tag{75}$$

where r_p and r_s are the Fresnel's reflection coefficients for p- and s- polarized light of the Air/$PtSe_2$/Au-layer system. These coefficients of such a three-layer system can be calculated by Equation (40), accompanied with Equations (34) and (36), and also the relation $k_{\parallel} = k_0 \sin\theta_{inc}$. It is assumed that all the layers are non-magnetic materials so that $\mu_i = 1$.

In order to fit the reflectivity $R(\omega)$, Lorentz-Drude (LD) model (Equation 30) with signal Lorentz oscillator term is used to express the dielectric constant of $PtSe_2$ $\varepsilon_2(\omega)$:

$$\varepsilon_2(\omega) = \varepsilon_\infty - \frac{{\omega_p}^2}{\omega^2 + i\gamma\omega} + \frac{f^2}{\omega_0 - \omega^2 - i\Gamma\omega}, \tag{76}$$

where f, ω_0 and Γ are the strength, eigenfrequency and damping rate of the oscillator. ε_∞ is called high-frequency permittivity, which corresponds to the high polarized environment surrounding the carriers in inner bands. The second is the Drude term attributing to the free charge carriers in the semi-metallic bulk $PtSe_2$ [1, 2, 7, 11, 12]. A Lorentz-oscillator term, that is the third term, is add to the Drude term in order to account for the contribution from the interband transition of the bound charge carriers.

The high-frequency permittivity ε_∞ is chosen to be $\varepsilon_\infty = 15$ [138] while other parameters chosen to fit $R(\omega)$ are listed in Table 1. The reflectivity spectra $R(\omega)$ calculated from the fitted dielectric constant $\varepsilon_2(\omega)$ of $PtSe_2$ are plotted as red lines in Figure 11. The corresponding fitted dielectric constants $\varepsilon_2(\omega)$ for $PtSe_2$ layers are plotted in Figure 12(a). One can see from Figure 11 that the calculated spectra match with the experimental FTIR spectra, especially in the frequency range 1000 – 3000 cm^{-1}. That means the obtained dielectric constants for the $PtSe_2$ samples (Table 1 and Figure 12(a)) are valid for theoretical study on the optical properties of $PtSe_2$ in the frequency range 1000 – 3000 cm^{-1}. The fitted dielectric constants $\varepsilon_2(\omega)$ do not vary at high degree for different thicknesses, except for d =199 nm, which has higher damping terms γ and Γ. This may be due to the thickness-dependent properties of $PtSe_2$ [7, 137].

	$\omega_p/\mathrm{cm}^{-1}$(eV)	γ/cm^{-1}	f/cm^{-1}	$\omega_0/\mathrm{cm}^{-1}$(eV)	Γ/cm^{-1}
d=199nm	2420.4 (0.300)	1076.8	42973	11244 (1.39)	4460.6
d=1013nm	2501 (0.310)	410.35	39251	10940 (1.36)	2820.9
d=1708nm	2564.7 (0.318)	321.44	40738	11197 (1.39)	2564.7
d=2810.3nm	2494.9 (0.309)	376.8	40915	11355 (1.41)	3385.8

Table 1. Parameters of single-Lorentz-Drude model for fitting the FTIR spectra for $PtSe_2$/Au system with different $PtSe_2$ thicknesses d.

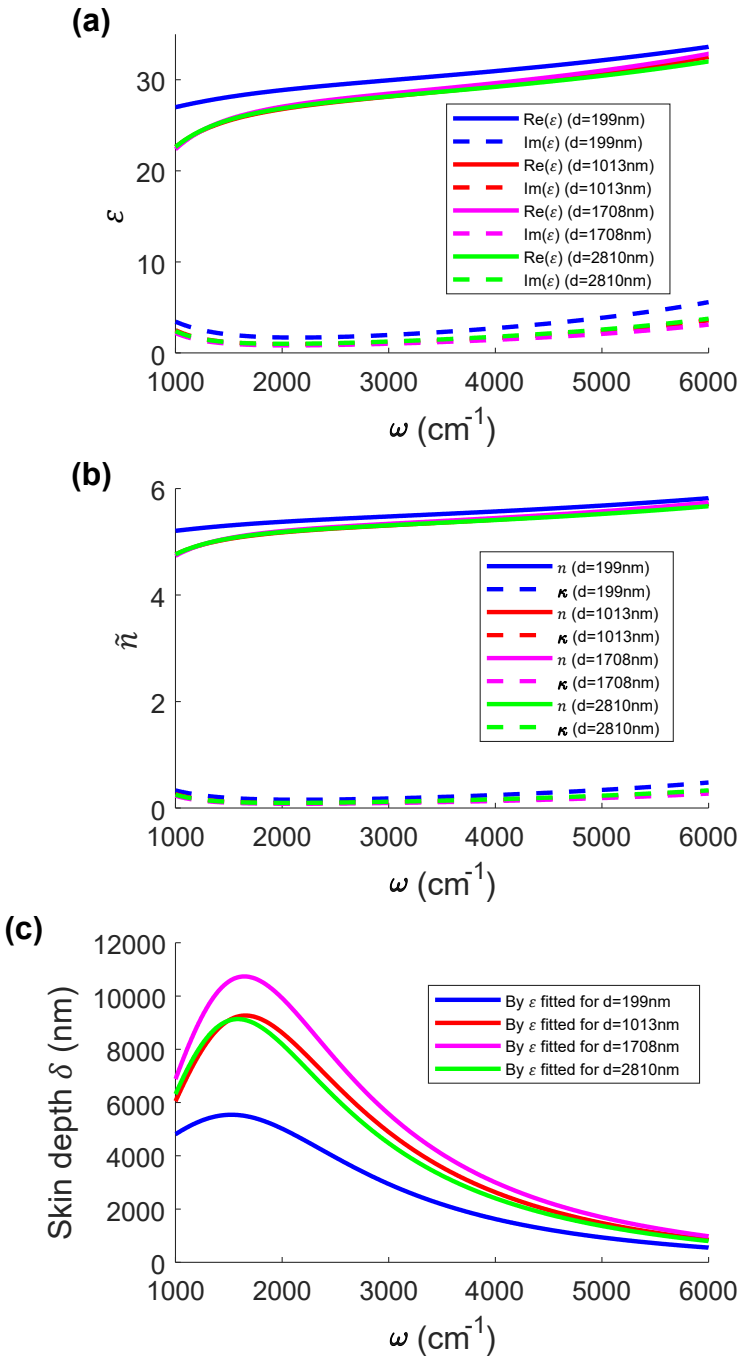

Figure 12. (a) Complex dielectric constants $\varepsilon(\omega)$ of $PtSe_2$ with different thicknesses, obtained by assuming Lorentz-Drude formalism and fitting the measured FTIR reflectivity spectra $R(\omega)$. (b) Complex refractive indices $\tilde{n} = n + i\kappa$ of $PtSe_2$, calculated by using the obtained $\varepsilon(\omega)$ in (a). The real part n is the normal refractive index while the imaginary part κ is the extinction coefficient. **(c)** Skin depths δ of $PtSe_2$ obtained by the fitted dielectric constants for sample with different thicknesses.

4.3.3 Skin Depth

Referring back to Figure 11, the reflectivity spectra show that, except for the d = 199 nm sample, the Fabry–Pérot (FP) oscillating signal becomes weaker and weaker when frequency increases. This weakening effect is especially strong for the sample with thickness d = 2810 nm in high frequency region, in where the oscillation almost disappears. By explaining this, the skin depth of $PtSe_2$ should be calculated, which is related to the imaginary part (κ) of the complex refractive index $\tilde{n} = n + i\kappa$, by the expression [64]

$$\delta = \frac{2}{\alpha} = \frac{c}{\kappa\omega(\text{rad s}^{-1})}, \tag{77}$$

where α is the absorption coefficient, c is the speed of light and the imaginary part κ is called the extinction coefficient. The complex refractive index is related to the complex dielectric constant $\varepsilon = \varepsilon_1 + i\varepsilon_2$ by relations $n = \frac{1}{\sqrt{2}}\sqrt{\varepsilon_1 + \sqrt{\varepsilon_1^2 + \varepsilon_2^2}}$ and $\kappa = \frac{1}{\sqrt{2}}\sqrt{-\varepsilon_1 + \sqrt{\varepsilon_1^2 + \varepsilon_2^2}}$. The complex refractive indices $\tilde{n}(\omega)$ for samples with different thicknesses are calculated and plot in Figure 12(b), and in turn the calculated skin depths $\delta(\omega)$ are plot in Figure 12(c). The $\delta(\omega)$ of $PtSe_2$ is found to be as high as about 8000 μm at $\omega \sim 1700\ \text{cm}^{-1}$. This high penetration depth might be due to the low value of the extinction coefficient $\kappa \sim 0.1$ at this frequency, and therefore low absorption of $PtSe_2$. Because the skin depth δ is inversely proportional to frequency ω, the skin depth decreases greatly with higher frequency and becomes about 1000 μm when frequency reaches $6000\ \text{cm}^{-1}$. This variation of δ agrees with the weakening oscillating signals in FTIR spectra $R(\omega)$ shown in Figure 11. First, for the

199-nm-thick sample (Figure 11(a)), the skin depth in the whole frequency range is much higher than the thickness, and therefore the weakening effect does not appear. For the 1013-nm-thick sample (Figure 11(a)), there is weakening effect and the effect becomes severer for thicker samples. For the 2810-thick-sample, the oscillating signal is strongest at $\omega \sim 1700\ \mathrm{cm}^{-1}$, in where the skin depth becomes highest with value about 8000 μm, which is much larger than the thickness and therefore the oscillating signal at around $\omega = 1700\ \mathrm{cm}^{-1}$ is still pronounced. However, at frequency near $6000\ \mathrm{cm}^{-1}$, the skin depth decreases to value only about 1000 μm, which means the light cannot penetrate through the $PtSe_2$ and therefore the oscillating signal disappears.

4.3.4 Plasma Frequencies and Charge Carrier Concentration

The plasma frequencies ω_p fitted for different thicknesses are all near $2500\ \mathrm{cm}^{-1}$ (0.3 eV) (Table 1). This is agreed with previous experimental results by G. Kliche [138]. From his IR study, the reflectance of $PtSe_2$ decreases from maximum to minimum in the frequency range about $400 - 1600\ \mathrm{cm}^{-1}$. From Equations (23), (34) and (36), the reflectance of a slightly damped free electron system for normal incident light can be expressed by $R(\omega) = \left|\frac{\sqrt{\varepsilon_{r,\mathrm{free}}}-1}{\sqrt{\varepsilon_{r,\mathrm{free}}}+1}\right|^2 = \left|\left[\sqrt{\varepsilon_\infty}\sqrt{1-\left(\frac{\omega_p/\sqrt{\varepsilon_\infty}}{\omega}\right)^2}-1\right] / \left[\sqrt{\varepsilon_\infty}\sqrt{1-\left(\frac{\omega_p/\sqrt{\varepsilon_\infty}}{\omega}\right)^2}+1\right]\right|^2$. For $\omega \le \frac{\omega_p}{\sqrt{\varepsilon_\infty}}$, $R(\omega) = 1$, while for $\omega > \frac{\omega_p}{\sqrt{\varepsilon_\infty}}$, the reflectance decreases greatly and becomes 0 for high frequency. Alternatively, for $\omega \le \frac{\omega_p}{\sqrt{\varepsilon_\infty}}$, the dielectric constant $\varepsilon_{r,\mathrm{free}} = \varepsilon_\infty\left[1-\left(\frac{\omega_p/\sqrt{\varepsilon_\infty}}{\omega}\right)^2\right]$ for the free electron system

becomes a negative real number, and thus the "complex" reflective index $\tilde{n} = \sqrt{\varepsilon_{r,\text{free}}} = n + ik$ is purely imaginary, which represents that the light cannot penetrate through the system and therefore $R(\omega) = 1$. On the other hand, for $\omega > \frac{\omega_p}{\sqrt{\varepsilon_\infty}}$, $\varepsilon_{r,\text{free}}$ becomes a positive real number and therefore $\tilde{n}$ is purely real and has no the absorption related imaginary part, which means that the system is transparent to light in this frequency region. In this work, the obtained $\frac{\omega_p}{\sqrt{\varepsilon_\infty}}$ value is about $\frac{2500}{\sqrt{15}} \approx 645\ \text{cm}^{-1}$, which is within the range $400 - 1600\ \text{cm}^{-1}$ from Kliche, thereby revealing the reliability of the fitted plasma frequencies ω_p. From the fitted ω_p (about 2500 cm^{-1}) and by using $\omega_p = \sqrt{\frac{Ne^2}{\varepsilon_0 m^*}}$ (Equation (24)) and choosing $m^* = 0.35m_e$ (where m_e denotes the mass of an free electron) [145], the free charge carrier concentration of $PtSe_2$ is found to be $N = 2.44 \times 10^{19}\ \text{cm}^{-3}$, which is within the a typical range for a semimetal: $1 \times 10^{17} - 1 \times 10^{22}\ \text{cm}^{-3}$.

4.3.5 Interband Transition by Bound Charges

For the bound electron term, that is the Lorentz oscillator term, the resonant frequencies ω_0 for all the thicknesses are about 1.4 eV. This effect might be due the interband transition by the core electrons in $PtSe_2$, by referring the band structure of bulk $PtSe_2$ (Figure 9(d)). The Lorentz-Drude fitted dielectric constants $\varepsilon_2(\omega)$ for $PtSe_2$ layers in extend frequency range including visible region are plotted as colour lines in Figure 13. One can see that the real parts $\text{Re}(\varepsilon_2(\omega))$ exhibit dispersion-like shape while the imaginary parts $\text{Im}(\varepsilon_2(\omega))$ have absorption-like bell-shape. It is typical

effect by the Lorentz oscillator term which is added to account for the interband transition effect. One can also see that both the real parts and imaginary parts of $\varepsilon(\omega)$ vary with the $PtSe_2$ thickness at high degree when ω is near the eigenfrequencies ω_0, which are about 11000 cm^{-1} (1.4 eV) for all 4 thicknesses. Nevertheless, for the near-field optical microscopy study of the $PtSe_2$ which will be discussed below, the frequency of interest is 1380 to 2520 cm^{-1}, within this range the $\varepsilon(\omega)$ varies little with the thickness.

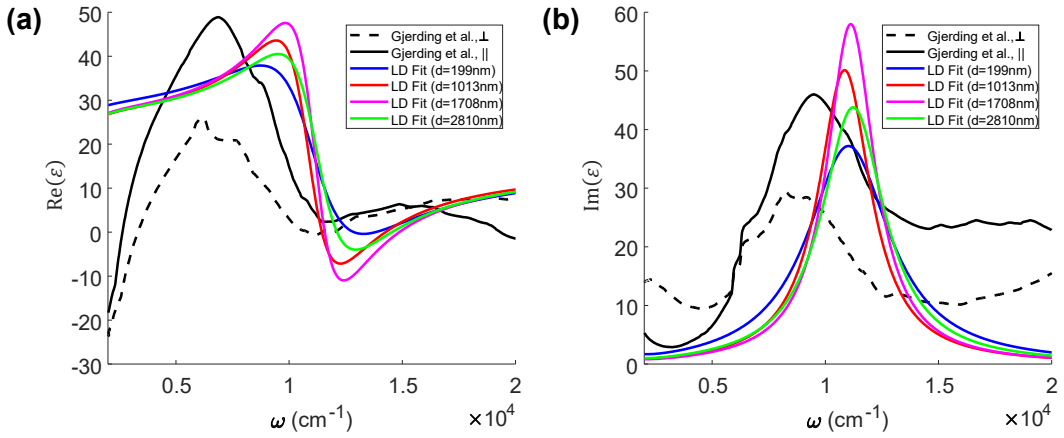

Figure 13. Comparison of the dielectric constants $\varepsilon(\omega)$ of $PtSe_2$ (in extend frequency range including visible region) between the one obtained by first-principles calculations done by Gjerding's group [146] and by fitting the measured reflectivity $R(\omega)$ derived from the single-Lorentz-Drude model.

4.3.6 Anisotropic Properties

Layered materials such as $PtSe_2$ should have pronounced anisotropic properties, and thus the dielectric constant should be different for out-of-plane and in-plane directions. Gjerding et al. [146] has calculated both the in-plane and out-of-plane dielectric constants $\varepsilon_{\parallel}$ and $\varepsilon_{\perp}$ for bulk $PtSe_2$ by first-principle calculation, the results

of which are plotted in Figure 13, in which the solid (dashed) black lines refer in-plane (out-of-plane) dielectric constant $\varepsilon_{||}(\varepsilon_{\perp})$. One can see that there is a certain degree of anisotropy for the dielectric constants. However, for fitting the $R(\omega)$, the dielectric constant of $PtSe_2$ is assumed to be isotopic. This assumption may be the cause of the discrepancy between the measured and calculated R spectra. Also, only one Lorentzian term was used which may not be accurate enough. Moreover, the Lorentz-Drude model (Equation (30)) is only a simple model and should be replaced by better models such as the hydrodynamic model and the Lindhard model [147]. Figure 13 shows the comparison between the calculated dielectric constants from Gjerding's group and the ones fitted to measured FTIR reflectivity spectra. The fitted curves do not agree well with Gjerding's work. Besides, reflectivity spectra from Gjerding's data have been calculated (non-shown) and they do not agree well with the measured spectra while our fitted data follow the general trend of the measured spectra (Figure 11), especially for frequency ranging from 500 to 4000 cm^{-1}. As a result, the fitted dielectric constants will be used for studying optical properties of the $PtSe_2$.

4.3.7 Kramers-Kronig Analysis

Kramers-Kronig (KK) analysis (Section 2.2.2.5) was also employed for testing the reliability of the fitted dielectric constant of the $PtSe_2$ from the reflectivity $R(\omega)$ (Section 4.3.2). The methodology is presented as follows. For the Air/$PtSe_2$/Au, a 3-layer system, the Fresnel reflection coefficient $r(\omega)$ for 3-layer system is represented by Equation (40). This complex valued $r(\omega)$ can be expressed by Euler's formula

$$r(\omega) = \sqrt{R(\omega)}\exp\big(i\theta(\omega)\big) \tag{78}$$

or equivalently $\ln r(\omega) = \ln\sqrt{R(\omega)} + i\theta(\omega)$, where $\sqrt{R(\omega)}$ and $\theta(\omega)$ are the modulus and the phase of $r(\omega)$ respectively. $R(\omega)$ can be obtained by conventional FTIR spectroscopy, just like the work presented in Section 4.3.1. In contrast, the phase spectrum $\theta(\omega)$ is relatively difficult to be obtained. Nonetheless, by analogy to Equation (33), for such a linear response system: $E_{\text{refl}} = r(\omega)E_{\text{inc}}$, the KK relation allows determining the imaginary part of In $r(\omega)$, that is $\theta(\omega)$, directly from the real part In$\sqrt{R(\omega)}$ by [148, 149]:

$$\theta(\omega) = -\frac{\omega}{\pi}\mathrm{P}\int_0^{\infty}\frac{\ln R(\omega)}{s^2-\omega^2}ds, \tag{79}$$

where P represents the principal part of the integral. Therefore, with the FTIR spectrum $R(\omega)$ and the phase spectrum $\theta(\omega)$ by KK analysis (Equation (79)), the complex reflection coefficient $r(\omega)$ for the three-layer system can be extracted by using Equation (78). From that experimental $r(\omega)$, the dielectric constant $\varepsilon(\omega)$ of $PtSe_2$ can be obtained by solving Equation (40) numerically.

With the methodology above, KK analysis was applied on the reflectivity spectrum $R(\omega)$ of the 1013-nm-thick $PtSe_2$ sample (Figure 11(b)). The phase spectrum $\theta_{KK}(\omega)$ can be obtained by Equation (79) and the $\theta_{KK}(\omega)$ spectrum with offset value π is plotted as dotted red line in Figure 14(a). Calculation was performed by the use of the MATLAB programme given by V. Lucarini [150]. In Figure 14(a), the theoretically calculated $\theta_{LD}(\omega)$ spectrum is also plotted, by the use of the LD-fitted dielectric constant of $PtSe_2$, which is shown by red lines in Figure 12(a) and replotted as black lines in Figure 14(b). The theoretical $\theta_{LD}(\omega)$ was calculated by finding the

argument of the theoretical effect reflection coefficient $r(\omega)$, which, for small incident angle, can be expressed by [151]:

$$r = \frac{r_s - r_p}{2}. \tag{80}$$

Figure 14(a) shows that although the phase spectrum $\theta_{KK}(\omega)$ does not exactly match with the theoretical $\theta_{LD}(\omega)$, it follows the general trend, especially in the frequency range 1000 – 3000 cm^{-1}. As a result, although the numerically solved dielectric constant $\varepsilon_{KK}(\omega)$ from KK analysis, as shown in Figure 14(b), does not match well with the Lorentz-Drude one, $\varepsilon_{LD}(\omega)$, it follows the trend of $\varepsilon_{LD}(\omega)$. This confirms the validity of the Lorentz-Drude model fitted dielectric constant of the $PtSe_2$ (Table 1 and Figure 12(a)). The LD fitted $\varepsilon(\omega)$ will be used for studying the optical properties of the $PtSe_2$.

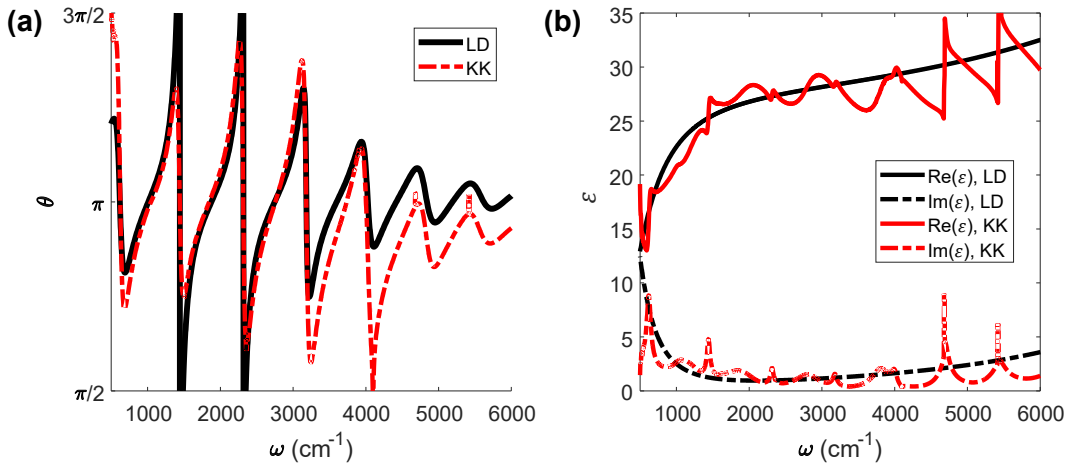

Figure 14. Comparison between Kramers-Kronig (KK) analysis and Lorentz-Drude (LD) fitting. KK analysis was applied on the reflectivity spectrum of the 1013-nm-thick $PtSe_2$ flake on the Au substrate (Figure 11(b)). (a) Dash-dot line represents the phase spectrum $\theta(\omega)$ of Fresnel reflection coefficient $r(\omega)$ by KK analysis (Equation (79)) of reflectivity spectrum $R(\omega)$ while black line refers to $\theta(\omega)$ calculated by LD model fitted $\varepsilon(\omega)$ (Table 1). (b) Black lines refer to dielectric constant $\varepsilon(\omega)$ of the $PtSe_2$ obtained by KK analysis while red lines refer to LD model fitted value as shown in Table 1.

4.4 Nano-Imaging of $PtSe_2$

As shown by FTIR reflectivity spectra in Figure 11, the $PtSe_2$ flakes show Fabry–Pérot (FP) cavity effect, which is a characteristic effect for dielectric materials. Therefore, the air/$PtSe_2$/SiO_2/Si layered structure, should support the optical waveguide modes in MIR range. In this work, elastic s-SNOM was employed to image the waveguide modes of the $PtSe_2$ directly in real-space. Figure 15 shows the schematic diagram of the nano-imaging on waveguide modes in $PtSe_2$ near a specific sample edge, whose direction is represented by the y-axis. The x-axis represents the lateral scanning direction. As mentioned in Section 2.5, a monochromatic p-polarized

laser beam with wavevector k_0 and incident angle $\alpha \approx 40^o$ is focused on the AFM tip during scanning. This illuminated AFM tip with apex radius $a \approx 30$ nm can generate a strong near field having a size in subwavelength dimension near the tip apex. During scanning, this nano-spot, which provides sufficient momentum to overcome the momentum mismatch between these modes and photons in air [53], can excite the waveguide modes inside the $PtSe_2$ sample which is underneath the tip. It is known that the waveguide-induced nano-images is sensitive to the orientation of the sample edge near where the scanning is performed. Therefore, a sample-edge orientation angle β is introduced in this work. As shown in the top view (Figure 15(b)), this angle β is defined as the angle between the projected light beam direction k_{xy} and the y-direction.

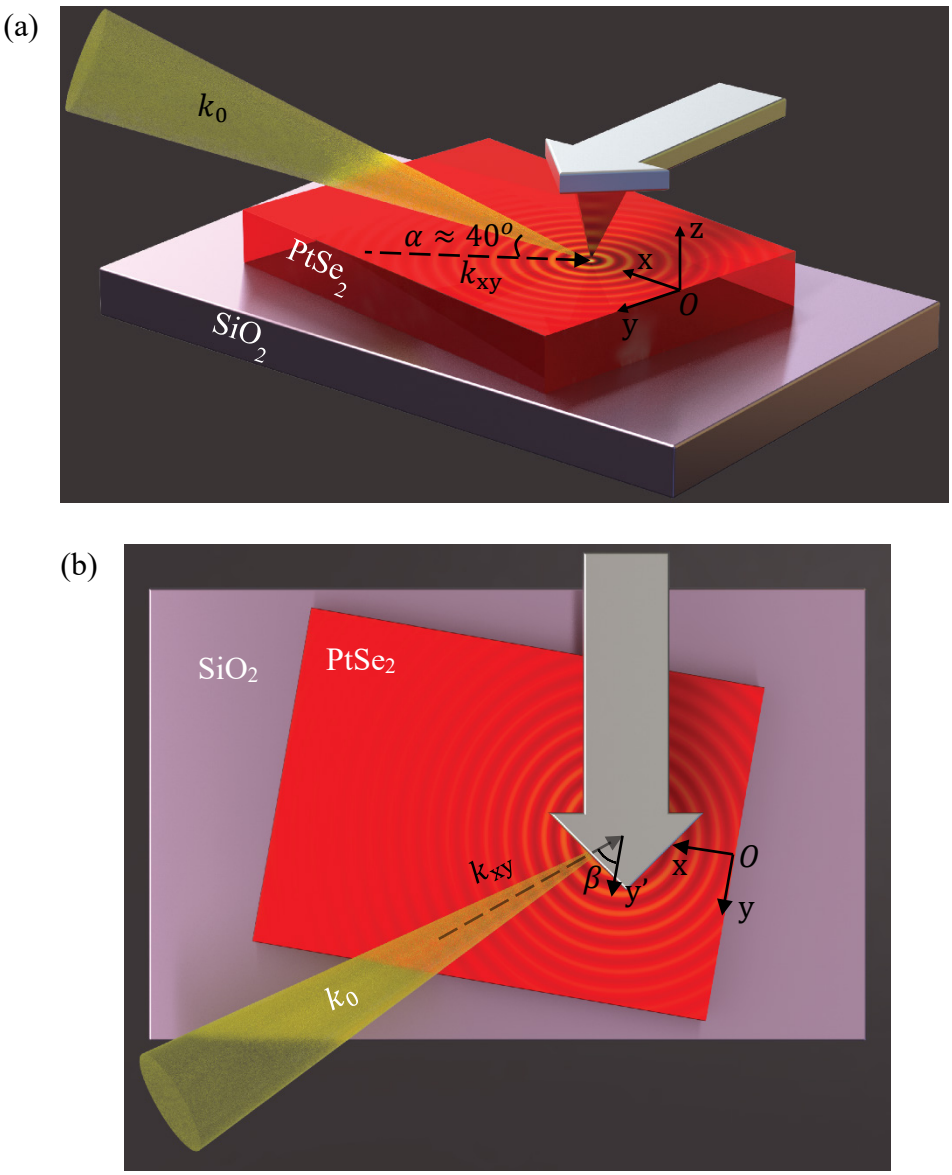

Figure 15. (a) Side view and (b) top view of the schematic diagram of near-field optical study of the $PtSe_2$ flake. Waveguide modes are excited in the $PtSe_2$ flake by the illuminated AFM tip. The y-axis represents the specific sample edge near which the scanning process is performed and the x-axis represents the lateral scanning direction. The incident direction of the laser is labeled by the angle $\alpha \approx 40^o$. The angle β is the sample-edge orientation angle, defined as the angle between the projected light beam direction k_{xy} and the y-direction. The waveguide-induced nano-image is sensitive to that angle β.

As mentioned above, the waveguide-induced nano-image is sensitive to the sample-edge orientation angle β. That means when rotating the sample about the point of the AFM tip, and performing the scanning (still with lateral direction parallel with the x-axis and near the same sample edge represented by y-axis), a different image will be generated, even though the scanning is performed on the same sample and near the same sample edge. This phenomenon can be explained if the mechanism of signal collection is known. By adapting the idea of Hu [50], the backscattered signal collection processes for two specific cases with sample-edge orientations, $\beta = 60^o$ and $\beta = 240^o$, are illustrated in Figures 16 (a) and (b) respectively. In both cases, the sample edges (represented the y-axis) are parallel to the cantilever of the AFM tip, but one edge is on the right size of the cantilever while another is on the left so that these edge orientations refer to different β. As shown in the top views in Figure 16 (a) and (b), and also referring to Figure 15(b), the sample-edge orientation angles for these two case are $\beta = 60^o$ and $\beta = 240^o$ respectively. For typical test in s-SNOM, there is only P1 pathway contribution to the backscattered signal, which refers to the light directly scattered in the AFM tip. For a sample supporting waveguide modes, there is another pathway, P2, contributing the backscattered signal. The formation of P2 is originated by the excitation of waveguide modes (with momentum k_p) inside $PtSe_2$. These waveguide modes propagate radially and reach the edge of the $PtSe_2$ and then partially scatters to air and then collected by the parabolic mirror. The parabolic mirror mainly collect the edge-scattered light with direction parallel to the incident beam, and thus the collected edge-scattered light has an angle α (same value as the incident angle $\alpha = 40^o$, as shown in Figure 15(a)) with the sample plane. As illustrated in Figures 16 (a) and (b), although the P1 pathways are the same in different β, P2 pathways are different. As a result, it is expected that the s-SNOM images of the waveguide modes

are edge orientation dependent (β dependent). The results of the s-SNOM study of the 579 nm $PtSe_2$ flake on SiO_2/Si substrate at the sample edge orientation angles $\beta = 60^o$ and $\beta = 240^o$ are shown in Figure 17. Figures 17(a) and 17(b) refer to the original SNOM s_3 (the third harmonic amplitude) images taken at frequency $\omega = 2519\ \mathrm{cm}^{-1}$ and the corresponding line profiles. Here, interference fringes parallel to the edge of the $PtSe_2$ are observed in both cases. Although images are taken from the same sample, the fringe patterns are different from one another. The baselines (cyan lines) of the line profiles are also plotted in Figures 17(a) and 17(b). Subtracting the baseline signals from the original ones, the baseline-corrected images and line-profiles can be obtained and are shown in Figures 17(c) and 17(d). Not only the baseline-corrected image for $\beta = 60^o$ but also the one for $\beta = 240^o$ exhibits clear decaying property. Also, the fringe patterns are clearer after removing the envelop. Still, these baseline-corrected images for different β are still different from each other.

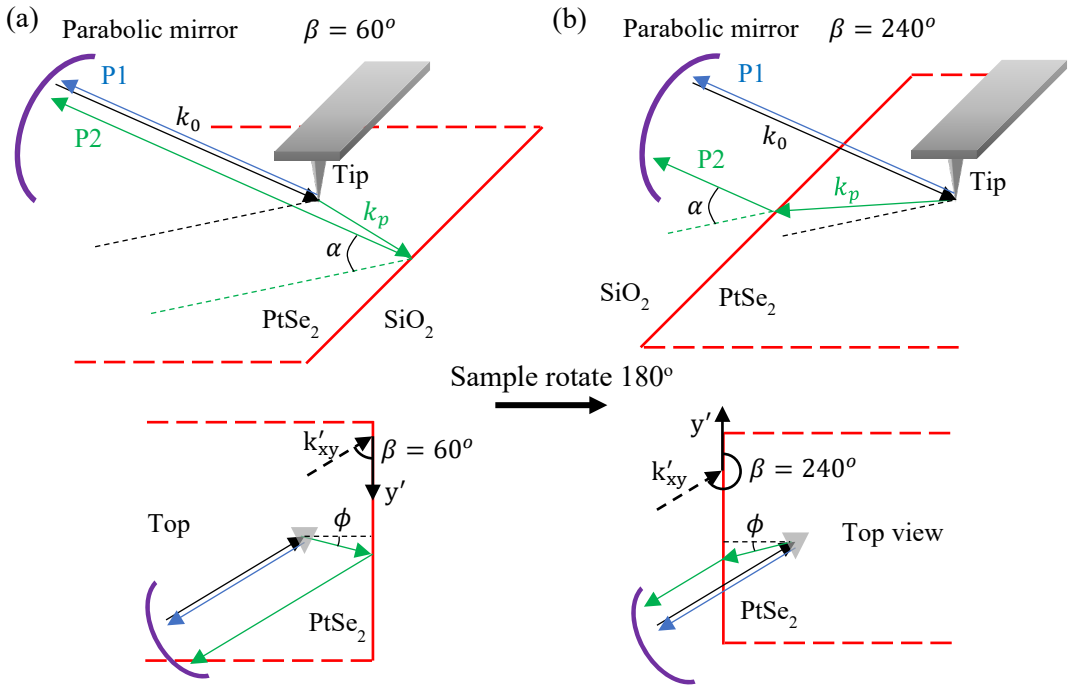

Figure 16. Illustration of the collection of the backscattered signal. In additional to the common P1 pathway contribution, there is P2 pathway generated by optical waveguide modes (with momentum k_p) inside $PtSe_2$. In each case, the edge is parallel to the cantilever of the AFM tip, but these cases refer to different sample edge orientation angles β. (a) refers to $\beta = 60^o$ while (b) refers to $\beta = 240^o$.

The edge orientation dependence is not produced by other in-plane propagative modes such as the surface plasmon polaritons (SPP) and surface phonon polaritons (SPhP). By pervious s-SNOM study on SPP in graphene [41, 42] and SPhP in h-BN [43, 44] and α-MoO_3 [45, 46], fringe patterns have also been imaged but they are independent on the edge orientation. For SPP and SPhP supporting materials, the s-SNOM tip launches the polaritons which propagate as cylindrical wave and reflects at the edge of the sample and finally return to the tip position. It is the interference between tip-launched and the reflected polaritons produces the fringes in s-SNOM images. Based on this mechanism, the fringe patterns by SPP and SPhP are

independent of the edge orientation. On the other hand, pervious s-SNOM studies on materials supporting waveguide modes, such as $MoSe_2$ [50] and MoS_2 [51], show the edge orientation dependent. Therefore, the fringe patterns in the s-SNOM images taken on the $PtSe_2$ (Figures 17(a) and 17(b)) should be originated from the waveguide modes inside the $PtSe_2$ flake.

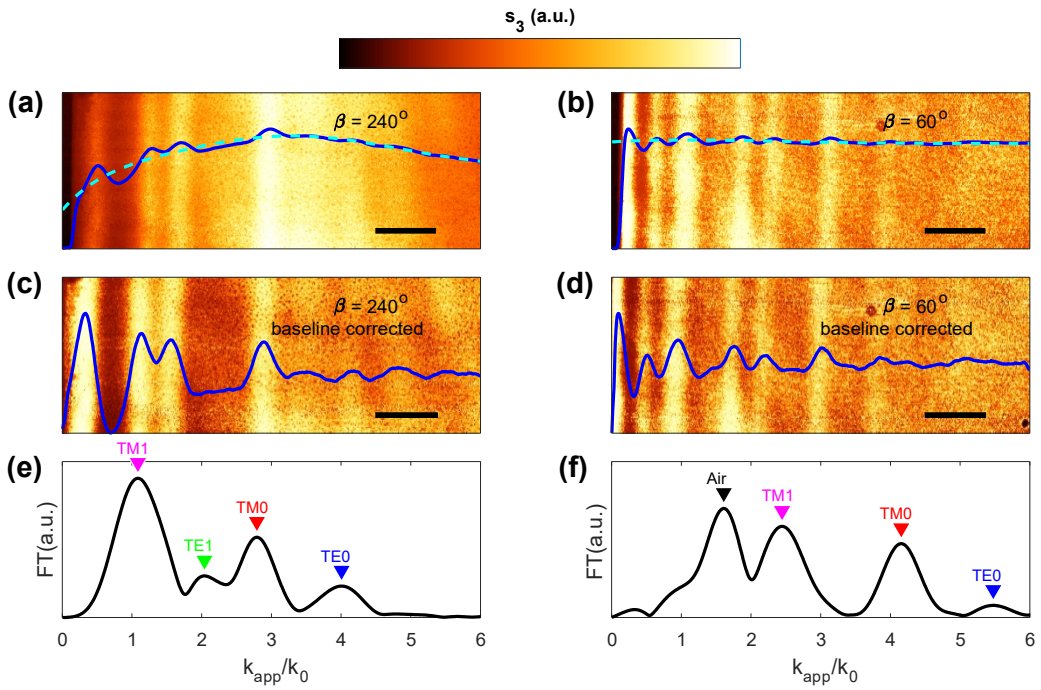

Figure 17. Near-field optical study of a 579nm-thick $PtSe_2$ flake on SiO_2/Si substrate. Images are taken at $\omega = 2519\ \mathrm{cm}^{-1}$ with scanning area 5μm × 15μm. (a, b) s-SNOM s_3 images for $\beta = 60^o$ and $\beta = 240^o$. Blue lines refer to the corresponding line-profiles while cyan lines are the corresponding baselines. (c, d) The baseline-corrected result of (a) and (b). (e, f) Discrete Fourier Transform (DFT) analysis on the baseline-corrected profiles in (c) and (d) respectively. The black inverted triangle refers to air mode while other colored triangles indicate the type of waveguide modes inside the $PtSe_2$ flake. Scalebars in (a-d) refer to 2 μm.

From Figures 17(c) and 17(d), the fringe patterns appear to be complicated and should be a superposition of different wavelengths. Therefore, Discrete Fourier Transform (DFT) analysis is performed on the baseline-corrected line-profiles in order to determine the correct fringe periodicities λ_{app}. Hanning windowing function was used for apodization in FT analysis. The obtained FT profiles are plotted in Figures 17(e) and 17(f). There are multiple peaks in both FT profiles and these peaks refer to the apparent wavevectors $\left(k_{\mathrm{app}} = \frac{2\pi}{\lambda_{\mathrm{app}}}\right)$ of the corresponding s_3-profiles. According to the analysis below, these peaks refer to different types of propagation modes (marked by coloured downward-pointing triangles). One can see that the modes of same type appear to have different apparent wavevectors k_{app} for different edge orientations.

4.5 Edge Orientation Dependence

In order to explore the nature of the sample edge orientation dependence of the fringe pattern, near-field optical study was performed at full range of the sample edge orientation angles, $0^o < \beta < 360^o$. The s-SNOM s_3 images and the corresponding line-profiles (normalized to the signal of SiO_2, as discussed in Section 2.7.6) are presented in Figure 18. As shown by the original images and line-profiles in Figures 18(a) and 18(b), the interference fringes parallel to the edge of the $PtSe_2$ flake occur at every β but the patterns change with β. Every image appears to be superposition of the oscillations with different periodicities. Generally, the periodicities decrease from $\beta \sim 0^o$ to $\beta \sim 90^o$ and then increase from $\beta \sim 90^o$ to $\beta \sim 270^o$ and finally decreases

again from $\beta{\sim}270^o$ to $\beta{\sim}360^o$. Another observation is that for angles near $\beta{\sim}270^o$, the fringe patterns only vary slightly, compared to other β values. The envelop in the signal seems to hide the fringe pattern, especially for $222^o \leq \beta \leq 327^o$. Nevertheless, The envelop can be removed by baseline-correction and the results is shown in Figures 18(c) and 18(d). The fringe patterns are clearer for these baseline-corrected results and all the line-profiles appear to decay from the sample edge $(\mathrm{x} = 0\ \mu\mathrm{m})$, which is consistent with the assumption that the waveguide modes propagating radially from the tip.

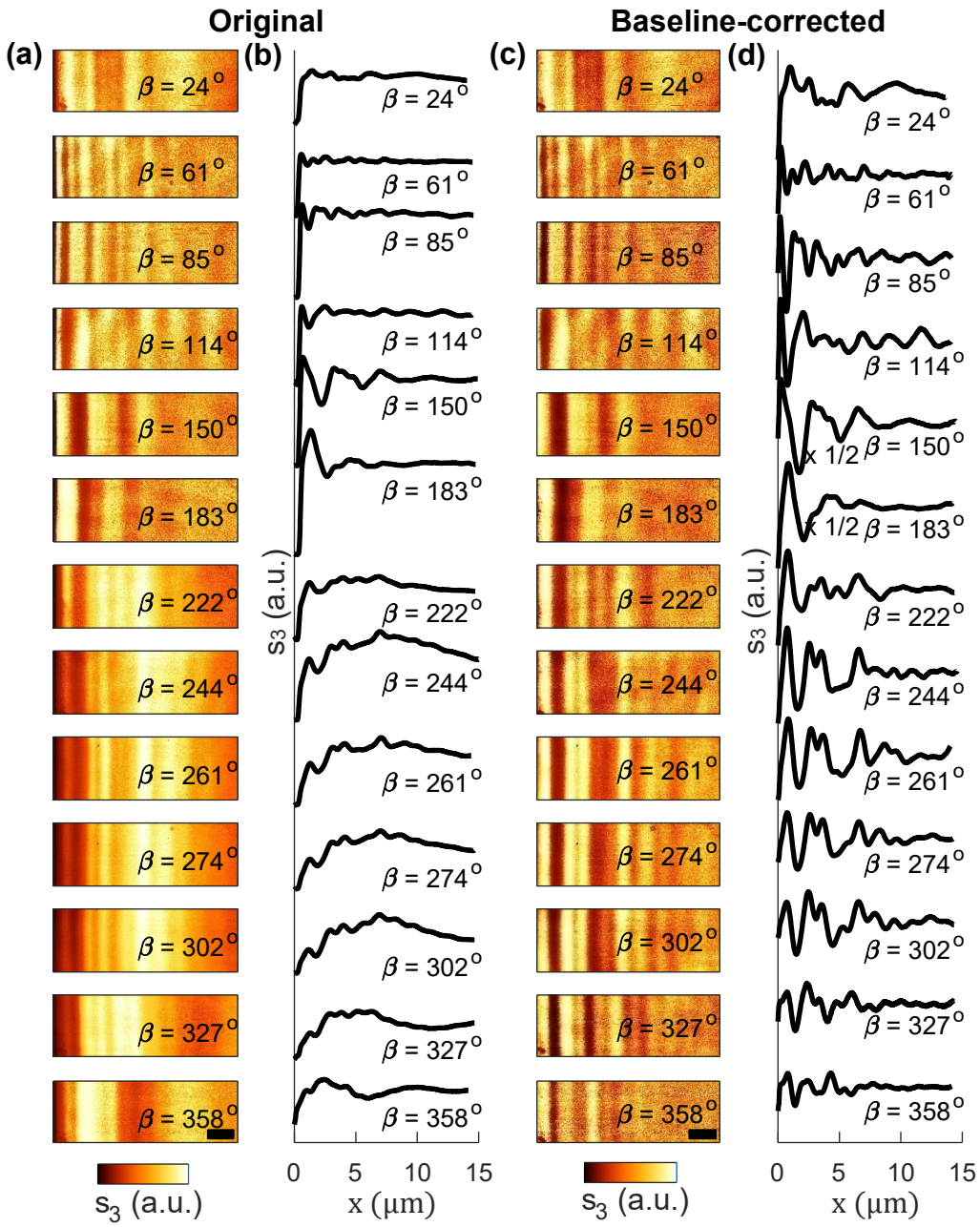

Figure 18. Sample edge orientation dependence of the s-SNOM images of a 579nm-thick $PtSe_2$ sample, taken at frequency $2519\ cm^{-1}$ with scanning area $5\mu m \times 15\mu m$. (a, b) original near-field amplitude s_3 images at various sample edge orientation angles β and the corresponding line-profiles (normalized to the signal of SiO_2.). (c, d) Baseline-corrected images and line-profiles of (a) and (b). Scalebars in (a) and (c) represent 2 μm.

In order to study the dependence of the periodicities λ_{app} on the edge orientation angle β, DFT analysis is performed on every baseline-corrected line-profiles. The corresponding FT profiles are given in Figure 19(a), where the dominant peaks refer to apparent wavevectors $\left(k_{\mathrm{app}} = \frac{2\pi}{\lambda_{\mathrm{app}}}\right)$ of the corresponding s_3-profiles. These dominant peaks are marked with coloured squares which indicates the type of waveguide modes (or the air mode) they belong to, according to the dispersion analysis as will be discussed below. From Figure 19(a), one can see that each type of the in-plane waveguide mode with specific in plane wavevector k_{p} has different values of k_{app} as β varies. The variation of k_{app} appears to have a general trend for all the modes: for $0^o \leq \beta \leq 90^o$, k_{app} increases from its minimum and reaches it maximum at $\beta = 90^o$; for $90^o \leq \beta \leq 270^o$, k_{app} decreases; for $270^o \leq \beta \leq 360^o$, k_{app} increases again. Another observation is that, different from other modes, the apparent wavevectors k_{app} of the air mode (marked by black squares, $k_{\mathrm{p}} = k_0$) are unable to be resolved when β is near 270°. It may be caused by the baseline remove process, in which the envelop of the signal is removed. Therefore, the envelop with large periodicity near $\beta = 270^o$ seems to be originated from the air mode.

To quantitively explore the dependence of the apparent wavevector k_{app} of an waveguide mode with specific wavevector k_{p} on β, one should refer back to Figuregf 16, which show the schematic diagrams of the backscattered light collection for the sample supporting waveguide modes. There are two pathways, P1 and P2, for the backscattered light collected by the parabolic mirror. P1 refers to the light directly scattered at the tip and propagating parallel to the illuminating beam (black arrow). For P2, the illuminated tip excites in-plane modes which propagate radially and

partially scatter to air when the modes reach the edge. When the tip scans along the path perpendicular to the edge, the path difference between P1 and P2 varies and produces interference fringe pattern parallel to the edge. As suggested by Hu [50], due to the small collection angle of the parallel mirror, for P2 it only collects the edge-scattered light parallel to the directly backscattered light (P1). Also, as illustrated in Figure 16, the edge-scattered light in P2 is mainly produced by the in-plane modes propagate with an angle ϕ relative to the shortest path to the edge, by the conservation of the momentum along the edge direction (generalized Snell's law). Hu's group [50] has studied two specific sample edge orientation cases, $\beta = 270^o$ and $\beta = 0^o$, for which they refer to 'perpendicular configuration' and 'parallel configuration' respectively. Here, Hu's idea is generalized to cover full range of edge orientation angle β. In this general case, the phase difference of the light between pathways P1 and P2 is:

$$\varphi = k_{\mathrm{p}} \frac{x}{\cos\phi} + k_0 \frac{x}{\cos\phi} \sin(\beta - \phi) \cos\alpha \tag{81}$$

where k_{p} is the in-plane wavenumber of waveguide modes, x is the tip-edge distance, $\alpha \approx 40^o$ is the angle between the incident light and sample plane and

$$\phi = \sin^{-1}\left(\frac{k_0}{k_{\mathrm{p}}} \cos\alpha \cos\beta\right) \tag{82}$$

is the propagating angle of tip-lunched waveguide modes. By substituting $x = \lambda_{\mathrm{app}}$ and $\phi = 2\pi$ in Equation (81), one can obtain the general expression of the fringe width λ_{app}:

$$\lambda_{\mathrm{app}} = \frac{\lambda_{\mathrm{p}}}{\frac{1}{\cos\phi} + \frac{\lambda_{\mathrm{p}}}{\lambda_0}\frac{\sin(\beta-\phi)\cos\alpha}{\cos\phi}}, \tag{83}$$

where λ_{p} and λ_0 are the wavelengths of waveguide modes and free-space photons. This general form can be reduced to the ones derived by Hu's group by putting $\beta = 270^{\mathrm{o}}$ and 0^{o}. From Equations (82) and (83), one can find the expression of the apparent wavenumber k_{app} by the relation $k_{\mathrm{app}} = 2\pi/\lambda_{\mathrm{app}}$:

$$k_{\mathrm{app}} = \frac{k_{\mathrm{p}} + k_0 \sin\left(\beta - \sin^{-1}\left(\frac{k_0}{k_{\mathrm{p}}}\cos\alpha\cos\beta\right)\right)\cos\alpha}{\cos\left(\sin^{-1}\left(\frac{k_0}{k_{\mathrm{p}}}\cos\alpha\cos\beta\right)\right)}. \tag{84}$$

This equation relates the apparent wavenumber k_{app} to the actual wavenumber k_{p} of a waveguide mode, and it shows the β dependence of k_{app}.

Figure 19(b) shows the variations of k_{app} with β by using Equation (84) for wavenumbers $k_{\mathrm{p}} = k_0, 1.8k_0, 3.6k_0, 4.7k_0$. Experimental data points in Figure 19(a) are overlaid on these calculated results. The results by the derived Equation (84) and the experiment are consistent and therefore the validity of Equation (84) is confirmed. This consistence also validates the discussion about the variation of k_{app} above: k_{app} of all the modes with wavenumber k_{p} varies with similar trend and becomes smallest when $\beta \sim 270^{o}$. Also, k_{app} of air mode ($k_{\mathrm{p}} = k_0$) becomes small and therefore, by $\lambda_{\mathrm{app}} = \frac{2\pi}{k_{\mathrm{app}}}$, the apparent wavelength of air mode becomes large ($> 15\mu\mathrm{m}$) and can produces an envelope with large periodicity in the signal, as shown in Figures 18(a) and 18(b). By this full range edge orientation study, one can confirm that, for 2519 cm-

[1] excitation, a 579 nm-thick $PtSe_2$ flake supports waveguide modes of types TM1 with $k_p = 1.8k_0$, TE1 with $k_p = 2.8k_0$, TM0 with $k_p = 3.6k_0$ and TE0 with $k_p = 4.7k_0$.

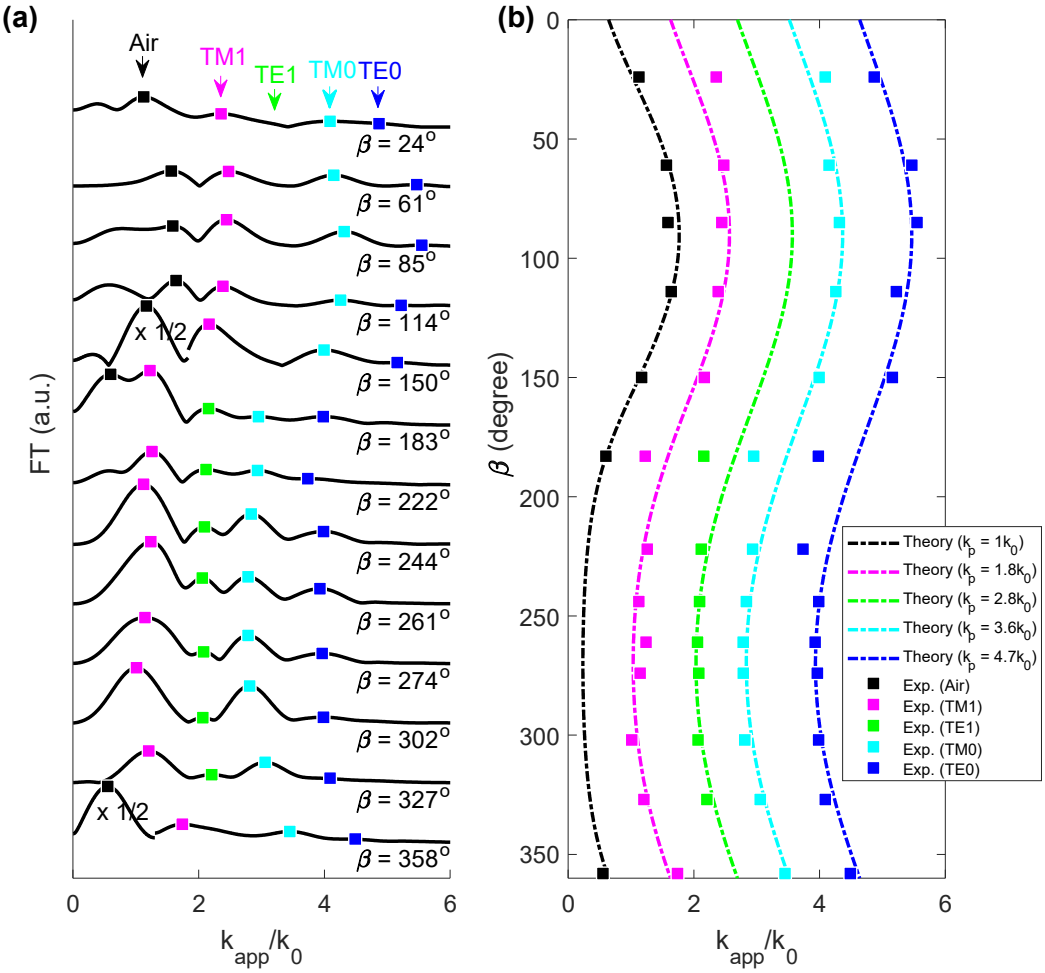

Figure 19. (a) FT-profiles of the baseline-corrected images and line-profiles in Figure 18(d). Colored squares represent different types of modes, as labelled in the top of the first FT-profile. Profiles are displaced vertically for clarity. (b) Calculated variations of the apparent wavenumbers k_{app} of the propagative modes with wavenumbers $k_p = k_0, 1.8k_0, 3.6k_0, 4.7k_0$. The experiment data set in (a) is overlaid on them.

4.6 Dispersion Analysis

Following the study on edge orientation dependence of the fringe pattern, the excitation frequency (ω) dependence of the pattern is hoped to be explored. In Figure 20, the original near-field optical amplitude s_3 images and their baseline-corrected images at various MIR frequencies are shown. Also, the line-profiles are superimposed on the corresponding images. From Figure 20, as ω decreases, the periodicity of the fringes also decreases, and the patterns become less complex. In order to quantitatively study the ω dependence of the fringe periodicity, FT is imposed on the baseline-corrected s_3 line-profiles as shown in Figure 20(b) and the corresponding k-space profiles are plotted in Figure 21(a). The peaks in the FT profiles refer to the apparent wavenumbers k_{app} of different waveguide modes (marked with inverted triangles). One can see that k_{app} shifts to lower values as ω of the laser source is tuned lower. Also, TE1 and TM1 disappear as ω is tuned lower.

Based on the obtained k_{app} at different ω in Figure 21(a), one can construct the experimental dispersion relation $\omega(k_{\mathrm{p}})$ (Section 2.2.5) of the waveguide modes by converting each k_{app} to k_{p}, with the use of Equation (84). The obtained dispersion data points (k_{p}, ω) are plotted as inverted triangles in Figures 21(c) and 21(d). These data points are overlaid on the theoretical dispersion curves (dash-dot lines) and dispersion colourmaps in where the bright regions refer to waveguide modes. According to the discussion on the loss function in Section 2.2.5.2, the dispersion colourmaps for TE and TM waveguide modes can be obtained by numerically evaluating the imaginary part of the Fresnel's reflection coefficients for s-polarized light $\mathrm{Im}(r_s)$ and p-polarized light $\mathrm{Im}(r_p)$ respectively. The coefficients r_s and r_p for the

air/$PtSe_2$/SiO_2/Si layered structure can be calculated by applying the Transfer-Matrix Method (Section 2.2.3.2)). This method for obtaining the dispersion colourmap is widely used to study the dispersion relation of surface polaritons such SPP in graphene [41, 42] and SPhP in h-BN [43]. For the calculation, the in-plane dielectric constant $\varepsilon_{\parallel}$ of the $PtSe_2$ is chosen to be the fitted value for 1013-nm-thick $PtSe_2$ (Table 1 and Figure 12(a)). Although TE mode dispersion relation calculation only relies on in-plane constant $\varepsilon_{\parallel}$, the TM mode calculation also requires the out-of-plane constant $\varepsilon_{\perp}$. The $\varepsilon_{\perp}$ is thus chosen to be 0.8 times the in-plane value to fit the experimental dispersion relations. Apart from the method based on loss function, the dispersion curves (dash-dot lines) can also be obtained by solving the eigenequations of the waveguide modes. The air/$PtSe_2$/SiO_2/Si structure is a 4-layer structure. Nonetheless, the fitted in-plane dielectric constant of $PtSe_2$ (Figure 12) reveals that in MIR the $PtSe_2$ has much higher refractive index that that in the upper ($\varepsilon_{\mathrm{air}} \approx 1$) and lower layers ($\varepsilon_{\mathrm{Si}} \approx 11.7$), so that waveguide modes can be mostly confined to the $PtSe_2$ layer. As a result, it is reasonable to approximate the system to be a three-layer system. As discussed in Section 2.2.5.1, the eigenequations for TE and TM waveguide modes for a 3-layer structure can be obtained by setting denominator of $r_{(\mathrm{p,s})}$ (Equation (40)) to be zero, that is, $1 + r_{1\to2}^{(s,p)} r_{2\to3}^{(s,p)} e^{2jk_{z_2}d_2} = 0$. As a result, the eigenequations for TE and TM waveguide modes for the 3-layer structure (Air/$PtSe_2$/SiO_2) are [80, 152, 153]

$$\sqrt{\varepsilon_{2,\parallel}{k_0}^2 - {k_\mathrm{p}}^2}\, d_2 = \tan^{-1}\left(\frac{\sqrt{{k_\mathrm{p}}^2 - \varepsilon_1 {k_0}^2}}{\sqrt{\varepsilon_{2,\parallel}{k_0}^2 - {k_\mathrm{p}}^2}}\right) + \tan^{-1}\left(\frac{\sqrt{{k_\mathrm{p}}^2 - \varepsilon_3 {k_0}^2}}{\sqrt{\varepsilon_{2,\parallel}{k_0}^2 - {k_\mathrm{p}}^2}}\right) + m\pi \tag{85}$$

and

$$\sqrt{\frac{\varepsilon_{2,\parallel}}{\varepsilon_{2,\perp}}}\sqrt{\varepsilon_{2,\perp}{k_0}^2-{k_\mathrm{p}}^2}\,d_2=\tan^{-1}\left(\frac{\varepsilon_{2,\parallel}}{\varepsilon_1}\frac{\sqrt{{k_\mathrm{p}}^2-\varepsilon_1{k_0}^2}}{\sqrt{\frac{\varepsilon_{2,\parallel}}{\varepsilon_{2,\perp}}}\sqrt{\varepsilon_{2,\perp}{k_0}^2-{k_\mathrm{p}}^2}}\right)+\tan^{-1}\left(\frac{\varepsilon_{2,\parallel}}{\varepsilon_3}\frac{\sqrt{{k_\mathrm{p}}^2-\varepsilon_3{k_0}^2}}{\sqrt{\frac{\varepsilon_{2,\parallel}}{\varepsilon_{2,\perp}}}\sqrt{\varepsilon_{2,\perp}{k_0}^2-{k_\mathrm{p}}^2}}\right)+n\pi \qquad (86)$$

respectively, where ε_i is the dielectric constant of the layer i, d_2 is the thickness of the second layer ($PtSe_2$ in this case) and m and n are the order numbers (non-negative integers) of the waveguide modes.

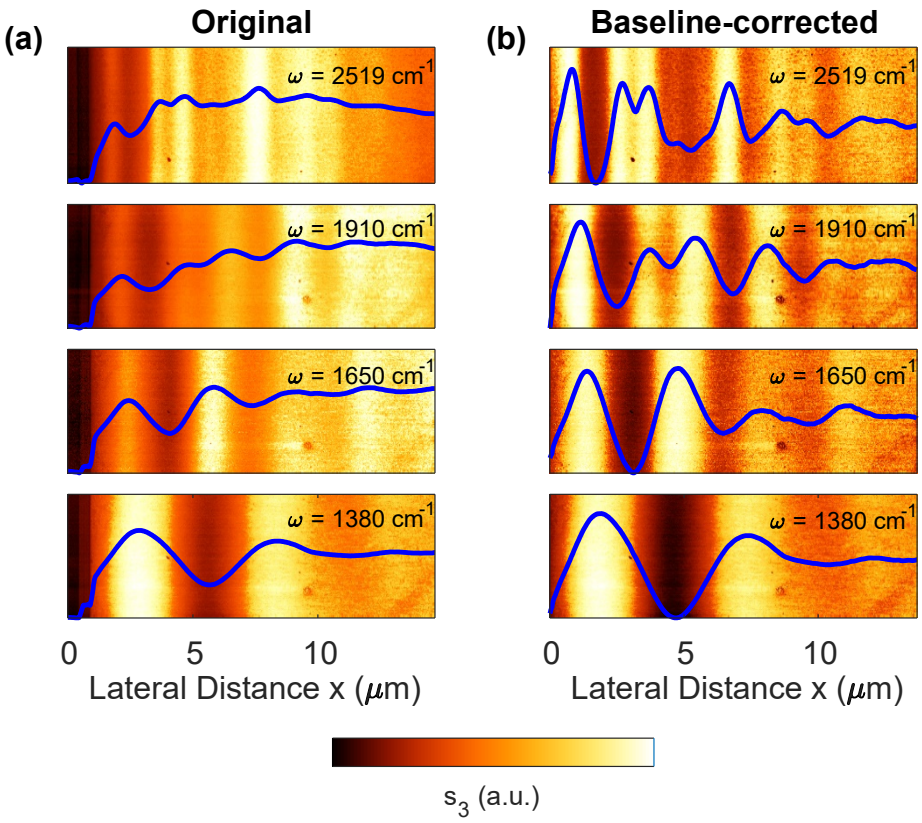

Figure 20. s-SNOM images taken at various frequencies ω for a 579 nm-thick $PtSe_2$ sample at sample edge orientation angle $\beta = 253^o$ with scanning area 5μm × 15μm. (a) Original near-field amplitude s_3 images and the corresponding line-profiles (normalized to the signal of SiO_2.). (b) Baseline-corrected images and line-profiles of (a).

From Figures 21(c) and 21(d), one can find that both methods predict the same dispersion relation $\omega(k_{\mathrm{p}})$ of the $PtSe_2$ structure. Also, there is a good agreement between the experiment data points and the calculated dispersion relations, and thus one can now identify the type of the waveguide modes for the peaks in the FT-profiles (Figure 21(a)). However, the air mode cannot be resolved due to the baseline-correction process, which removes the air-mode-induced envelop of the signal. Therefore, similar test for $\beta = 61^o$ was performed and the results is shown in Figure 22(a). At this edge orientation, there is a dominant oscillation in each ω, and it should be attributed to the air mode. By applying same methodology, the FT-profiles for $\beta = 61^o$ are shown in Figure 21(b) and the corresponding dispersion data points are plotted (marked by coloured diamonds) in Figures 21(c) and 21(d). Although the TE1 modes cannot be resolved, the experimental data points for air mode match with the calculated results. Also, the extracted TE0 dispersion points agree with the calculated results. Therefore, the results at different β are complementary. By dispersion analysis at several β, the dispersion relation of a sample can be extracted. Based on the same methodology, the same dispersion analysis is performed on the sample with a different $PtSe_2$ thickness. The near-field images for a 696 nm-thick $PtSe_2$ sample at $\beta = 272^o$ and $\beta = 64^o$ are shown in Figures 23 and 22(b) respectively. The corresponding results of dispersion analysis are shown in Figure 24. Again, the experimental dispersion data points agree well with the calculated dispersion relation.

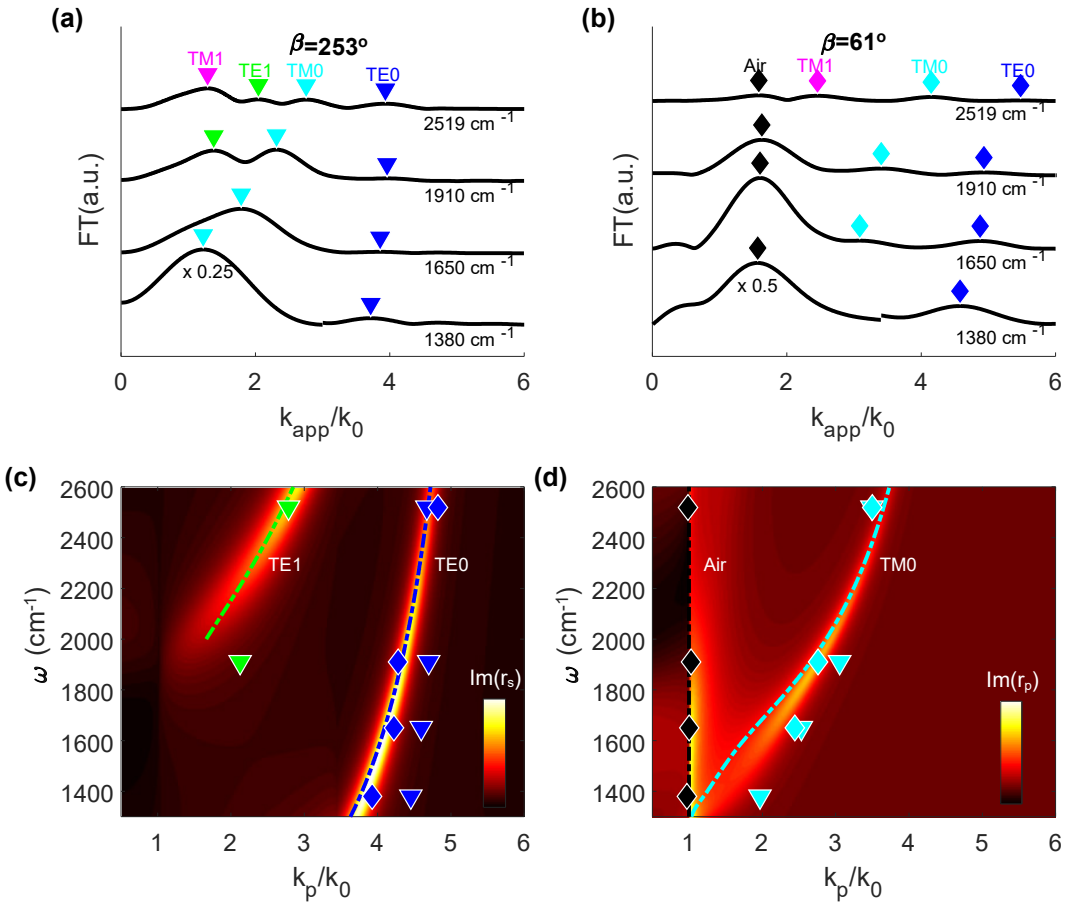

Figure 21. Dispersion analysis of a 579 nm-thick $PtSe_2$ sample. (a, b) Fourier Transform profiles of baseline-corrected s_3 line-profiles in Figure 16(b) ($\beta = 253^o$) and in Figure 22(a) ($\beta = 61^o$). Profiles are displaced vertically for clarity. (c, d) Experimental dispersion data points obtained by converting k_{app} (found in (a) and (b)) to k_{p} by Equation (84), overlaid on the calculated dispersion color-plots ($\mathrm{Im}(r_{s,p})$) and calculated dispersion curves (colored lines) by numerically solving eigenequations (85) and (86).

The FT analysis shown in Figures 21 and 24 reveals that not only the TM waveguide modes, but also the TE modes are excited and imaged by s-SNOM in MIR frequency. Although the aperture-type SNOM (a-SNOM) has been used to image both TE and TM modes in WSe_2 [48], scattering-type SNOM (s-SNOM) with the use of p-polarized light source is believed to be only able to launch TM modes. Pervious study shows

that TM waveguide modes in $MoSe_2$ can be excited and imaged by s-SNOM at visible frequency [50]. Nevertheless, Hu's group [51] has successfully employed s-SNOM for imaging both TM and TE waveguide modes in MoS_2 at NIR frequency. By studying $PtSe_2$ in this work, s-SNOM successfully recovers the TE modes at MIR range for the first time.

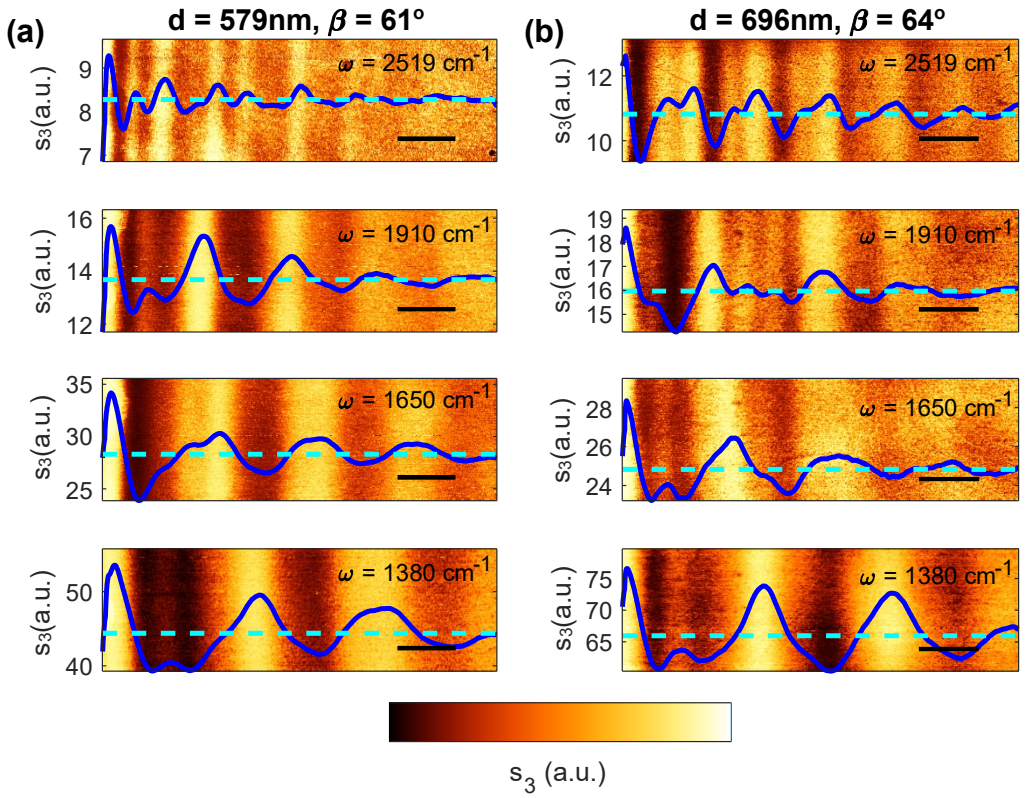

Figure 22. Baseline-corrected s-SNOM s_3 images taken at various frequency ω for (a) a 579 nm-thick $PtSe_2$ sample with scanning area $5\mu m \times 15\mu m$ at $\beta = 61^o$ and (b) a 696 nm-thick $PtSe_2$ sample at $\beta = 64^o$. The corresponding original s_3 line-profiles (normalized to the signal of SiO_2.) are overlaid on images. Scalebars represent 2μm. Cyan lines represent the baselines of the original s_3 profiles.

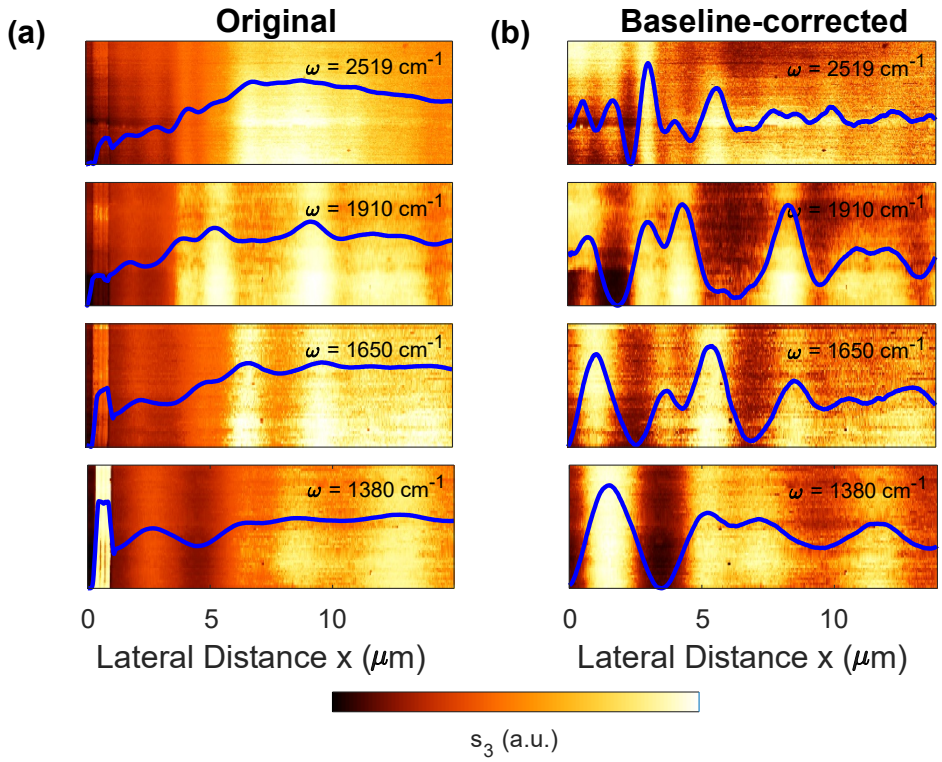

Figure 23. s-SNOM images taken at various frequencies ω for a 696nm-thick $PtSe_2$ sample at sample edge orientation angles $\beta = 272^o$ with scanning area 5μm × 15μm. (a) original near-field amplitude s_3 images and the corresponding line-profiles (normalized to the signal of SiO_2.). (b) Baseline-corrected images and line-profiles of (a).

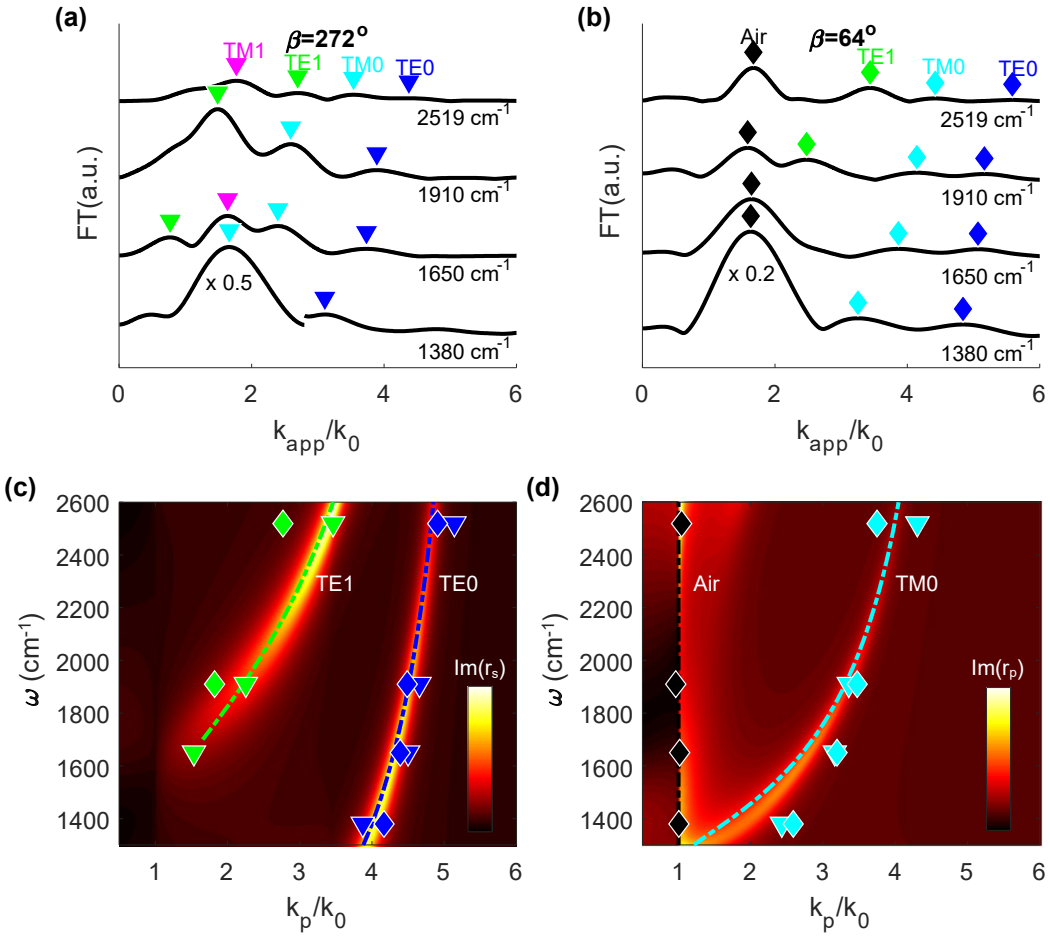

Figure 24. Dispersion analysis of a 696nm-thick $PtSe_2$ sample. (a, b) Fourier Transform profiles of the baseline-corrected s_3 line-profiles in Figure 20(b) ($\beta = 27^o$) and in Figure 22 ($\beta = 64^o$). Profiles are displaced vertically for clarity. (c, d) Experimental dispersion data points obtained by converting k_{app} (found in (a) and (b)) to k_p by Equation (84)), overlaid on the calculated dispersion color-plots and calculated dispersion curves (colored lines).

4.7 Propagating Length

In this Section, the propagating length of the waveguide modes is to be studied. Because the dielectric constant of $PtSe_2$ (Section 4.3.2) is a complex value, the in-plane propagation constant of a waveguide mode $k_{\mathrm{p}} = \sqrt{\varepsilon}$ is also a complex value, which has real part k'_{p} and imaginary part k''_{p}. For a tip-launched waveguide mode, its waveform is assumed as cylindrical wave $E = \frac{A}{\sqrt{r}} e^{i(k_{\mathrm{p}} r - \omega t)} = \frac{A}{\sqrt{r}} e^{-k''_{\mathrm{p}} r} e^{i(k'_{\mathrm{p}} r - \omega t)}$. Thus, the amplitude of intensity decays as $e^{-2k''_{\parallel} r_{\parallel}}$ and the propagating length is

$$L_p = \frac{1}{2k''_{\mathrm{p}}} = \frac{1}{2\mathrm{Im}(k_{\mathrm{p}})}. \tag{87}$$

One can relate k''_{p} to the waveguide modes' wavenumber k'_{p} (Appendix D), so that L_p for TE modes and TM modes can be found by k'_{p} via the relations

$$L_{p,\mathrm{TE}}(\omega) = \frac{k'_{\mathrm{p,TE}}(\omega)}{\mathrm{Im}(\varepsilon_{\parallel}) {k_0}^2} = \frac{k'_{\mathrm{p,TE}}(\omega)}{\varepsilon''_{\parallel} {k_0}^2} \tag{88}$$

for TE modes, and

$$L_{p,\mathrm{TM}}(\omega) = \frac{\frac{1}{2k'_{p,\mathrm{TM}}} \frac{\varepsilon''_{\parallel}\varepsilon'_{\perp} - \varepsilon'_{\parallel}\varepsilon''_{\perp}}{\varepsilon'_{\parallel}\varepsilon'_{\perp} + \varepsilon''_{\parallel}\varepsilon''_{\perp}}}{1 - \sqrt{1 + \left(\frac{\varepsilon''_{\parallel}\varepsilon'_{\perp} - \varepsilon'_{\parallel}\varepsilon''_{\perp}}{\varepsilon'_{\parallel}\varepsilon'_{\perp} + \varepsilon''_{\parallel}\varepsilon''_{\perp}}\right)^2 \left(1 - \frac{\left({\varepsilon'_{\perp}}^2 + {\varepsilon''_{\perp}}^2\right)\varepsilon''_{\parallel} k_0^2}{\left(\varepsilon''_{\parallel}\varepsilon'_{\perp} - \varepsilon'_{\parallel}\varepsilon''_{\perp}\right) {k'_{p,\mathrm{TM}}}^2}\right)}} \tag{89}$$

for TM modes, where the inverse dispersions $k'_{\mathrm{p,TE}}(\omega)$ and $k'_{\mathrm{p,TM}}(\omega)$ can be obtained by solving the TE and TM eigenequations (85) and (86) respectively. The calculated L_p for 696 nm-thick and 579 nm-thick $PtSe_2$ samples is shown in Figure 25. The L_p curves for TE modes have a similar shape with the skin depth of $PtSe_2$ (Figure 12(c)),

which becomes maximum when $\omega\sim1700\ \mathrm{cm}^{-1}$ and then keeps decreasing and becomes small for high frequency. Likewise, the L_p for different TE waveguide modes of $PtSe_2$ becomes maximum (about 4 μm for the TE0 mode) near the frequency $\omega\sim1700\ \mathrm{cm}^{-1}$ because the imaginary part of the dielectric constant, $\mathrm{Im}(\varepsilon_2)$, becomes minimum near that frequency (see Figure 12(a)). Afterwards, the propagation lengths L_p of different modes keep decrease when frequency increases because L_p is inversely proportional to ω^2 (Equation (888888) with the relation $ck_0 = \omega$). On the other hand, the L_p for the TM0 mode (Equation (89)) also has similar shape to that of TE modes, due to the assumption of small anisotropy ($\varepsilon_\perp = 0.8\varepsilon_\parallel$). Figure 25 reveals that the waveguide modes in the $PtSe_2$ have propagating length between about 1 and 4 μm, which is much smaller than the case in $MoSe_2$, which can be as large as 10 μm near $E = 1.3$ eV [50]. This relatively short propagating length of the $PtSe_2$ is consistent with the s-SNOM images as shown in Figures 20, 22 and 23. The smaller $L_p(\omega)$ may be due to the higher imaginary part of the in-plane and out-of-plane dielectric constant of the $PtSe_2$, as compared to $MoSe_2$, which has near zero values for both near excitation energy $E = 1.3$ eV [146, 154].

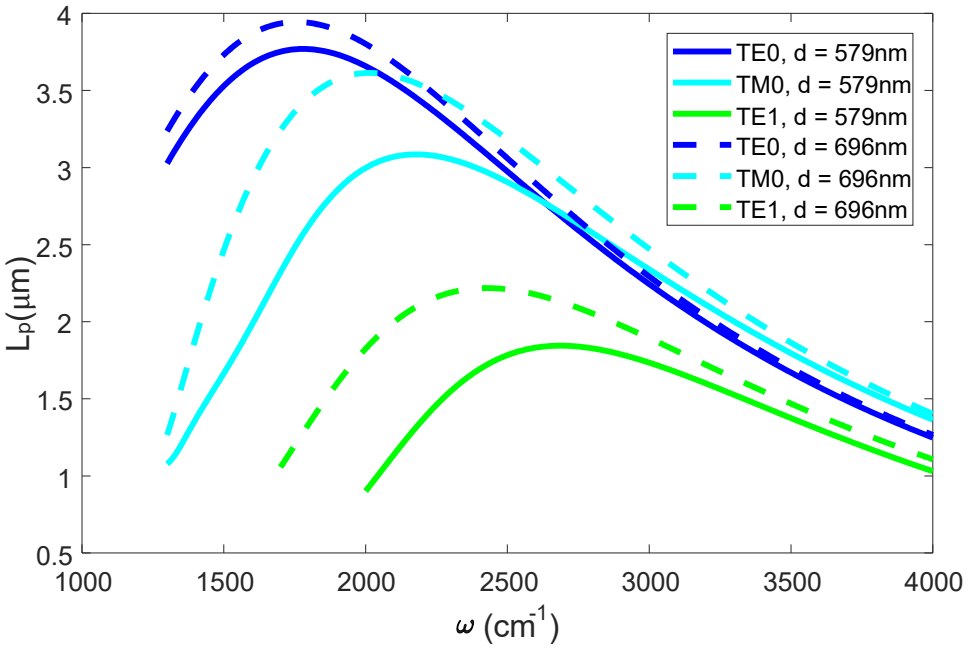

Figure 25. Propagation lengths L_p of TE0, TE1 and TM0 waveguide modes in 696 nm-thick and 579 nm-thick $PtSe_2$ samples.

4.8 Nano-FTIR Study

Following the study of waveguide modes in the $PtSe_2$, the dependence of near-field amplitude s on frequency ω is explored. In Figure 22, s-SNOM images and corresponding line-profiles for the $PtSe_2$ with thicknesses 579 nm and 696 nm are shown. One can see that in each image the s_3 signal normalized to SiO_2 (or equivalently the near-field contrast η_3, as discussed in Section 2.7.6) fluctuate about a mean value, as indicated by the baseline (cyan line). In Figure 26(a), the data points of the mean values against ω are plotted. The data points agree qualitatively with the calculated near-field spectrum $\eta_{3,PtSe_2/SiO_2}(\omega)$, by using the finite dipole model for bulk sample (Equation (59)). The experimental and theoretical results also show η_3 increases sharply for $\omega \sim 1400$ cm^{-1}, which might be due to the phonon resonance in

the SiO_2 substrate [119]. This method can obtain spectrum $\eta_n(\omega)$ but it is very inefficient. By contrast, nano-FTIR provides a powerful way to obtain $\eta_n(\omega)$ in a single measuring process and in nano-scale resolution. Figure 26(b) shows the measured $\eta_3(\omega)$ spectra for 87 nm-thick and 260 nm-thick $PtSe_2$ on Au substrate, by employing nano-FTIR. The measured result for d = 87nm has a good agreement with the calculated result, which is obtained by the Finite Dipole model for thin film (Equation (62)). For the 260 nm-thick sample, although the measured $\eta_3(\omega)$ does not match with the theory (Equation (59)), it has a similar shape with the calculated $\eta_3(\omega)$.

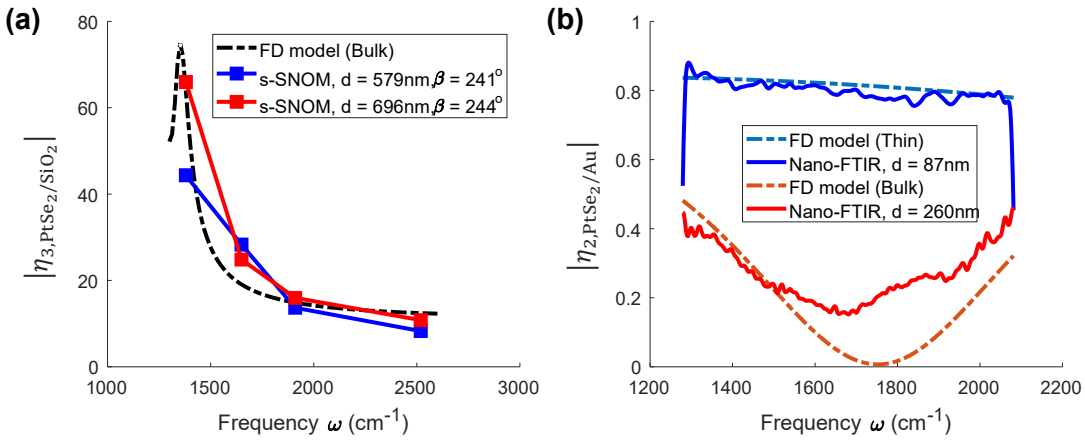

Figure 26. (a) The near-field spectra $\eta_3(\omega)$ of the $PtSe_2$, extracted from the s-SNOM images in Figure 22, overlaid on the calculated result by Finite dipole model. (b) The near-field spectra $\eta_2(\omega)$ of $PtSe_2$, measured by nano-FTIR, overlaid on the calculated result by Finite dipole model.

4.9 Summary

Using state-of-art scattering-type near-field optical microscope (s-SNOM), the optical waveguide modes inside the $PtSe_2$ flakes were imaged in real space with nanoscale resolution. The fringe patterns were observed, in spite of the short propagating lengths of these modes. With Fourier analysis, the sample edge orientation dependence of these patterns was studied. Also, by dispersion analysis, the dispersion relations of the waveguide modes were extracted, as well as confirmed by the theory. Interestingly, in addition to the commonly observed TM modes, the TE modes were also visualised in MIR range. This work shows the applicability of s-SNOM in MIR waveguide mode imaging. In addition, our work shows the MIR range complex dielectric constant of the $PtSe_2$ found by conventional far-field FTIR spectroscopy, which reveals the dielectric nature of bulk $PtSe_2$ in MIR region, although it is believed to be semimetallic. The far-field analysis shows that The $PtSe_2$ become less absorptive near the frequency $\omega \sim 1700\ \mathrm{cm}^{-1}$, where the skin depth becomes maximum. The analysis also found that the free charge carrier concentration of $PtSe_2$ is $N = 2.44 \times 10^{19}\ \mathrm{cm}^{-3}$. Apart from far-field FTIR, the near-field nano-FTIR was employed to measure the near-field spectra of the $PtSe_2$ and in good agreement with the calculated spectra from FD model.

5 Conclusion and Future Works

s-SNOM and nano-FTIR are novel techniques to break the diffraction limit to perform nanoscale measurements and are possible for nanoelectronics and nanophotonic studies. In this thesis, the basic working principle of s-SNOM and nano-FTIR are introduced. Also, necessary theories, particularly, the Fresnel's coefficients, complex dielectric constant and Finite Dipole (FD) Model are presented. They are necessary for predicting s-SNOM and nano-FTIR signal. Moreover, the Fresnel's coefficients and complex dielectric constant are necessary for calculating the dispersion relation of electromagnetic in-plane modes which is useful for the nano-optical study of $PtSe_2$ flakes in this work. Inspired by the conventional-FTIR spectra which show the dielectric nature of the $PtSe_2$ flakes, s-SNOM and nano-FTIR were employed to perform nano-optical study of the waveguide modes of $PtSe_2$ flakes. As confirmed by the theory, the dispersion relations of these modes can be extracted. This work paves the way for the use of s-SNOM to study nano-waveguides and future nanophotonic circuits.

For the future, nano-imaging should be performed on sample with different substrates such as Au and at other frequency such as the NIR range, so as to further confirm the analysis methodology in this work. Also, more precise measurement of the dielectric constant is required. Nano-FTIR microscopy may be a promising technique to achieve it [35-37]. It is also of importance if both the in-plane and out-of-plane dielectric constant can be obtained, and thus more precise dispersion relations can be calculated. Besides waveguide properties, s-SNOM and nano-FTIR may be capable of studying the layer dependent electronic properties of $PtSe_2$ and measuring the free carrier concentration of nano-electronics devices made up of $PtSe_2$ or other

2D materials. The dispersion analysis may allow the calculation of the group velocity $v_g = \frac{\mathrm{d}\omega}{\mathrm{d}k_p}$ and the density of states (DOS) of in-plane propagation modes of $PtSe_2$ or other materials.

Reference

[1] D. Dai, H.-J. Koo, M.-H. Whangbo, C. Soulard, X. Rocquefelte, and S. Jobic, "Trends in the structure and bonding in the layered platinum dioxide and dichalcogenides PtQ2 (Q= O, S, Se, Te)," *Journal of Solid State Chemistry,* vol. 173, no. 1, pp. 114-121, 2003.

[2] G. Guo and W. Liang, "The electronic structures of platinum dichalcogenides: PtS2, PtSe2 and PtTe2," *Journal of Physics C: Solid State Physics,* vol. 19, no. 7, p. 995, 1986.

[3] P. Miró, M. Audiffred, and T. Heine, "An atlas of two-dimensional materials," *Chemical Society Reviews,* vol. 43, no. 18, pp. 6537-6554, 2014.

[4] W. Zhang, Z. Huang, W. Zhang, and Y. Li, "Two-dimensional semiconductors with possible high room temperature mobility," *Nano Research,* journal article vol. 7, no. 12, pp. 1731-1737, December 01 2014, doi: 10.1007/s12274-014-0532-x.

[5] Y. Zhao *et al.*, "High-Electron-Mobility and Air-Stable 2D Layered PtSe2 FETs," *Advanced Materials,* vol. 29, no. 5, p. 1604230, 2017.

[6] W. Zhang, J. Qin, Z. Huang, and W. Zhang, "The mechanism of layer number and strain dependent bandgap of 2D crystal PtSe2," *J Appl Phys,* vol. 122, no. 20, p. 205701, 2017.

[7] A. Kandemir *et al.*, "Structural, electronic and phononic properties of PtSe2: from monolayer to bulk," *Semiconductor Science and Technology,* vol. 33, no. 8, p. 085002, 2018.

[8] Y. Wang *et al.*, "Monolayer PtSe2, a new semiconducting transition-metal-dichalcogenide, epitaxially grown by direct selenization of Pt," *Nano letters,* vol. 15, no. 6, pp. 4013-4018, 2015.

[9] M. O'Brien *et al.*, "Raman characterization of platinum diselenide thin films," *2D Materials,* vol. 3, no. 2, p. 021004, 2016.

[10] X. Yu *et al.*, "Atomically thin noble metal dichalcogenide: a broadband mid-infrared semiconductor," *Nature communications,* vol. 9, no. 1, p. 1545, 2018.

[11] H. Huang, S. Zhou, and W. Duan, "Type-II Dirac fermions in the PtSe 2 class of transition metal dichalcogenides," *Physical Review B,* vol. 94, no. 12, p. 121117, 2016.

[12] K. Zhang *et al.*, "Experimental evidence for type-II Dirac semimetal in PtSe 2," *Physical Review B,* vol. 96, no. 12, p. 125102, 2017.

[13] P. Li, L. Li, and X. C. Zeng, "Tuning the electronic properties of monolayer and bilayer PtSe 2 via strain engineering," *Journal of Materials Chemistry C,* vol. 4, no. 15, pp. 3106-3112, 2016.

[14] S. Deng, L. Li, and Y. Zhang, "Strain Modulated Electronic, Mechanical, and Optical Properties of the Monolayer PdS2, PdSe2, and PtSe2 for Tunable Devices," *ACS Applied Nano Materials,* vol. 1, no. 4, pp. 1932-1939, 2018.

[15] J. Du *et al.*, "Elastic, electronic and optical properties of the two-dimensional PtX2 (X= S, Se, and Te) monolayer," *Applied Surface Science,* vol. 435, pp. 476-482, 2018.

[16] Z. Wang, Q. Li, F. Besenbacher, and M. Dong, "Facile Synthesis of Single Crystal PtSe2 Nanosheets for Nanoscale Electronics," *Advanced Materials,* vol. 28, no. 46, pp. 10224-10229, 2016/12/01 2016, doi: 10.1002/adma.201602889.

[17] C. Yim *et al.*, "High-Performance Hybrid Electronic Devices from Layered PtSe2 Films Grown at Low Temperature," *ACS Nano,* vol. 10, no. 10, pp. 9550-9558, 2016/10/25 2016, doi: 10.1021/acsnano.6b04898.

[18] L. H. Zeng *et al.*, "Fast, self-driven, air-Stable, and broadband photodetector based on vertically aligned PtSe2/GaAs heterojunction," *Advanced Functional Materials,* vol. 28, no. 16, p. 1705970, 2018.

[19] W. Yao *et al.*, "Direct observation of spin-layer locking by local Rashba effect in monolayer semiconducting PtSe2 film," *Nature Communications,* vol. 8, no. 1, p. 14216, 2017/01/31 2017, doi: 10.1038/ncomms14216.

[20] F. Keilmann and R. Hillenbrand, "Near-field microscopy by elastic light scattering from a tip," *PHILOSOPHICAL TRANSACTIONS-ROYAL SOCIETY OF LONDON SERIES A MATHEMATICAL PHYSICAL AND ENGINEERING SCIENCES,* pp. 787-806, 2004.

[21] A. V. Zayats and D. Richards, *Nano-optics and near-field optical microscopy*. Artech House, 2009.

[22] J. M. Atkin, S. Berweger, A. C. Jones, and M. B. Raschke, "Nano-optical imaging and spectroscopy of order, phases, and domains in complex solids," *Advances in Physics,* vol. 61, no. 6, pp. 745-842, 2012, doi: 10.1080/00018732.2012.737982.

[23] B. Knoll and F. Keilmann, "Infrared conductivity mapping for nanoelectronics," *Applied Physics Letters,* vol. 77, no. 24, pp. 3980-3982, 2000, doi: 10.1063/1.1330756.

[24] A. J. Huber, D. Kazantsev, F. Keilmann, J. Wittborn, and R. Hillenbrand, "Simultaneous IR Material Recognition and Conductivity Mapping by Nanoscale Near-Field Microscopy," *Advanced Materials,* vol. 19, no. 17, pp. 2209-2212, 2007, doi: 10.1002/adma.200602303.

[25] A. J. Huber, F. Keilmann, J. Wittborn, J. Aizpurua, and R. Hillenbrand, "Terahertz near-field nanoscopy of mobile carriers in single semiconductor nanodevices," *Nano letters,* vol. 8, no. 11, pp. 3766-3770, 2008.

[26] B. Knoll and F. Keilmann, "Near-field probing of vibrational absorption for chemical microscopy," *Nature,* vol. 399, no. 6732, p. 134, 1999.

[27] T. Taubner, R. Hillenbrand, and F. Keilmann, "Nanoscale polymer recognition by spectral signature in scattering infrared near-field microscopy," *Applied Physics Letters,* vol. 85, no. 21, pp. 5064-5066, 2004, doi: 10.1063/1.1827334.

[28] M. B. Raschke, L. Molina, T. Elsaesser, D. H. Kim, W. Knoll, and K. Hinrichs, "Apertureless Near-Field Vibrational Imaging of Block-Copolymer Nanostructures with Ultrahigh Spatial Resolution," *ChemPhysChem,* vol. 6, no. 10, pp. 2197-2203, 2005.

[29] N. Ocelic and R. Hillenbrand, "Subwavelength-scale tailoring of surface phonon polaritons by focused ion-beam implantation," *Nature materials,* vol. 3, no. 9, p. 606, 2004.

[30] A. M. Gigler, A. J. Huber, M. Bauer, A. Ziegler, R. Hillenbrand, and R. W. Stark, "Nanoscale residual stress-field mapping around nanoindents in SiC by IR s-SNOM and confocal Raman microscopy," *Optics Express,* vol. 17, no. 25, pp. 22351-22357, 2009.

[31] A. Huber, A. Ziegler, T. Köck, and R. Hillenbrand, "Infrared nanoscopy of strained semiconductors," *Nature nanotechnology,* vol. 4, no. 3, p. 153, 2009.

[32] M. M. Qazilbash *et al.*, "Mott transition in VO2 revealed by infrared spectroscopy and nano-imaging," *Science,* vol. 318, no. 5857, pp. 1750-1753, 2007.

[33] M. Qazilbash *et al.*, "Infrared spectroscopy and nano-imaging of the insulator-to-metal transition in vanadium dioxide," *Physical Review B,* vol. 79, no. 7, p. 075107, 2009.

[34] F. Huth, A. Govyadinov, S. Amarie, W. Nuansing, F. Keilmann, and R. Hillenbrand, "Nano-FTIR absorption spectroscopy of molecular fingerprints at 20 nm spatial resolution," *Nano letters,* vol. 12, no. 8, pp. 3973-3978, 2012.

[35] A. A. Govyadinov, I. Amenabar, F. Huth, P. S. Carney, and R. Hillenbrand, "Quantitative measurement of local infrared absorption and dielectric function with tip-enhanced near-field microscopy," *The journal of physical chemistry letters,* vol. 4, no. 9, pp. 1526-1531, 2013.

[36] A. A. Govyadinov, S. Mastel, F. Golmar, A. Chuvilin, P. S. Carney, and R. Hillenbrand, "Recovery of permittivity and depth from near-field data as a step toward infrared nanotomography," *Acs Nano,* vol. 8, no. 7, pp. 6911-6921, 2014.

[37] A. S. McLeod *et al.*, "Model for quantitative tip-enhanced spectroscopy and the extraction of nanoscale-resolved optical constants," *Physical Review B,* vol. 90, no. 8, p. 085136, 2014.

[38] F. Xia, H. Wang, D. Xiao, M. Dubey, and A. Ramasubramaniam, "Two-dimensional material nanophotonics," *Nature Photonics,* vol. 8, no. 12, pp. 899-907, 2014, doi: 10.1038/nphoton.2014.271.

[39] D. N. Basov, M. M. Fogler, and F. J. Garcia de Abajo, "Polaritons in van der Waals materials," *Science,* vol. 354, no. 6309, Oct 14 2016, doi: 10.1126/science.aag1992.

[40] T. Low *et al.*, "Polaritons in layered two-dimensional materials," *Nat Mater,* vol. 16, no. 2, pp. 182-194, Feb 2017, doi: 10.1038/nmat4792.

[41] J. Chen *et al.*, "Optical nano-imaging of gate-tunable graphene plasmons," *Nature,* vol. 487, no. 7405, p. 77, 2012.

[42] Z. Fei *et al.*, "Gate-tuning of graphene plasmons revealed by infrared nano-imaging," *Nature,* vol. 487, no. 7405, p. 82, 2012.

[43] S. Dai *et al.*, "Tunable phonon polaritons in atomically thin van der Waals crystals of boron nitride," *Science,* vol. 343, no. 6175, pp. 1125-1129, 2014.

[44] E. Yoxall *et al.*, "Direct observation of ultraslow hyperbolic polariton propagation with negative phase velocity," *Nature Photonics,* vol. 9, no. 10, p. 674, 2015.

[45] W. Ma *et al.*, "In-plane anisotropic and ultra-low-loss polaritons in a natural van der Waals crystal," *Nature,* vol. 562, no. 7728, p. 557, 2018.

[46] Z. Zheng *et al.*, "Highly Confined and Tunable Hyperbolic Phonon Polaritons in Van Der Waals Semiconducting Transition Metal Oxides," *Advanced Materials,* vol. 30, no. 13, p. 1705318, 2018.

[47] M. A. Huber *et al.*, "Femtosecond photo-switching of interface polaritons in black phosphorus heterostructures," *Nature nanotechnology,* vol. 12, no. 3, p. 207, 2017.

[48] Z. Fei *et al.*, "Nano-optical imaging of WSe2 waveguide modes revealing light-exciton interactions," *Physical Review B,* vol. 94, no. 8, p. 081402, 2016.

[49] M. Mrejen, L. Yadgarov, A. Levanon, and H. Suchowski, "Transient exciton-polariton dynamics in WSe2 by ultrafast near-field imaging," *Science advances,* vol. 5, no. 2, p. eaat9618, 2019.

[50] F. Hu *et al.*, "Imaging exciton–polariton transport in MoSe2 waveguides," *Nature Photonics,* vol. 11, no. 6, p. 356, 2017.

[51] D. Hu *et al.*, "Probing optical anisotropy of nanometer-thin van der waals microcrystals by near-field imaging," *Nature Communications,* vol. 8, no. 1, p. 1471, 2017.

[52] D. Hu, K. Chen, X. Chen, X. Guo, M. Liu, and Q. Dai, "Tunable Modal Birefringence in a Low-Loss Van Der Waals Waveguide," *Advanced Materials,* p. 1807788, 2019.

[53] Z. Fei *et al.*, "Infrared nanoscopy of Dirac plasmons at the graphene–SiO2 interface," *Nano letters,* vol. 11, no. 11, pp. 4701-4705, 2011.

[54] P. Patoka *et al.*, "Nanoscale plasmonic phenomena in CVD-grown MoS 2 monolayer revealed by ultra-broadband synchrotron radiation based nano-FTIR spectroscopy and near-field microscopy," *Optics express,* vol. 24, no. 2, pp. 1154-1164, 2016.

[55] S. N. Neal *et al.*, "Near-field infrared spectroscopy of monolayer MnPS3," *Physical Review B,* vol. 100, no. 7, p. 075428, 08/22/ 2019, doi: 10.1103/PhysRevB.100.075428.

[56] E. L. Wolf, *Nanophysics and Nanotechnology: An Introduction to Modern Concepts in Nanoscience*. Wiley, 2015.

[57] C. Girard and A. Dereux, "Near-field optics theories," *Reports on Progress in Physics,* vol. 59, no. 5, p. 657, 1996.

[58] J.-J. Greffet and R. Carminati, "Image formation in near-field optics," *Progress in surface science,* vol. 56, no. 3, pp. 133-237, 1997.

[59] F. Zenhausern, Y. Martin, and H. Wickramasinghe, "Scanning interferometric apertureless microscopy: optical imaging at 10 angstrom resolution," *Science,* vol. 269, no. 5227, pp. 1083-1085, 1995.

[60] D. J. Griffiths, "Introduction to electrodynamics," ed: AAPT, 2005.

[61] J. D. Jackson, *Classical electrodynamics*. John Wiley & Sons, 2012.

[62] J. C. Maxwell, "II. A dynamical theory of the electromagnetic field," *Proceedings of the Royal Society of London,* no. 13, pp. 531-536, 1864.

[63] J. C. Maxwell, "VIII. A dynamical theory of the electromagnetic field," *Philosophical transactions of the Royal Society of London,* no. 155, pp. 459-512, 1865.

[64] M. Fox, *Optical properties of solids*. AAPT, 2002.

[65] C. F. Bohren and D. R. Huffman, *Absorption and scattering of light by small particles*. John Wiley & Sons, 1983.

[66] P. Drude, "Zur elektronentheorie der metalle," *Annalen der physik,* vol. 306, no. 3, pp. 566-613, 1900.

[67] N. W. Ashcroft and N. D. Mermin, *Solid state physics*. Orlando: Saunders college, 1976.

[68] D. A. Miller, *Quantum mechanics for scientists and engineers*. Cambridge University Press, 2008.

[69] L. Novotny and B. Hecht, *Principles of nano-optics*. Cambridge university press, 2012.

[70] H. Ehrenreich and H. Philipp, "Optical properties of Ag and Cu," *Physical Review,* vol. 128, no. 4, p. 1622, 1962.

[71] H. Ehrenreich, H. Philipp, and B. Segall, "Optical properties of aluminum," *Physical Review,* vol. 132, no. 5, p. 1918, 1963.

[72] A. Vial, A.-S. Grimault, D. Macías, D. Barchiesi, and M. L. de La Chapelle, "Improved analytical fit of gold dispersion: Application to the modeling of extinction spectra with a finite-difference time-domain method," *Physical Review B,* vol. 71, no. 8, p. 085416, 2005.

[73] H. Kramers, "Estratto dagli Atti del Congresso Internazionale di Fisici Como," *Nicolo Zonichello, Bologna,* 1927.

[74] R. d. Kronig, "Algemeene theorie der diëlectrische en magnetische verliezen," *Ned. T. Natuurk,* vol. 9, p. 402, 1942.

[75] J. S. Toll, "Causality and the dispersion relation: logical foundations," *Physical review,* vol. 104, no. 6, p. 1760, 1956.

[76] J. Renger, S. Grafström, L. M. Eng, and R. Hillenbrand, "Resonant light scattering by near-field-induced phonon polaritons," *Physical Review B,* vol. 71, no. 7, 2005, doi: 10.1103/PhysRevB.71.075410.

[77] A. Cvitkovic, N. Ocelic, and R. Hillenbrand, "Analytical model for quantitative prediction of material contrasts in scattering-type near-field optical microscopy," *Optics express,* vol. 15, no. 14, pp. 8550-8565, 2007. [Online]. Available: https://www.osapublishing.org/oe/abstract.cfm?uri=oe-15-14-8550.

[78] P. A. D. Gonçalves and N. M. Peres, *An introduction to graphene plasmonics*. World Scientific, 2016.

[79] M. J. Adams, *An introduction to optical waveguides*. Wiley New York, 1981.

[80] D. Marcuse, *Theory of dielectric optical waveguides*. Elsevier, 1981.

[81] V. E. Babicheva, S. Gamage, L. Zhen, S. B. Cronin, V. S. Yakovlev, and Y. Abate, "Near-field Surface Waves in Few-Layer MoS2," *ACS Photonics,* vol. 5, no. 6, pp. 2106-2112, 2018.

[82] J. Lekner, *Theory of reflection*. Springer, 1987.

[83] E. Hecht, *Optics*, 3rd ed.. ed. Reading, Mass.: Addison-Wesley, 1998.

[84] J. Lekner, "Reflection and refraction by uniaxial crystals," *Journal of Physics: Condensed Matter,* vol. 3, no. 32, p. 6121, 1991.

[85] T. Zhan, X. Shi, Y. Dai, X. Liu, and J. Zi, "Transfer matrix method for optics in graphene layers," *Journal of Physics: Condensed Matter,* vol. 25, no. 21, p. 215301, 2013.

[86] S. A. Maier, *Plasmonics: fundamentals and applications*. Springer Science & Business Media, 2007.

[87] A. V. Zayats, I. I. Smolyaninov, and A. A. Maradudin, "Nano-optics of surface plasmon polaritons," *Physics reports,* vol. 408, no. 3-4, pp. 131-314, 2005.

[88] L. M. Zhang *et al.*, "Near-field spectroscopy of silicon dioxide thin films," *Physical Review B,* vol. 85, no. 7, p. 075419, 2012.

[89] B. Prade, J. Vinet, and A. Mysyrowicz, "Guided optical waves in planar heterostructures with negative dielectric constant," *Physical Review B,* vol. 44, no. 24, p. 13556, 1991.

[90] E. Synge, "A suggested method for extending microscopic resolution into the ultra-microscopic region," *The London, Edinburgh, and Dublin Philosophical Magazine and Journal of Science,* vol. 6, no. 35, pp. 356-362, 1928.

[91] L. Novotny, "The history of near-field optics," *Progress in optics,* vol. 50, p. 137, 2007.

[92] D. W. Pohl, W. Denk, and M. Lanz, "Optical stethoscopy: Image recording with resolution λ/20," *Applied physics letters,* vol. 44, no. 7, pp. 651-653, 1984.

[93] E. Betzig, J. Trautman, T. Harris, J. Weiner, and R. Kostelak, "Breaking the diffraction barrier: optical microscopy on a nanometric scale," *Science,* vol. 251, no. 5000, pp. 1468-1470, 1991.

[94] A. Lahrech, R. Bachelot, P. Gleyzes, and A. Boccara, "Infrared-reflection-mode near-field microscopy using an apertureless probe with a resolution of λ/600," *Optics letters,* vol. 21, no. 17, pp. 1315-1317, 1996.

[95] B. Knoll and F. Keilmann, "Mid-infrared scanning near-field optical microscope resolves 30 nm," *Journal of microscopy,* vol. 194, no. 2-3, pp. 512-515, 1999.

[96] B. Knoll and F. Keilmann, "Enhanced dielectric contrast in scattering-type scanning near-field optical microscopy," *Optics communications,* vol. 182, no. 4-6, pp. 321-328, 2000.

[97] R. Hillenbrand and F. Keilmann, "Complex optical constants on a subwavelength scale," *Physical Review Letters,* vol. 85, no. 14, p. 3029, 2000.

[98] L. Novotny and S. J. Stranick, "Near-field optical microscopy and spectroscopy with pointed probes," *Annu. Rev. Phys. Chem.,* vol. 57, pp. 303-331, 2006.

[99] R. Esteban, R. Vogelgesang, and K. Kern, "Tip-substrate interaction in optical near-field microscopy," *Physical Review B,* vol. 75, no. 19, p. 195410, 2007.

[100] J. L. Bohn, D. J. Nesbitt, and A. Gallagher, "Field enhancement in apertureless near-field scanning optical microscopy," *JOSA A,* vol. 18, no. 12, pp. 2998-3006, 2001.

[101] M. Brehm, A. Schliesser, F. Čajko, I. Tsukerman, and F. Keilmann, "Antenna-mediated back-scattering efficiency in infrared near-field microscopy," *Optics express,* vol. 16, no. 15, pp. 11203-11215, 2008.

[102] R. Esteban, R. Vogelgesang, and K. Kern, "Full simulations of the apertureless scanning near field optical microscopy signal: achievable resolution and contrast," *Optics express,* vol. 17, no. 4, pp. 2518-2529, 2009.

[103] P. Aravind and H. Metiu, "The effects of the interaction between resonances in the electromagnetic response of a sphere-plane structure; applications to surface enhanced spectroscopy," *Surface science,* vol. 124, no. 2-3, pp. 506-528, 1983.

[104] J. Wessel, "Surface-enhanced optical microscopy," *JOSA B,* vol. 2, no. 9, pp. 1538-1541, 1985.

[105] A. Hartschuh, E. J. Sánchez, X. S. Xie, and L. Novotny, "High-resolution near-field Raman microscopy of single-walled carbon nanotubes," *Physical Review Letters,* vol. 90, no. 9, p. 095503, 2003.

[106] N. Anderson, P. Anger, A. Hartschuh, and L. Novotny, "Subsurface Raman imaging with nanoscale resolution," *Nano letters,* vol. 6, no. 4, pp. 744-749, 2006.

[107] T.-a. Yano, Y. Inouye, and S. Kawata, "Nanoscale uniaxial pressure effect of a carbon nanotube bundle on tip-enhanced near-field Raman spectra," *Nano letters,* vol. 6, no. 6, pp. 1269-1273, 2006.

[108] B.-S. Yeo, J. Stadler, T. Schmid, R. Zenobi, and W. Zhang, "Tip-enhanced Raman Spectroscopy–Its status, challenges and future directions," *Chemical Physics Letters,* vol. 472, no. 1-3, pp. 1-13, 2009.

[109] J. Porto, R. Carminati, and J.-J. Greffet, "Theory of electromagnetic field imaging and spectroscopy in scanning near-field optical microscopy," *J Appl Phys,* vol. 88, no. 8, pp. 4845-4850, 2000.

[110] J. Porto, P. Johansson, S. Apell, and T. Lopez-Rios, "Resonance shift effects in apertureless scanning near-field optical microscopy," *Physical Review B,* vol. 67, no. 8, p. 085409, 2003.

[111] G. W. Ford and W. H. Weber, "Electromagnetic interactions of molecules with metal surfaces," *Physics Reports,* vol. 113, no. 4, pp. 195-287, 1984.

[112] J. Koglin, U. C. Fischer, and H. Fuchs, "Material contrast in scanning near-field optical microscopy at 1–10 nm resolution," *Physical Review B,* vol. 55, no. 12, p. 7977, 1997.

[113] R. Ruppin, "Infrared active modes of dielectric crystallites on a substrate," *Surface Science,* vol. 58, no. 2, pp. 550-556, 1976.

[114] A. Huber, N. Ocelic, T. Taubner, and R. Hillenbrand, "Nanoscale Resolved Infrared Probing of Crystal Structure and of Plasmon− Phonon Coupling," *Nano letters,* vol. 6, no. 4, pp. 774-778, 2006.

[115] S. Schneider *et al.*, "Impact of optical in-plane anisotropy on near-field phonon polariton spectroscopy," *Applied physics letters,* vol. 90, no. 14, p. 143101, 2007.

[116] M. B. Raschke and C. Lienau, "Apertureless near-field optical microscopy: Tip–sample coupling in elastic light scattering," *Applied Physics Letters,* vol. 83, no. 24, pp. 5089-5091, 2003.

[117] S. Amarie and F. Keilmann, "Broadband-infrared assessment of phonon resonance in scattering-type near-field microscopy," *Physical Review B,* vol. 83, no. 4, p. 045404, 2011.

[118] S. Kehr *et al.*, "Anisotropy contrast in phonon-enhanced apertureless near-field microscopy using a free-electron laser," *Physical review letters,* vol. 100, no. 25, p. 256403, 2008.

[119] R. Hillenbrand, T. Taubner, and F. Keilmann, "Phonon-enhanced light–matter interaction at the nanometre scale," *Nature,* vol. 418, no. 6894, p. 159, 2002.

[120] S. Schneider, S. Grafström, and L. Eng, "Scattering near-field optical microscopy of optically anisotropic systems," *Physical Review B,* vol. 71, no. 11, p. 115418, 2005.

[121] J. Aizpurua, T. Taubner, F. J. G. de Abajo, M. Brehm, and R. Hillenbrand, "Substrate-enhanced infrared near-field spectroscopy," *Optics express,* vol. 16, no. 3, pp. 1529-1545, 2008.

[122] P. Johansson, S. P. Apell, and D. R. Penn, "Theory of a magnetic microscope with nanometer resolution," *Physical Review B,* vol. 64, no. 5, p. 054411, 2001.

[123] B. Hauer, A. P. Engelhardt, and T. Taubner, "Quasi-analytical model for scattering infrared near-field microscopy on layered systems," *Optics express,* vol. 20, no. 12, pp. 13173-13188, 2012.

[124] J. Stiegler *et al.*, "Nanoscale free-carrier profiling of individual semiconductor nanowires by infrared near-field nanoscopy," *Nano letters,* vol. 10, no. 4, pp. 1387-1392, 2010.

[125] J. Walford *et al.*, "Influence of tip modulation on image formation in scanning near-field optical microscopy," *J Appl Phys,* vol. 89, no. 9, pp. 5159-5169, 2001.

[126] P. G. Gucciardi, G. Bachelier, and M. Allegrini, "Far-field background suppression in tip-modulated apertureless near-field optical microscopy," *J Appl Phys,* vol. 99, no. 12, p. 124309, 2006.

[127] R. Hillenbrand, B. Knoll, and F. Keilmann, "Pure optical contrast in scattering-type scanning near-field microscopy," *Journal of microscopy,* vol. 202, no. 1, pp. 77-83, 2001.

[128] L. Stebounova, B. B. Akhremitchev, and G. C. Walker, "Enhancement of the weak scattered signal in apertureless near-field scanning infrared microscopy," *Review of scientific instruments,* vol. 74, no. 8, pp. 3670-3674, 2003.

[129] T. Taubner, R. Hillenbrand, and F. Keilmann, "Performance of visible and mid-infrared scattering-type near-field optical microscopes," *Journal of microscopy,* vol. 210, no. 3, pp. 311-314, 2003.

[130] D. Roy, S. Leong, and M. Welland, "Dielectric contrast imaging using apertureless scanning near-field optical microscopy in the reflection mode," *J. Korean Phys. Soc,* vol. 47, p. 140, 2005.

[131] N. Ocelic, A. Huber, and R. Hillenbrand, "Pseudoheterodyne detection for background-free near-field spectroscopy," *Applied Physics Letters,* vol. 89, no. 10, 2006, doi: 10.1063/1.2348781.

[132] F. Huth, "Nano-FTIR: Nanoscale Infrared Near-field Spectroscopy," PhD Thesis, UNIVERSIDAD DEL PAIS VASCO, 2015.

[133] S. Amarie, T. Ganz, and F. Keilmann, "Mid-infrared near-field spectroscopy," *Optics Express,* vol. 17, no. 24, pp. 21794-21801, 2009.

[134] K. F. Mak and J. Shan, "Photonics and optoelectronics of 2D semiconductor transition metal dichalcogenides," *Nature Photonics,* vol. 10, no. 4, pp. 216-226, 2016/04/01 2016, doi: 10.1038/nphoton.2015.282.

[135] P. Miró, M. Ghorbani-Asl, and T. Heine, "Two dimensional materials beyond MoS2: noble-transition-metal dichalcogenides," *Angewandte Chemie International Edition,* vol. 53, no. 11, pp. 3015-3018, 2014.

[136] S. Furuseth, K. Selte, and A. Kjekshus, "Redetermined Crystal Structures of NiTe2 PdTe2 PtS2 PtSe2 and PtTe2," vol. 19, ed: MUNKSGAARD INT PUBL LTD 35 NORRE SOGADE, PO BOX 2148, DK-1016 COPENHAGEN …, 1965, pp. 257-&.

[137] R. A. B. Villaos *et al.*, "Thickness dependent electronic properties of Pt dichalcogenides," *npj 2D Materials and Applications,* vol. 3, no. 1, p. 2, 2019.

[138] G. Kliche, "Far-infrared and X-ray investigations of the mixed platinum dichalcogenides PtS2− xSex, PtSe2− xTex, and PtS2− xTex," *Journal of Solid State Chemistry,* vol. 56, no. 1, pp. 26-31, 1985.

[139] J. Xiong *et al.*, "Evidence for the chiral anomaly in the Dirac semimetal Na3Bi," *Science,* vol. 350, no. 6259, pp. 413-416, 2015.

[140] H. Li *et al.*, "Negative magnetoresistance in Dirac semimetal Cd3As2," *Nature Communications,* vol. 7, no. 1, p. 10301, 2016/01/08 2016, doi: 10.1038/ncomms10301.

[141] Q. Wang *et al.*, "Ultrafast Broadband Photodetectors Based on Three-Dimensional Dirac Semimetal Cd3As2," *Nano Letters,* vol. 17, no. 2, pp. 834-841, 2017/02/08 2017, doi: 10.1021/acs.nanolett.6b04084.

[142] J. Kim *et al.*, "Observation of tunable band gap and anisotropic Dirac semimetal state in black phosphorus," *Science,* vol. 349, no. 6249, pp. 723-726, 2015.

[143] M. A. Ordal, R. J. Bell, R. W. Alexander, L. L. Long, and M. R. Querry, "Optical properties of fourteen metals in the infrared and far infrared: Al, co, cu, au, fe, pb, mo, ni, pd, pt, ag, ti, v, and w," *Applied optics,* vol. 24, no. 24, pp. 4493-4499, 1985.

[144] M. Born and E. Wolf, *Principles of Optics: Electromagnetic Theory of Propagation, Interference and Diffraction of Light*, 7 ed. Cambridge: Cambridge University Press, 1999.

[145] H. Yang *et al.*, "Quantum oscillations in the type-II Dirac semi-metal candidate PtSe2," *New Journal of Physics,* vol. 20, no. 4, p. 043008, 2018.

[146] M. N. Gjerding, R. Petersen, T. G. Pedersen, N. A. Mortensen, and K. S. Thygesen, "Layered van der Waals crystals with hyperbolic light dispersion," *Nature communications,* vol. 8, no. 1, p. 320, 2017.

[147] T. Christensen, *From classical to quantum plasmonics in three and two dimensions*. Springer, 2017.

[148] C. Kittel, *Introduction to solid state physics*. Wiley New York, 2005.

[149] D. Y. Smith, "Dispersion relations for complex reflectivities," *JOSA,* vol. 67, no. 4, pp. 570-571, 1977.

[150] V. Lucarini, J. J. Saarinen, K.-E. Peiponen, and E. M. Vartiainen, *Kramers-Kronig relations in optical materials research*. Springer Science & Business Media, 2005.

[151] C. Sheppard and F. Aguilar, "Fresnel coefficients for weak reflection, and the scattering potential for three-dimensional imaging," *Optics communications,* vol. 162, no. 4-6, pp. 182-186, 1999.

[152] K. Okamoto, *Fundamentals of optical waveguides*. Academic press, 2006.

[153] C. Yeh and F. I. Shimabukuro, *The essence of dielectric waveguides*. Springer, 2008.

[154] A. Beal and H. Hughes, "Kramers-Kronig analysis of the reflectivity spectra of 2H-MoS2, 2H-MoSe2 and 2H-MoTe2," *Journal of Physics C: Solid State Physics,* vol. 12, no. 5, p. 881, 1979.

Appendix A: Demodulated Signal with Direct Detection

The backscattered field E_s after modulating the distance between the tip and sample surface with frequency Ω is:

$$E_s = E_i \sum_{n=0}^{\infty} \sigma_n e^{in\Omega t},$$

where $\sigma_n = \sigma_{nf,n} + \sigma_{bg,n}$.

The detected signal U is proportional to the intensity I of the field E_s:

$$U \propto E_s {E_s}^* = {E_i}^2 \left(\sum_{n=0}^{\infty} \sigma_n e^{in\Omega t} \right) \left(\sum_{n=0}^{\infty} {\sigma_n}^* e^{-in\Omega t} \right) \tag{A. 1}$$

$$U \propto {E_i}^2 \begin{bmatrix} (\sigma_0{\sigma_0}^* + \sigma_1{\sigma_1}^* + \sigma_2{\sigma_2}^* + \cdots) \\ +(\sigma_1{\sigma_0}^* + \sigma_2{\sigma_1}^* + \sigma_3{\sigma_2}^* + \cdots)e^{i\Omega t} + ({\sigma_1}^*\sigma_0 + {\sigma_2}^*\sigma_1 + {\sigma_3}^*\sigma_2 + \cdots)e^{-i\Omega t} \\ +(\sigma_2{\sigma_0}^* + \sigma_3{\sigma_1}^* + \sigma_4{\sigma_2}^* + \cdots)e^{i2\Omega t} + ({\sigma_2}^*\sigma_0 + {\sigma_3}^*\sigma_1 + {\sigma_4}^*\sigma_2 + \cdots)e^{-i2\Omega t} \\ +\cdots \end{bmatrix}$$

$$= {E_i}^2 \begin{bmatrix} \sum_{j=0}^{\infty} \sigma_j {\sigma_j}^* \\ +[(\sigma_1{\sigma_0}^* + {\sigma_1}^*\sigma_0) + (\sigma_2{\sigma_1}^* + {\sigma_2}^*\sigma_1) + (\sigma_3{\sigma_2}^* + {\sigma_3}^*\sigma_2) + \cdots]\cos\Omega t \\ +i[(\sigma_1{\sigma_0}^* - {\sigma_1}^*\sigma_0) + (\sigma_2{\sigma_1}^* - {\sigma_2}^*\sigma_1) + (\sigma_3{\sigma_2}^* - {\sigma_3}^*\sigma_2) + \cdots]\sin\Omega t \\ +[(\sigma_2{\sigma_0}^* + {\sigma_2}^*\sigma_0) + (\sigma_3{\sigma_1}^* + {\sigma_3}^*\sigma_1) + (\sigma_4{\sigma_2}^* + {\sigma_4}^*\sigma_2) + \cdots]\cos 2\Omega t \\ +i[(\sigma_2{\sigma_0}^* - {\sigma_2}^*\sigma_0) + (\sigma_3{\sigma_1}^* - {\sigma_3}^*\sigma_1) + (\sigma_4{\sigma_2}^* - {\sigma_4}^*\sigma_2) + \cdots]\sin 2\Omega t \\ +\cdots \end{bmatrix}$$

$$= {E_i}^2 \begin{bmatrix} \sum_{j=0}^{\infty} \sigma_j {\sigma_j}^* \\ +\sum_{j=1}^{\infty} (\sigma_j {\sigma_{j-1}}^* + {\sigma_j}^*\sigma_{j-1})\cos\Omega t + i\sum_{j=1}^{\infty} (\sigma_j {\sigma_{j-1}}^* - {\sigma_j}^*\sigma_{j-1})\sin\Omega t \\ +\sum_{j=2}^{\infty} (\sigma_j {\sigma_{j-2}}^* + {\sigma_j}^*\sigma_{j-2})\cos 2\Omega t + i\sum_{j=2}^{\infty} (\sigma_j {\sigma_{j-2}}^* - {\sigma_j}^*\sigma_{j-2})\sin 2\Omega t \\ +\cdots \end{bmatrix}$$

$$= {E_i}^2 \left\{ \begin{array}{c} \sum_{j=0}^{\infty} \sigma_j {\sigma_j}^* \\ \sum_{n=1}^{\infty} \left[\sum_{j=n}^{\infty} \left(\sigma_j {\sigma_{j-n}}^* + {\sigma_j}^* \sigma_{j-n} \right) \cos \mathrm{n}\Omega t + i \sum_{j=n}^{\infty} \left(\sigma_j {\sigma_{j-n}}^* - {\sigma_j}^* \sigma_{j-n} \right) \sin \mathrm{n}\Omega t \right] \\ + \cdots \end{array} \right\}$$

For $\mathrm{n} \geq 1$, the n^{th} order demodulated signal U_n is the cosine component:

$$U_n \propto {E_i}^2 \sum_{j=n}^{\infty} \left(\sigma_j {\sigma_{j-n}}^* + {\sigma_j}^* \sigma_{j-n} \right)$$

$\because \sigma_0 \ggg \sigma_1 > \sigma_2 > \cdots$

$\therefore U_n \propto {E_i}^2 (\sigma_n {\sigma_0}^* + {\sigma_n}^* \sigma_0)$

$$= {E_i}^2 \left[\left(\sigma_{nf,n} + \sigma_{b,n} \right) \left({\sigma_{nf,0}}^* + {\sigma_{b,0}}^* \right) + \left({\sigma_{nf,n}}^* + {\sigma_{b,n}}^* \right) \left(\sigma_{nf,0} + \sigma_{b,0} \right) \right]$$

$\because {\sigma_{b,0}}^* \gg {\sigma_{nf,0}}^*$

$\therefore U_n \propto {E_i}^2 \left[\left(\sigma_{nf,n} + \sigma_{b,n} \right) \left({\sigma_{b,0}}^* \right) + \left({\sigma_{nf,n}}^* + {\sigma_{b,n}}^* \right) \left(\sigma_{b,0} \right) \right]$

Assuming $\sigma_{nf,n} \gg \sigma_{b,0}$ for high n,

$$U_n \propto {E_i}^2 \left(\sigma_{nf,n} {\sigma_{b,0}}^* + {\sigma_{nf,n}}^* \sigma_{b,0} \right)$$

$$= {E_i}^2 \cdot 2\mathrm{Re}\left(\sigma_{nf,n} {\sigma_{b,0}}^* \right)$$

$$= 2{E_i}^2 \mathrm{Re}\left[s_{nf,n} {s_{b,0}}^* e^{i(\phi_{nf,n} - \phi_{b,0})} \right]$$

$$= 2{E_{inc}}^2 s_{nf,n} {s_{b,0}}^* \cos\left(\phi_{nf,n} - \phi_{b,0} \right)$$

$$\therefore U_n \propto s_{nf,n} {s_{b,0}}^* \cos\left(\phi_{nf,n} - \phi_{b,0} \right) \quad \text{(A. 2)}$$

Appendix B: Demodulated Signal with Pseudo-heterodyne detection

The detected signal is proportional to the intensity of the combination of backscattered and reference field:

$$U \propto \left(E_s + E_{ref}\right)\left({E_s}^* + {E_{ref}}^*\right) \tag{B. 1}$$

The reference mirror is vibrating with frequency M, and thus modulating the phase of the reference wave:

$$E_{ref} = s_{ref} e^{i\gamma \sin(Mt) + i\psi_{ref}}.$$

Expressing in Fourier series, one can have

$$E_{ref} = \sum_{m=-\infty}^{\infty} \rho_m e^{imMt}, where\ \rho_m = s_{ref} J_m(\gamma) e^{i\psi_{ref} + i\frac{m\pi}{2}}\ and\ m\ is\ integers$$

From Equation (B. 1), we obtain:

$$U \propto E_s {E_s}^* + E_s {E_{ref}}^* + {E_s}^* E_{ref} + E_{ref} {E_{ref}}^* \tag{B. 2}$$

The first term in Equation (B. 2) is just the same as Equation (A. 1). In other word, if we demodulate the signal in order n, there is still background contribution. The last term in Equation (B. 2) is useless because if involves no backscattered field. Therefore, the focus is the second plus the third term, $E_s {E_{ref}}^* + {E_s}^* E_{ref}$.

$$E_s {E_{ref}}^* = E_i \left(\sum_{n=0}^{\infty} \sigma_n e^{in\Omega t}\right)\left(\sum_{m=-\infty}^{\infty} \rho_m e^{imMt}\right)$$

$$\propto \begin{pmatrix} \sigma_0 {\rho_1}^* e^{-iMt} + \sigma_0 {\rho_2}^* e^{-i2Mt} + \cdots \\ +\sigma_0 {\rho_{-1}}^* e^{iMt} + \sigma_0 {\rho_{-2}}^* e^{i2Mt} + \cdots \end{pmatrix} + \begin{bmatrix} \sigma_1 {\rho_1}^* e^{i(\Omega - M)t} + \sigma_1 {\rho_2}^* e^{-i(\Omega - 2M)t} + \cdots \\ +\sigma_1 {\rho_{-1}}^* e^{i(\Omega - M)t} + \sigma_1 {\rho_{-2}}^* e^{i(\Omega - 2M)t} + \cdots \end{bmatrix} + \cdots$$
$$+ \begin{bmatrix} \sigma_n {\rho_1}^* e^{i(n\Omega - M)t} + \sigma_n {\rho_2}^* e^{-i(n\Omega - 2M)t} + \cdots \\ +\sigma_n {\rho_{-1}}^* e^{i(n\Omega - M)t} + \sigma_n {\rho_{-2}}^* e^{i(n\Omega - 2M)t} + \cdots \end{bmatrix} + \cdots$$

$$= \sum_{m=-\infty}^{\infty} \sigma_0 {\rho_m}^* e^{-imMt} + \sum_{m=-\infty}^{\infty} \sigma_1 {\rho_m}^* e^{i(\Omega - mM)t} + \sum_{m=-\infty}^{\infty} \sigma_2 {\rho_m}^* e^{i(2\Omega - mM)t} + \cdots$$
$$+ \sum_{m=-\infty}^{\infty} \sigma_n {\rho_m}^* e^{i(n\Omega - mM)t} + \cdots$$

$$E_s{E_{ref}}^* + {E_s}^* E_{ref} \propto \begin{pmatrix} \sum_{m=-\infty}^{\infty} \sigma_0 {\rho_m}^* e^{-imMt} + \sum_{m=-\infty}^{\infty} {\sigma_0}^* \rho_m e^{imMt} \\ + \sum_{m=-\infty}^{\infty} \sigma_1 {\rho_m}^* e^{i(\Omega - mM)t} + \sum_{m=-\infty}^{\infty} {\sigma_1}^* \rho_m e^{-i(\Omega - mM)t} \\ + \cdots \\ + \sum_{m=-\infty}^{\infty} \sigma_n {\rho_m}^* e^{i(n\Omega - mM)t} + \sum_{m=-\infty}^{\infty} {\sigma_n}^* \rho_m e^{-i(n\Omega - mM)t} \\ + \cdots \end{pmatrix}$$

$$= \begin{pmatrix} \sum_{m=-\infty}^{\infty} (\sigma_0 {\rho_m}^* + {\sigma_0}^* \rho_m)\cos(-mMt) + i \sum_{m=-\infty}^{\infty} (\sigma_0 {\rho_m}^* - {\sigma_0}^* \rho_m)\sin(-mMt) \\ + \sum_{m=-\infty}^{\infty} (\sigma_1 {\rho_m}^* + {\sigma_1}^* \rho_m)\cos(\Omega - mMt) + i \sum_{m=-\infty}^{\infty} (\sigma_1 {\rho_m}^* - {\sigma_1}^* \rho_m)\sin(\Omega - mMt) \\ + \cdots \\ + \sum_{m=-\infty}^{\infty} (\sigma_n {\rho_m}^* + {\sigma_n}^* \rho_m)\cos(n\Omega - mMt) + i \sum_{m=-\infty}^{\infty} (\sigma_n {\rho_m}^* - {\sigma_n}^* \rho_m)\sin(n\Omega - mMt) \\ + \cdots \end{pmatrix}$$

Demodulating the signal in side-bands $n\Omega - mMt$ but not $n\Omega$, we obtain the demodulated signal:

$$U_{n,m} \propto \sigma_n {\rho_m}^* + {\sigma_n}^* \rho_m$$

$$= 2\mathrm{Re}(\sigma_n {\rho_m}^*)$$

$$= 2\mathrm{Re}\left(s_n e^{i\phi_n} \cdot {s_{ref}}^* J_m(\gamma)^* e^{-i\left(\psi_{ref} + i\frac{m\pi}{2}\right)}\right)$$

$$= 2 s_n s_{ref} J_m(\gamma)\cos\left(\phi_n - \psi_{ref} - i\frac{m\pi}{2}\right)$$

$$\approx 2 s_{nf,n} s_{ref} J_m(\gamma)\cos\left(\phi_{nf,n} - \psi_{ref} - i\frac{m\pi}{2}\right) \text{ for high enough demoduation order}$$

$$\Longrightarrow \begin{matrix} \dfrac{U_{n,m}}{s_{ref} J_m(\gamma)} = s_{nf,n}\sin\left(\phi_{nf,n} - \psi_{ref}\right) = \mathrm{Im}\left(\sigma_{nf,n} e^{-i\psi_{ref}}\right) \text{ for odd m} \\ \dfrac{U_{n,m}}{s_{ref} J_m(\gamma)} = s_{nf,n}\cos\left(\phi_{nf,n} - \psi_{ref}\right) = \mathrm{Re}\left(\sigma_{nf,n} e^{-i\psi_{ref}}\right) \text{ for even m} \end{matrix}$$

Assuming $J_j(\gamma) = J_l(\gamma)$, and introducing a complex constant $\kappa = \dfrac{e^{i\psi_{ref}}}{s_{ref}}$, we can obtain:

$$\sigma_{nf,n} = \frac{\kappa}{J_j(\gamma)}\left(U_{n,j} + iU_{n,l}\right)$$

Appendix C: Demodulated Signal for Nano-FTIR

The backscattered field E_{sca} after modulating the distance between the tip and sample surface with frequency Ω is:

$$E_{\mathrm{sca}} = E_{\mathrm{inc}} \sum_{n=0}^{\infty} \sigma_n e^{in\Omega t}$$

where $\sigma_n = \sigma_{\mathrm{nf},n} + \sigma_{\mathrm{b},n}$.

On the other hand, the reference field is:

$$E_{\mathrm{ref}} = \sigma_{\mathrm{ref}} E_{\mathrm{inc}} = s_{\mathrm{ref}} e^{i\phi_{\mathrm{ref}}} E_{\mathrm{inc}}$$

The detected signal U is proportional to the intensity of the combination of E_{ref} and E_{sca}, therefore,

$$U \propto \left(E_{\mathrm{sca}} + E_{ref}\right)\left({E_{\mathrm{sca}}}^{*} + {E_{ref}}^{*}\right)$$

$$= {E_{inc}}^{2}\left(\sum_{n=0}^{\infty} \sigma_n e^{in\Omega t} + s_{ref} e^{i\phi_{ref}}\right)\left(\sum_{n=0}^{\infty} {\sigma_n}^{*} e^{-in\Omega t} + s_{ref} e^{-i\phi_{ref}}\right)$$

$$\propto \left(\sum_{n=0}^{\infty} \sigma_n e^{in\Omega t}\right)\left(\sum_{n=0}^{\infty} {\sigma_n}^{*} e^{-in\Omega t}\right) + {s_{ref}}^{2} + \sum_{n=0}^{\infty} s_{ref}\sigma_n e^{in\Omega t} e^{-i\phi_{ref}} + i\sum_{n=0}^{\infty} s_{ref}{\sigma_n}^{*} e^{-in\Omega t} e^{i\phi_{ref}}$$

$$= {E_{\mathrm{sca}}}^{2} + {s_{ref}}^{2} + \sum_{n=0}^{\infty} s_{ref}\left(\sigma_n e^{-i\phi_{ref}} + {\sigma_n}^{*} e^{i\phi_{ref}}\right)\cos n\Omega t + i\sum_{n=0}^{\infty} s_{ref}\left(\sigma_n e^{-i\phi_{ref}} - {\sigma_n}^{*} e^{i\phi_{ref}}\right)\sin n\Omega t$$

The first term is the same as Equation (A. 1), thus the contribution for n$^{\mathrm{th}}$ order demodulation follows the Equation (69) and is equal to $s_{\mathrm{nf},n}{s_{\mathrm{bg},0}}^{*}\cos\left(\phi_{\mathrm{nf},n} - \phi_{\mathrm{bg},0}\right)$. The third term shows extra contribution for the demodulated signal in nΩ:

$$s_{ref}\left(\sigma_n e^{-i\phi_{ref}} + {\sigma_n}^{*} e^{i\phi_{ref}}\right) = 2s_{ref}\mathrm{Re}\left[s_n e^{i(\phi_n - \phi_{ref})}\right] = 2s_{ref}s_n\cos\left(\phi_n - \phi_{ref}\right) \approx 2s_{ref}s_{nf,n}\cos\left(\phi_{nf,n} - \phi_{ref}\right) \text{ for high demodulation order } n$$

As a result, the total demodulated signal in nΩ is:

$$U_n \propto s_{\mathrm{nf},n}[s_{\mathrm{b},0}\cos\left(\varphi_{\mathrm{nf},n} - \varphi_{\mathrm{b},0}\right) + s_{\mathrm{ref}}\cos\left(\varphi_{\mathrm{nf},n} - \varphi_{\mathrm{ref}}\right)]$$

Appendix D: Relation between Real and Imaginary Part of $k_{\|}$

According to Equation (36) and assuming medium is uniaxial and is non-magnetic so that $\mu = 1$, one can have the relation for propagation constant of a TE in-plane mode

$$k_{\|}^2 = \varepsilon_{\|} k_0^2 - k_z^2$$

$$\left(k_{\|}' + ik_{\|}''\right)^2 = \left(\varepsilon_{\|}' + i\varepsilon_{\|}''\right)k_0^2 - k_z^2$$

$$k_{\|}'^2 - k_{\|}''^2 + i\left(2k_{\|}'k_{\|}''\right) = \varepsilon_{\|}' k_0^2 - k_z^2 + i\left(\varepsilon_{\|}'' k_0^2\right)$$

Comparing the imaginary part, one can have the relation between $k_{\|}'$ and $k_{\|}''$:

$$k_{\|,\mathrm{TE}}'' = \frac{\varepsilon_{\|}'' k_0^2}{k_{\|}'}. \tag{D.1}$$

For TM modes, the relation for propagation constant should be modified to

$$k_{\|}^2 = \varepsilon_{\perp} k_0^2 - \frac{\varepsilon_{\perp}}{\varepsilon_{\|}} k_z^2$$

$$\frac{\varepsilon_{\|}}{\varepsilon_{\perp}} k_{\|}^2 = \varepsilon_{\|} k_0^2 - k_z^2$$

$$\frac{\varepsilon_{\|}' + i\varepsilon_{\|}''}{\varepsilon_{\perp}' + i\varepsilon_{\perp}''}\left(k_{\|}' + ik_{\|}''\right)^2 = \left(\varepsilon_{\|}' + i\varepsilon_{\|}''\right)k_0^2 - k_z^2$$

$$\frac{\left(\varepsilon_{\|}' + i\varepsilon_{\|}''\right)\left(\varepsilon_{\perp}' - i\varepsilon_{\perp}''\right)}{\varepsilon_{\perp}'^2 + \varepsilon_{\perp}''^2}\left(k_{\|}'^2 - k_{\|}''^2 + i\left(2k_{\|}'k_{\|}''\right)\right) = \varepsilon_{\|}' k_0^2 - k_z^2 + i\left(\varepsilon_{\|}'' k_0^2\right)$$

Expanding the equation and comparing the imaginary parts of both sides, it gives

$$2k_{\|}'k_{\|}''\left(\varepsilon_{\|}'\varepsilon_{\perp}' + \varepsilon_{\|}''\varepsilon_{\perp}''\right) + \left(\varepsilon_{\|}''\varepsilon_{\perp}' - \varepsilon_{\|}'\varepsilon_{\perp}''\right)\left(k_{\|}'^2 - k_{\|}''^2\right) = \left(\varepsilon_{\perp}'^2 + \varepsilon_{\perp}''^2\right)\varepsilon_{\|}'' k_0^2$$

$$\left(\varepsilon_{\|}''\varepsilon_{\perp}' - \varepsilon_{\|}'\varepsilon_{\perp}''\right)k_{\|}''^2 - 2k_{\|}'k_{\|}''\left(\varepsilon_{\|}'\varepsilon_{\perp}' + \varepsilon_{\|}''\varepsilon_{\perp}''\right) = \left(\varepsilon_{\|}''\varepsilon_{\perp}' - \varepsilon_{\|}'\varepsilon_{\perp}''\right)k_{\|}'^2 - \left(\varepsilon_{\perp}'^2 + \varepsilon_{\perp}''^2\right)\varepsilon_{\|}'' k_0^2$$

By completing the square, it gives

$$\left(\varepsilon_{\|}''\varepsilon_{\perp}' - \varepsilon_{\|}'\varepsilon_{\perp}''\right)\left(k_{\|}'' - k_{\|}'\frac{\varepsilon_{\|}'\varepsilon_{\perp}' + \varepsilon_{\|}''\varepsilon_{\perp}''}{\varepsilon_{\|}''\varepsilon_{\perp}' - \varepsilon_{\|}'\varepsilon_{\perp}''}\right)^2 - \left(\varepsilon_{\|}''\varepsilon_{\perp}' - \varepsilon_{\|}'\varepsilon_{\perp}''\right)\left(k_{\|}'\frac{\varepsilon_{\|}'\varepsilon_{\perp}' + \varepsilon_{\|}''\varepsilon_{\perp}''}{\varepsilon_{\|}''\varepsilon_{\perp}' - \varepsilon_{\|}'\varepsilon_{\perp}''}\right)^2$$
$$= \left(\varepsilon_{\|}''\varepsilon_{\perp}' - \varepsilon_{\|}'\varepsilon_{\perp}''\right)k_{\|}'^2 - \left(\varepsilon_{\perp}'^2 + \varepsilon_{\perp}''^2\right)\varepsilon_{\|}'' k_0^2$$

After rearranging the terms, one can obtain the expression of $k_{\|,\mathrm{TM}}''$:

$$k''_{\parallel,\mathrm{TM}} = k'_{\parallel,\mathrm{TM}} \frac{\varepsilon'_{\parallel}\varepsilon'_{\perp} + \varepsilon''_{\parallel}\varepsilon''_{\perp}}{\varepsilon''_{\parallel}\varepsilon'_{\perp} - \varepsilon'_{\parallel}\varepsilon''_{\perp}} \left(1 - \sqrt{1 + \left(\frac{\varepsilon''_{\parallel}\varepsilon'_{\perp} - \varepsilon'_{\parallel}\varepsilon''_{\perp}}{\varepsilon'_{\parallel}\varepsilon'_{\perp} + \varepsilon''_{\parallel}\varepsilon''_{\perp}} \right)^2 \left(1 - \frac{\left({\varepsilon'_{\perp}}^2 + {\varepsilon''_{\perp}}^2 \right)\varepsilon''_{\parallel} k_0^2}{\left(\varepsilon''_{\parallel}\varepsilon'_{\perp} - \varepsilon'_{\parallel}\varepsilon''_{\perp} \right) {k'_{\parallel,\mathrm{TM}}}^2} \right)} \right). \quad (\mathrm{D.2})$$

The equations (D.1) and (D.2) can be used to calculate the propagation length through the equation $L_p = \frac{1}{2k''_{\parallel}}$ (Equation (87)).